International Journal of Acoustics and Vibration

A quarterly publication of the International Institute of Acoustics and Vibration

Volume 20, Number 3, September 2015

EDITORIAL

ARTICLES

Editor's Space

What I Don't Know Part 1 of 2

This editorial is taken from one published in Sound & Vibration, May 2003 but significantly modified.

Unlike most editorials or articles, where the author tells the readership what he/she knows, I thought I'd take this opportunity to write about things in acoustics that I don't know. I'll limit them to the most pressing issues.

Calibration Intervals of Instruments. Why do most people insist on yearly instrument calibrations? Instrument manufacturers have not been able to provide data to justify the 'recommended yearly interval,' a de facto standard. In about 2005 or so, there arose documents (Organization Internationale Metrologie Legal) that at least suggested the one-year interval was meaningless. The document stated that the interval should depend on use (If it sat on a shelf for a year, did it need to be calibrated?); on history of drift; on criticality of measurements (Suppose you only care about approximate sound levels or have a limited frequency range.); and on abuse (Suppose you drop it.). And finally, ISO 17025, a standard for quality control of test and calibration laboratories, has wording that states a lab may not put calibration due dates on instruments. The standard reaffirms that only the user, based on past data and instrument use, can determine intervals. Conclusion: pick up a copy of "OIML 10 ILAC_G24_2007" and develop a justification for your calibration intervals based on experience and past calibrations.

Use of Microphones. Most measuring microphones are characterized as 'free-field' or 'pressure/random incidence.' The former has a well-defined frequency response for an acoustical field without any reflections and measures the pressure as though the microphone was absent. The latter is for a random incidence acoustical field (closely approximated by a pressure response) with the microphone as part of the field. But when we measure almost anything (community noise, HVAC noise, industrial noise), the field is never 'free' or 'random incidence.' This means the well-defined frequency response for ideal fields is not met and the actual response to the measurement field is unknown. Thus, the accuracy of the measurement is a function of the spectrum of the sound, which is not known except by measurement. Conclusion: the uncertainty of measurements is much more than we are led to think.

Windscreens. Just about all acoustical measurements outdoors include the use of a windscreen placed over the microphone grid. Few people give thought or care about the effects of the windscreen on the measurement. Ostensibly, the screen reduces the effects of wind noise at the diaphragm. But, at the same time, the windscreen adds a transfer function—an insertion loss—as a function of frequency that modifies the spectrum measured from that produced. Unless this transfer function is known with some uncertainty, the accuracy of the measurements is in dispute. Now, a few manufacturers provide some insertion loss characteristics of their windscreen but often the test method is not defined and normally the uncertainty of the results are not given. However most windscreens are uncharacterized. Experience shows that a windscreen can easily change a 'Class 1' measurement to a 'Class 2' measurement, and worse, it can effect frequency response by more than 5 dB at higher frequencies. Conclusion: if you want the measurement to be accurate you must know the insertion loss of your windscreen.

Temperature and Wind Gradients. These phenomena occur very often and are temporally and spatially varying. They effect measurements of noise as well as long range propagation. Because these gradients are probably never measured over the propagation distance, we know nothing of the accuracy of the sound measured from the source. The uncertainty of the measurement seems to be inversely proportional to measurement time. Conclusion: long-term averages are the only way to predict, specify and measure outdoor sound pressure level.

Value of Accuracy Measurements in Acoustics. Why do we measure down to tenths of dB? What are we going to do with high accuracy test results? I suggest that the high measurement accuracy is uncalled for in most cases. For example, what do we really know about the randomness of community noise? Clearly short-term measurements vary (vehicle pass-by, etc.), and with changing environments, I suspect yearly descriptors (virtually useless) will never be the same from one year to another (changing demographics, etc.). Does a very accurate measurement instrument give any better information? In industrial noise, except for a few cases, repeatability of a test will never give the same results within 1-2 dB. In architectural acoustics, is there a perceptible difference of a ceiling tile with a sound absorption coefficient of 0.80 or 0.85? I suspect not. The sound power determined from an air-handler in a reverb room can be measured within 0.1 dB (then add the 2-3 dB uncertainty). Since the quantity we really care about is sound pressure, and the air-handler is mounted differently in less-than-ideal-conditions when installed, does that 0.1 dB matter? Conclusion: the science and sophistication of noise measurement far exceed the subjective usefulness of the measurements. Class 2 meters could replace many measurements requiring Class 1 meters with no appreciable difference in real results.

Richard J. Peppin
Director, IIAV

Improved Crack Closure Line Position: An Improved Model for Crack Breathing Phenomenon

R. Ramezanpour, M. Ghayour and S. Ziaei-Rad

Department of Mechanical Engineering, Isfahan University of Technology 84156-83111 Isfahan, Iran

(Received 3 October 2012; accepted 15 November 2013)

The dynamic behaviour of a cracked Jeffcott rotor is investigated in this paper. The crack is located at the midpoint of the rotor. It is known that when the static deflection dominates the vibration of the rotating shaft, the crack opens and closes according to the shaft rotation. This phenomenon is known as crack breathing. There are several models for classifying crack breathing phenomena, such as the switching crack model, harmonic approach model, and response-dependent breathing crack model. In order to model the breathing of the crack in the response-dependent breathing crack model, the concept of a crack closure line position (CCLP) is proposed and used by some researchers. The main scope of this work is to present an improved crack closure line position (ICCLP). By using several contour plots over the crack's surface, it is shown that the imaginary line that separates the open and closed parts of a breathing crack should not be considered perpendicular to the crack tip. It is also shown that the improved model positively agrees with those proposed in the literature. The effects of ICCLP on the coefficients of the local flexibility matrix are investigated.

NOMENCLATURE

Symb.	Unit	Description
I	m^4	area moment of inertia for the cross section
k_{ij}	N/m, N/rad	cross-coupled stiffness
dp	m	disk diameter
e	m	eccentricity
$[k]_g$		global stiffness matrix
φ	rad	initial phase angle
$[c]_l$		local flexibility matrix of the cracked shaft
m	kg	mass of the disk
ν		Poisson ratio
R, d	m	radius and diameter of the shaft, respectively
α	rad	rotor center displacement in rotational direction
l	m	shaft length
k_x	N/m	stiffness in x direction
k_y	N/m	stiffness in y direction
k_u	N/m	stiffness in longitudinal direction
k_T	N/rad	stiffness in torsional direction
W	Nm	strain energy due to crack
U	Nm	strain energy of uncracked shaft
t	s	time in seconds
$[C_s]$		total flexibility matrix of the uncracked shaft
$[K]_l$		local stiffness matrix
η_0	m	location of elemental strip along η' direction
$[H]$		transformation matrix
h	m	height of the element strip
J_p	m^2	polar moment of inertia for the cross section
q_1	N	longitudinal force (internal reaction)
c	Ns/m	transversal damping coefficient
E	N/m^2	modulus of elasticity
q_4, q_5	Nm	bending moments (internal reactions)
c_T	Ns/rad	torsional damping coefficient
γ	m	crack depth
Ω	rpm	revolutionary speed
c_u	Ns/m	longitudinal damping coefficient
$M(t)$	Nm	external torsional excitation
G	N/m^2	modulus of rigidity
ω_T	rpm	torsional excitation frequency
A	m^2	cross sectional area of the crack
x, y	m	transversal displacements of center of disk
u	m	longitudinal displacement of center of disk
α	rad	torsional displacement of center of disk
F_z	N	longitudinal force (external load)
T	Nm	torsional moment
J	kgm^2	mass moment of inertia of the disk
K_{I}^i	$N/m\sqrt{m}$	opening mode of the crack due to internal load "i"
K_{III}^j	$N/m\sqrt{m}$	tearing mode of the crack due to internal load "j"
K_{I}	$N/m\sqrt{m}$	total opening mode of the crack
K_{III}	$N/m\sqrt{m}$	total tearing mode of the crack
F_1, F_2, F_{III}		influential functions

1. INTRODUCTION

Many investigations have been conducted concerning the overall behaviour of cracked shafts in past decades. In general, a crack in rotating shafts may be classified in three different ways: opened crack, closed crack, and breathing crack. In other words, if a cracked shaft rotates under external loading, then the crack opens and closes regularly per revolution, which could be said to breathe. This phenomenon is produced

by the stress distribution around the crack.[1] This is a very common situation in large turbine-generator rotors.[2] Throughout the two past decades, the main focus of some studies was the modelling and explanation of the breathing mechanism in cracked shafts.[3–14] Georgantzinos et al. investigated the time history of local flexibilities associated with a breathing crack in a rotating shaft.[1] The deflections of a beam with a circular cross-section presenting a crack of different depths was analysed using quasi-static approximation with the aid of a refined nonlinear contact-finite element. The partial contact of crack surfaces was predicted by using this method. In his excellent review paper, Papadopoulos explained many crack models, such as the open crack model, switching crack model, second moment inertia model, breathing models, and harmonic model approaches.[2] The use of strain energy release rate theory (SERR) and its combination with linear fracture mechanics and rotor dynamics for calculating the compliance matrix have been considered in detail.

Dimarogonas and Papadopoulos conducted an analysis of a cracked rotor neglecting the non-linear behaviour of the crack by assuming a constant stiffness asymmetry and using the theory of shafts with dissimilar moments of inertia.[6] Later, they derived a complete flexibility matrix of the cross-section containing the crack.[7] Grabowski suggested switching the stiffness values, from those of an uncracked rotor (closed crack state) with those of a cracked rotor (fully open state) at a particular angular position of the rotor (when the crack edge becomes vertical).[8] Mayes and Davies suggested sinusoidal stiffness variations to model the breathing in a more sensible way, as a rotor crack is expected to open and close gradually due to gravity.[9] Papadopoulos and Dimarogonas represented stiffness variation by means of a truncated, four term series using known stiffness matrices corresponding to half-open, half-closed, fully open, and fully closed cracks.[10] Changhe et al. represented the crack as a hinge with variable stiffness in two rotor-fixed lateral directions.[11] The crack is introduced at the node of a finite element model. Ballo investigated the flexural vibrations of a continuous slender shaft with a crack.[12] The mathematical model of the problem has been formulated by means of the finite element method. However, the crack was modelled by a switching crack. It has been shown that the increase in crack depth causes a decrease in the bending stiffness, whereas the nonlinearity is related to the opening and closing of the crack faces in the process of flexural vibrations. Subsequently, the theoretical results have been illustrated by the calculation of the amplitudes and phases of the second and third harmonics of the forced shaft flexural vibrations. Darpe et al. proposed a response-dependent non-linear breathing crack model, which is called crack closure line position (CCLP).[13] Considering all six degrees of freedom per node, the stiffness matrix in a Timoshenko beam element is modified to account for the effect of the crack. Using this model, they were able to study the coupling between longitudinal, lateral, and torsional vibrations. They observed that motion coupling, together with the rotational effect of the rotor and non-linearities due to their proposed breathing model, introduced sum and difference frequency in the response of the cracked rotor. Bachschmid et al. used a 3D FE model to investigate the breathing mechanism in a rotating shaft.[14] Slant and helicoidally cracks are the two types of crack shape models that they considered. A simplified model to determine the open area of a crack is also presented in their work. This simple model has been used for analysing the non-linear dynamic behaviour of cracked rotating shafts, which occurs when breathing is governed by the vibration itself. It has been concluded that torsional deflections could be generated by bending moments due to the coupling effects.

Additionally, the response of a cracked rotor is investigated in some of the literature. Sekhar investigated the dynamic behaviour of a cracked rotor—in particular, that of a rotor with two open transverse cracks.[15] The influence of one crack over the other was studied using finite element analysis while considering flexural vibrations. Darpe et al. investigated a simple Jeffcott rotor with two transverse surface cracks.[16] However, they assumed that one crack remains open while the other is breathing. Also, the effect of the interaction of two cracks on the breathing behaviour and on the unbalanced response of the rotor was studied. They observed significant changes in the dynamic response of the rotor when the angular orientation of one crack relative to the other is varied. Darpe et al. presented a novel way to detect fatigue transverse cracks in rotating shafts.[17] In this technique, a transient torsional excitation was applied for a very short duration at a specific angular orientation of the rotor, and then the transient features of the resonant bending vibration were revealed using wavelet transform. Subsequently the sensitivity of the proposed methodology to the depth of crack is investigated. It is mentioned that this detection method is very specific to the behaviour of the transverse surface crack in a horizontal rotor. Fortunately, a positive feature of their proposed method was that the response features were different from the responses of other common rotor faults under similar excitation. Lin and Chu investigated the dynamic behaviour of a slant (45^o crack angle) cracked rotor.[18] Using the Jeffcott rotor model, the equation of motion was extracted in four directions. The global stiffness of the system was obtained from concepts of fracture mechanics and strain energy release rate. They mentioned that a much longer time is required to compute the steady responses of a breathing cracked shaft than that of an open cracked shaft and that this is why almost all investigators have adopted the open crack model. The existence of the frequency of torsional excitation is included in the longitudinal response, and the combined frequencies of the rotating frequency and the frequency of torsional excitation in the transverse response are good indicators for slant crack detection.

By using several contour plots over the crack surface, it is shown in this paper that the imaginary line (crack closure line) that separates the open and closed parts of a breathing crack should not be considered perpendicular to the crack tip. According to these plots, a new breathing model called the improved crack closure line position (ICCLP) is introduced. Using the proposed model, the dynamic behaviour of a cracked Jeffcott rotor is considered. The effect of this model on the flexibility of the cracked shaft is investigated in detail. Subsequently, steady state responses and their spectrums are investigated.

2. EQUATIONS OF MOTION

Consider a Jeffcott rotor rotating at speed Ω (Fig. 1). It has a massless shaft and a disk with mass m. A view of the cross-section of the disk is shown in Fig. 2. In this figure, XOY is the stationary coordinate, $\xi o\eta$ is the rotational coordinate with

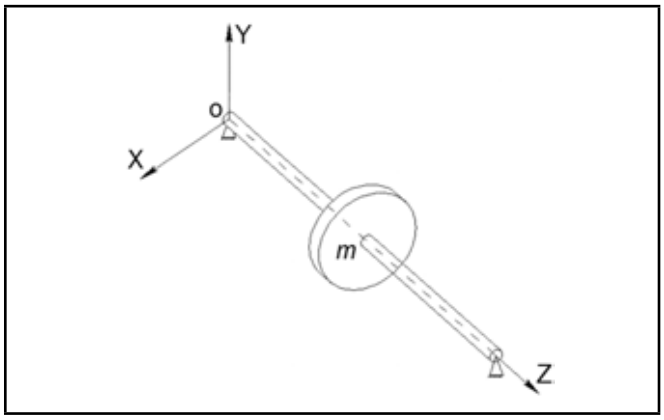

Figure 1. Jeffcott rotor model.

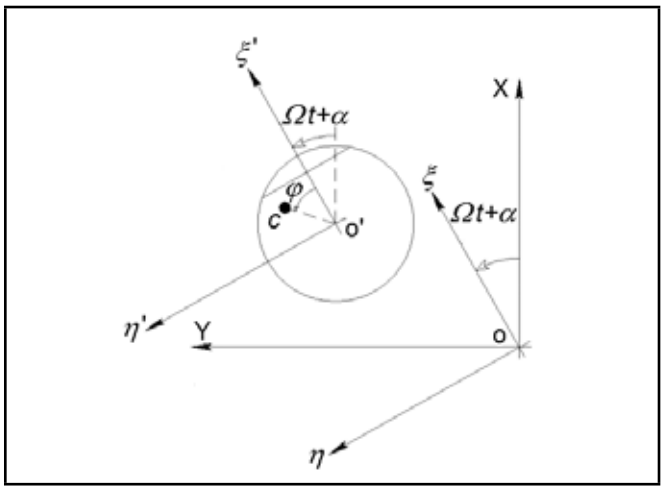

Figure 2. Cross-sectional view of crack at midpoint of the shaft.

centre o, and $\xi' o' \eta'$ is the rotational coordinate that is attached at the centre of the disk. Coordinate o' is the centre of the disk, c is the centre of mass of the disk, α is the angle that is caused by torsional vibration, and φ is the phase angle of the centre of mass.

The angle position of the centre of mass is

$$\Theta = \Omega t + \alpha + \varphi; \tag{1}$$

then

$$\dot{\Theta} = \Omega + \dot{\alpha}, \qquad \ddot{\Theta} = \ddot{\alpha}. \tag{2}$$

Using the d'Alambert principle (Fig. 3), the equation of motion in four directions (two transverse, one torsional, and one longitudinal) can be established as

$$m\ddot{x} + c\dot{x} + k_x x + k_{xy} y + k_{xT}\alpha + k_{xu} u = -mg + me\,(\Omega+\dot{\alpha})^2 \cos(\Omega t+\alpha+\varphi) + me\ddot{\alpha}\sin(\Omega t+\alpha+\varphi); \tag{3}$$

$$m\ddot{y} + c\dot{y} + k_{xy} x + k_y y + k_{yT}\alpha + k_{yu} u = me\,(\Omega+\dot{\alpha})^2 \sin(\Omega t+\alpha+\varphi) - me\ddot{\alpha}\cos(\Omega t+\alpha+\varphi); \tag{4}$$

$$J\ddot{\alpha} + c_T(\Omega+\dot{\alpha}) + k_{xT} x + k_{yT} y + k_T\alpha + k_{Tu} u = M(t) + mge\sin(\Omega t+\alpha+\varphi) + me\ddot{x}\sin(\Omega t+\alpha+\varphi) - me\ddot{y}\cos(\Omega t+\alpha+\varphi); \tag{5}$$

$$m\ddot{u} + c_u\dot{u} + k_{xu} x + k_{yu} y + k_{Tu}\alpha + k_u u = 0; \tag{6}$$

where J is the mass moment of inertia of the disk, about o'. The damping coefficients in the transverse, torsional, and longitudinal directions are shown by c, c_T, and c_u, respectively. It should be mentioned that these equations are the same as those presented in the work of Lin and Chu.[18] $M(t)$ and e denote the torsional excitation and eccentricity of the disk, respectively. Using Eqs. (3)–(6), the stiffness matrix of the system can be determined as

$$[k]_g = \begin{bmatrix} k_x & k_{xy} & k_{xT} & k_{xu} \\ k_{xy} & k_y & k_{yT} & k_{yu} \\ k_{xT} & k_{yT} & k_T & k_{Tu} \\ k_{xu} & k_{yu} & k_{Tu} & k_u \end{bmatrix}. \tag{7}$$

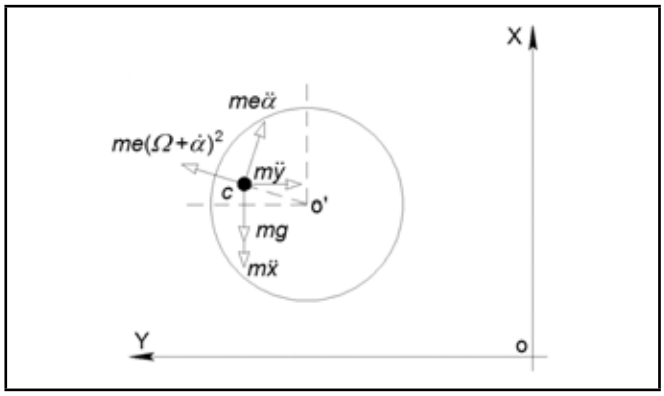

Figure 3. Forces on the centre of mass of the disk.

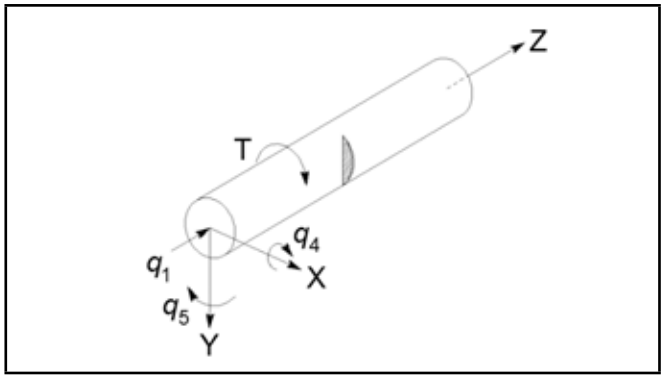

Figure 4. Internal reactions on the crack.

3. FLEXIBILITY OF A CRACKED ROTOR

Suppose that the internal reactions on the crack are two bending moments q_4 and q_5, one torsional moment T, and one longitudinal force q_1 (Fig. 4). Using Castiglione's theorem, the local flexibility of the crack can be written as

$$[c]_l = [G_1][\Delta c_{ij}][G_2] + [C_s]; \tag{8}$$

where

$$\Delta c_{ij} = \frac{\partial^2 W}{\partial q_i \partial q_j}, \quad [G_1] = \left[\frac{l}{4}, \frac{l}{4}, 1, 1\right], \quad [G_2] = \left[\frac{l}{4}, \frac{l}{4}, 1, 1\right], \quad [C_s] = \mathrm{diag}\left(\frac{l^3}{48EI}, \frac{l^3}{48EI}, \frac{l}{2GJ_p}, \frac{l}{2AE}\right). \tag{9}$$

In Eq. (9), W is the additional strain energy due to the crack. It is obvious that local flexibility of the crack is determined if additional stain energy due to the crack is known, and it can be expressed as

$$W = \int_A J(A)\, dA; \tag{10}$$

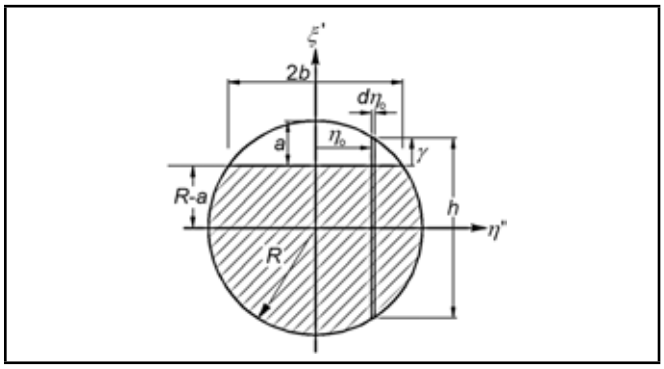

Figure 5. Crack surface.

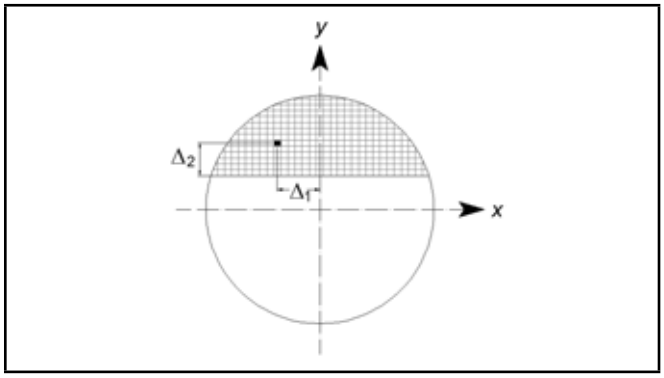

Figure 6. Mesh over the crack surface for evaluation of first mode over the cracked surface.

where $J(A)$ is the strain energy density function. In general, $J(A)$ is a function of K_{I}, K_{II}, and K_{III}, which are the stress intensity factors for the opening mode, sliding mode, and tearing mode, respectively. But here, K_{II} (sliding mode) is neglected. Thus,

$$J = \frac{1}{E'}\left[K_{\mathrm{I}}^2 + (1+\nu)K_{\mathrm{III}}^2\right]; \tag{11}$$

where $E' = \frac{E}{1-\nu^2}$ and ν is the Poisson's ratio. Therefore, according to Eqs. (10) and (11), the additional strain energy due to the crack can be written as

$$W = \int_A \frac{1}{E'}\left[K_{\mathrm{I}}^2 + (1+\nu)K_{\mathrm{III}}^2\right] dA; \tag{12}$$

where A is total surface of the crack for the third crack mode (K_{III}), and the opening part of the surface of crack for the first crack mode (K_{I}).[18]

The crack surface is shown in Fig. 5. Therefore, the stress intensity factors (SIF) for a transverse crack are
for q_1,

$$K_{\mathrm{I}}^1 = \frac{q_1}{\pi R^2}\sqrt{\pi\gamma}F_1; \tag{13}$$

$$K_{\mathrm{III}}^1 = 0; \tag{14}$$

for q_4,

$$K_{\mathrm{I}}^4 = \frac{4q_4\eta_0}{\pi R^4}\sqrt{\pi\gamma}F_1; \tag{15}$$

$$K_{\mathrm{III}}^4 = 0; \tag{16}$$

for q_5,

$$K_{\mathrm{I}}^5 = \frac{4q_5\sqrt{R^2-\eta_0^2}}{\pi R^4}\sqrt{\pi\gamma}F_2; \tag{17}$$

$$K_{\mathrm{III}}^4 = 0; \tag{18}$$

and for T,

$$K_{\mathrm{I}}^T = 0; \tag{19}$$

$$K_{\mathrm{III}}^T = \frac{2T\sqrt{R^2-\eta_0^2}}{\pi R^4}\sqrt{\pi\gamma}F_{\mathrm{III}}. \tag{20}$$

It should be noted that the total effect of q_4 is zero.[18] According to Tada et al.,[19]

$$F_1 = \sqrt{\frac{\tan(\lambda)}{\lambda}}\left[0.752 + 1.01\frac{\gamma}{\sqrt{R^2-\eta_0^2}} + 0.37\left(1-\sin(\lambda)\right)^3\right]\frac{1}{\cos(\lambda)}; \tag{21a}$$

$$F_2 = \sqrt{\frac{\tan(\lambda)}{\lambda}}\left[0.923 + 0.199\left(1-\sin(\lambda)\right)^4\right]\frac{1}{\cos(\lambda)}; \tag{21b}$$

$$F_{\mathrm{III}} = \sqrt{\frac{\tan(\lambda)}{\lambda}}; \tag{21c}$$

where

$$\lambda = \frac{\pi\gamma}{4\sqrt{R^2-\eta_0^2}}. \tag{21d}$$

Therefore, the total strain density functions are

$$K_{\mathrm{I}} = \left(\frac{q_1}{\pi R^2}F_1 + \frac{4q_4\eta_0}{\pi R^4}F_1 + \frac{4q_5\sqrt{R^2-\eta_0^2}}{\pi R^4}F_2\right)\sqrt{\pi\gamma}; \tag{22}$$

$$K_{\mathrm{III}} = \left(\frac{2T\sqrt{R^2-x_0^2}}{\pi R^4}\right)\sqrt{\pi\gamma}F_{\mathrm{III}}. \tag{23}$$

After calculating the local flexibility of the cracked rotor, the local stiffness of the system can easily be calculated as

$$[K]_l = [c]_l^{-1}; \tag{24}$$

and the global stiffness matrix in the inertia coordinate system is

$$[K]_g = [H]^{-1}[K]_l[H]; \tag{25}$$

where

$$[H] = \begin{bmatrix} \cos(\Phi) & \sin(\Phi) & 0 & 0 \\ -\sin(\Phi) & \cos(\Phi) & 0 & 0 \\ 0 & 0 & 1 & 0 \\ 0 & 0 & 0 & 1 \end{bmatrix}, \quad \Phi = \Omega t + \alpha. \tag{26}$$

4. CONSTANT K_{I} CONTOURS OVER THE CRACK SURFACE

In order to use the CCLP model, the value of stress intensity factor in the first mode (K_{I}) is evaluated over the crack tip.[13] The change in the sign of K_{I} shows the position of CCLP, which is assumed to be perpendicular to the crack tip. Therefore, CCLP separates the crack area into two parts: open and closed. In this paper, it is shown that the line that separates the crack surfaces is not perpendicular to the crack tip. A meshed example that has been used here for drawing constant K_{I} contours is shown in Fig. 6. According to Eq. (22), it is obvious that the value of K_{I} is dependent on the values of q_1, q_4, and q_5. Therefore, in order to draw the contours, one is required

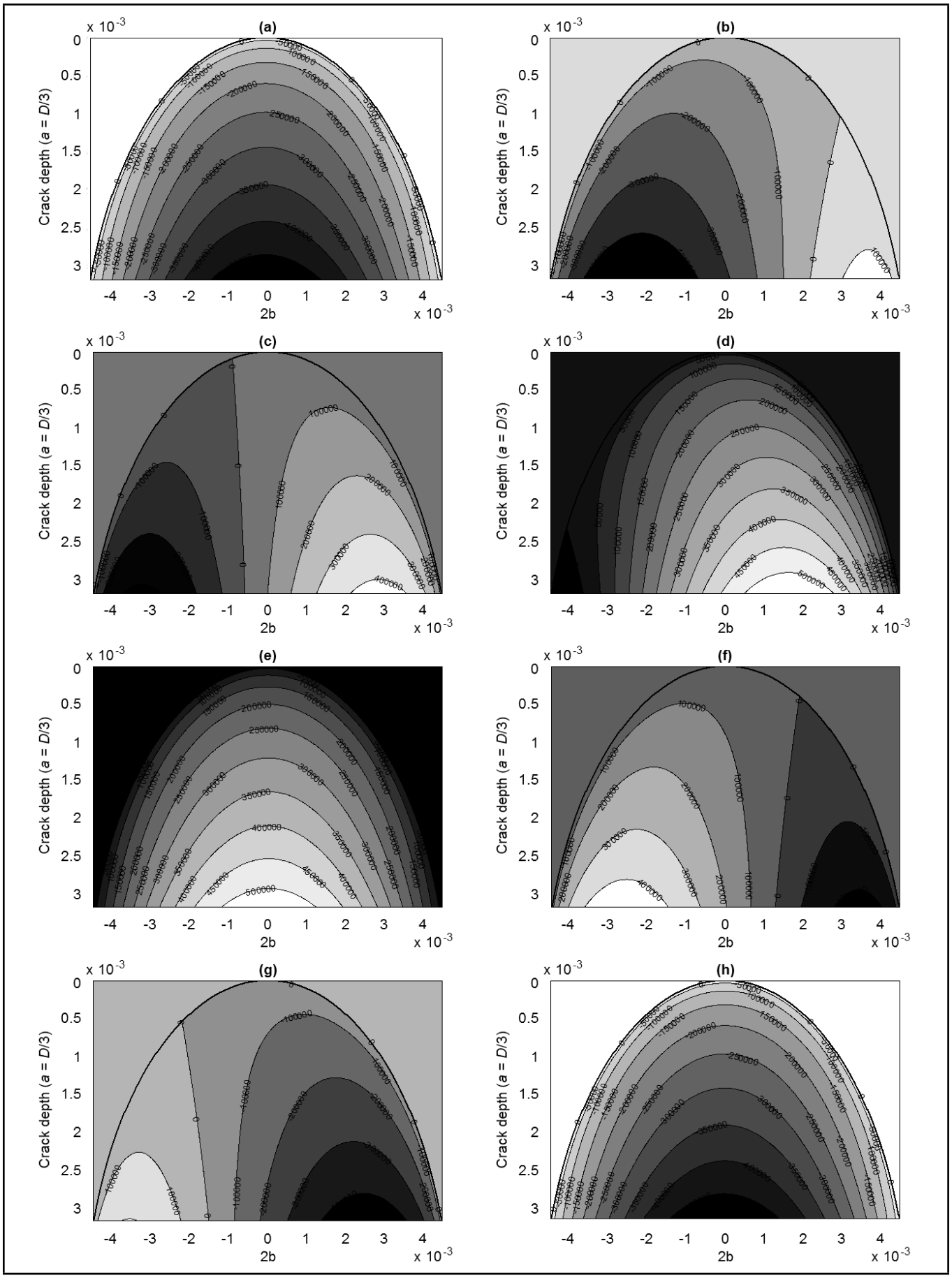

Figure 7. Contours over the crack surface for (a) 0º, (b) 50º, (c) 100º, (d) 150º, (e) 180º, (f) 250º, (g) 300º, and (h) 360º.

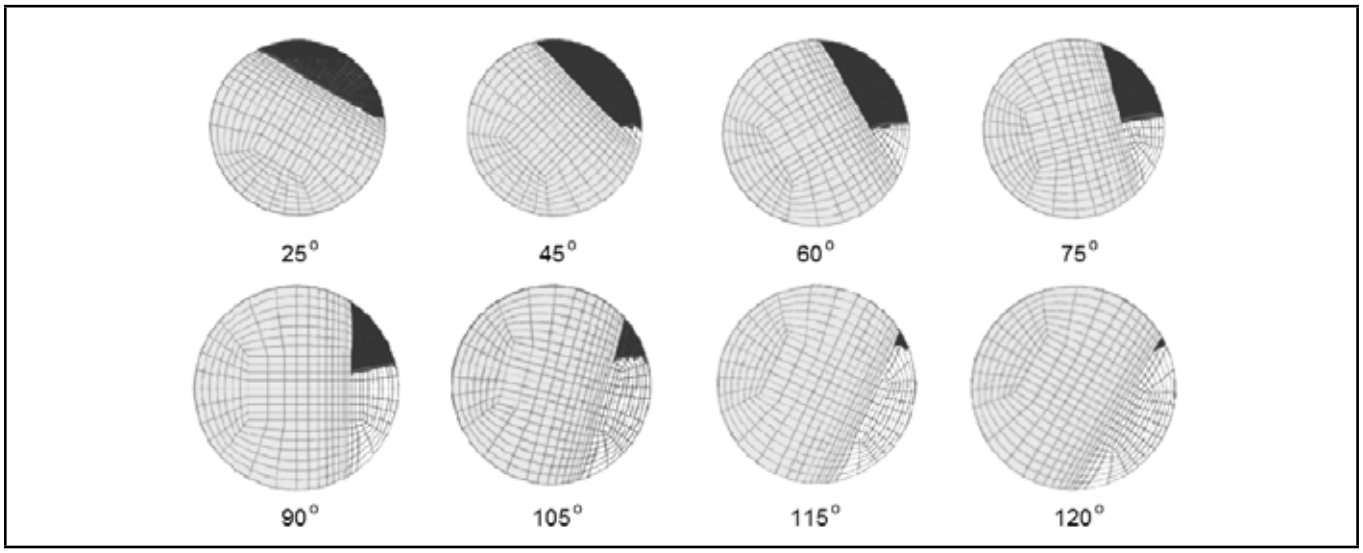

Figure 8. Open and closed areas in different angular positions.[14]

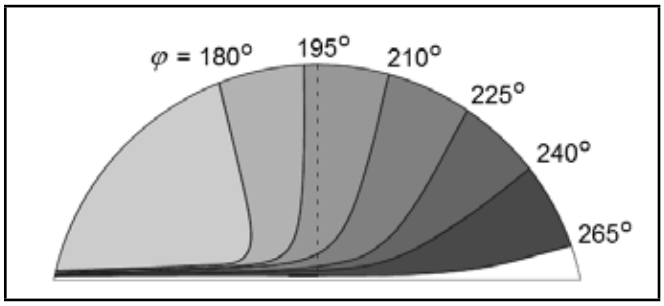

Figure 9. Evolution of contact area between the crack surfaces for a transverse crack under bending.[1]

to solve the equation of motion. On the other hand, the determination of the solution needs the computation of q_1, q_4, and q_5. In fact, drawing the constant K_{I} is an interdependent procedure. This procedure is explained here. Using the Runge-Kutta numerical method, the equations of motion are solved for Δt time intervals, which is related to the time that is needed for one degree rotation of the rotor. Therefore, the values of forces on the crack surface are known. So K_{I} is a function of η and γ which are the distances from the vertical axis (Δ_1) and crack depth line (Δ_2), respectively (see Fig. 6).

Suppose that in the initial situation the crack is closed due to the weight of the rotor; so in $t = 0$, the stiffness of the system is known, and thus the solving of the equations of motion is possible. It should be noted that, in general, the stiffness of a cracked rotor system with a closed crack is not equal to the stiffness of an uncracked rotor. Figure 7 shows the constant K_{I} contours over the crack surface for 0°, 50°, 100°, 150°, 180°, 250°, 300°, and 360°. Figure 2(b) shows the length of the crack depth line. According to this figure, two crack surfaces coincide with each other at the zero rotation angle. In other words, the crack is closed, and therefore all contours have negative values, which show that the two crack surfaces are in compression. Due to an increase in the value of the rotation angle, the crack opens gradually. Therefore, the values on some contours are positive while the others are negative. As one can see, the contour with zero value separates the open and closed parts on the crack surface. At the 90° rotation angle (which is not presented here in Fig. 7), the open and closed parts of the crack separate from each other with a straight line that is perpendicular to the crack tip. In a similar way, due to the increase in the value of the rotation angle, the contour with zero value travels to the left side of the crack surface. So at the 180° rotation angle, all the contours have positive values (which means that the crack is fully open). By increasing the value of the rotation angle further than 180°, contours with zero value travel from the right side to the left side of the crack surface. Here, the contours that are situated on the right side of the zero contour have a negative sign, and the contours that are situated in the left side of the zero contour have a positive sign. This means that the right side of the crack is closing while the left side of it is opening. At the 360° rotation angle, the whole crack surface is closed, similar to the zero angle. Figure 7 shows that the separation boundary is not always a straight line, while this boundary in the CCLP model has been considered as a straight line.[13] Also, it is obvious that this boundary is not perpendicular to the crack tip as has been assumed for the CCLP model. Bachschmid et al. investigated the breathing phenomenon in detail using 3D nonlinear FEM.[14] The open and closed parts of the crack surface during the rotation of the rotor are presented in their work (Fig. 8). According to this figure, the boundary between the open and closed parts of the crack surface is not a straight line. Furthermore, this boundary is not perpendicular to the crack tip. One can therefore claim that these two results are in good agreement to those presented in this section. Figure 9 shows the results that are presented by Georgantzinos and Anifantis, which is evaluated due to bending moments only.[1]

It is obvious that the results presented in Fig. 9 are not the same as those are obtained in this paper. However, the overall schematic of the results are in good agreement with each other.

5. ICCLP MODEL

As mentioned in the previous section, the contour with zero value is the separation curve that separates the open and closed surfaces of the breathing crack from each other. Therefore, the introduced model can be called crack closure curve position (CCCP) (Fig. 10).

According to Fig. 10, the integration in Eq. (12) should be calculated over the ACBD area. Since the determination of the ACBD curve—from every degree of rotation—is almost im-

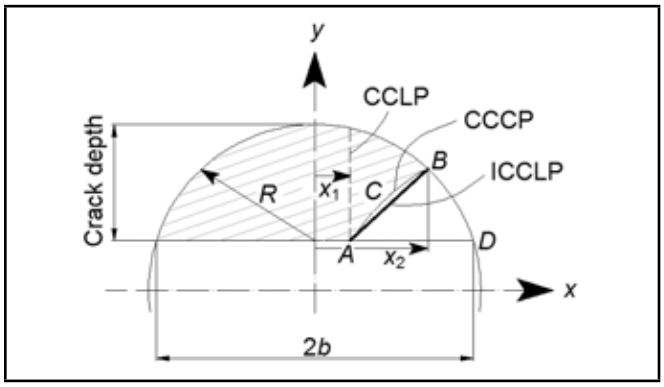

Figure 10. Difference in the location of CCCP, CCLP, and ICCLP.

possible, the curve ACB is approximated by the AB line. This means that the integration in Eq. (12) should be calculated over the ABD area. Due to this approximation, a new breathing model is introduced and is called the ICCLP. Figure 10 shows the position of CCCP and ICCLP. Figure 11 shows the variations of the elements of the $[\Delta c_{ij}]$ matrix for a crack depth $a = D/3$ and $D = 9.5$ mm.

In Fig. 11, the dashed lines express the ICCLP model, and the continuous lines express the CCLP model. It should be noted that the horizontal axis shows the variations of the position of point A, or the CCLP (Fig. 10). According to Fig. 11, the values of compliance, which are calculated with the ICCLP model, are different from those calculated with the CCLP model.

As it is shown in Fig. 12, for CCLPs less than 90°, the amount of the open area of the crack that is bounded by the ICCLP model is less than that bound by the CCLP model. Therefore, compliances that are calculated with the CCLP model are greater than those calculated with the ICCLP model. Also, according to Fig. 12, it is obvious that for CCLPs between 90° and 180°, the values of compliance for the ICCLP model are greater than the values of compliance calculated with the CCLP model. For CCLPs between 180° and 270°, the values of compliance that are calculated with the ICCLP model are greater than those calculated with the CCLP model. However, for CCLPs between 270° and 360°, it is the reverse. It should be noted that Fig. 11 shows that the use of the ICCLP or CCLP models does not change the value of some of the compliance elements, such as $c(1,3)$, $c(2,3)$, and $c(3,4)$. According to Eq. (22), it is obvious that T does not contribute in K_{I}, so the value of $c(3,3)$ is not sensitive to the position of point A; therefore, the value of $c(3,3)$ for CCLP and ICCLP models is the same. Similarly, the values of $c(1,3)$, $c(2,3)$, and $c(3,4)$ are equal to zero for both CCLP and ICCLP models. However, it should be mentioned that K_{III} is not zero for $c(3,3)$, while for $c(1,3)$, $c(2,3)$, and $c(3,4)$ it is zero.

6. NUMERICAL SIMULATION

The parameters that are needed for solving the equations of motion are summarised in Table 1.

A program has been written in the MATLAB® environment to estimate the response of a transverse cracked rotor using the ICCLP model for crack breathing. The solution process for using the model mentioned is presented in Fig. 13. According to this flowchart, the initial displacement is assumed to be equal to the static deflection of the uncracked rotor and the initial

Table 1. Characteristics of the studied rotor system.

Speed of revolution	$\Omega = 500$ rpm
Torsional excitation freq.	$\omega_T = 0.6\Omega = 300$ rpm
External torsional excitation	$M_T = \sin(\omega_T t)$
Transverse damp coefficient	$c = 41.65$ kg/s
Torsional damp coefficient	$c_T = 0.0091$ kgm^2/s
Longitudinal damp coefficient	$c_u = 146.2034$ kg/s
Modulus of elasticity	$E = 210$ GPa
Disk mass	$m = 0.595$ kg
Shaft length	$l = 0.26$ m
Shaft diameter	$d = 9.5$ mm
Disk diameter	$dp = 76$ mm
Initial phase angle	$\varphi = \pi/6$ rad
Poisson's ratio	$\nu = 0.3$
Eccentricity	$e = 0.1643$ mm

stiffness values correspond to that of the cracked rotor. Rotational speed (Ω) and $t_{\max}$, corresponding to total time of solution, are known. Knowing the shaft rotational speed, the time for one degree rotation can be calculated. Using the procedure mentioned (Fig. 13), the program evaluates the forces that act on the crack surfaces. Thus, by using these forces, stress intensity factors (SIFs) are evaluated at points along the crack. Changes in the sign of the SIF over the crack tip determines the position of point A.

Elements of the stiffness matrix for the CCLP model can be evaluated using this point. Also, the position of point B is identified using the zero contour of K_{I} over the crack surface, and therefore, the stiffness of the system that is calculated for the CCLP model is corrected for the ICCLP model. The equation of motion is solved for the Δt time interval by using this stiffness matrix, which is assumed to be constant for one degree of rotation. For the next step, this time increment will increase by Δt, and then the forces that act on the crack will be evaluated. The equations of motion will be calculated for the present step using these forces. This iterative procedure will be repeated until the total time ("t") is greater than or equal to $t_{\max}$. There are two points that should be mentioned about the proposed algorithm: the $t_{\max}$ parameter should be adopted in such a way that guarantees the steady state response of the system; the second point concerns the selection of the time step in the Runge-Kutta numerical method, which should be set in small increments. The small time steps guarantee insignificant changes in the response of the system. In Fig. 13, the steps that are embedded in the program for the ICCLP method are determined by dashed lines. In fact, if this part is removed from the flowchart, the remaining algorithm can be used for the CCLP method. As previously mentioned, in order to determine the position of point B, the contours of K_{I} should be calculated for the crack surface. It is obvious that the calculation of these contours is a time consuming procedure, particularly due to the fact that it should be carried out for every rotation angle. This is why the time required for the ICCLP model is greater than that is for the CCLP model.

Figure 14 shows the non-dimensional position of points A and B (Fig. 10) versus the rotor rotation angle under steady state conditions. According to Fig. 14, for rotation angles of less than 90° (and also between 180° and 270°), the position of point B is always on the right side of point A, which indicates that the separation line is not perpendicular to the crack tip. However, for rotation angles between 90° and 180° (and between 270° and 360°), the position of point B is always on the left side of the position of point A. For angles equal to 0°,

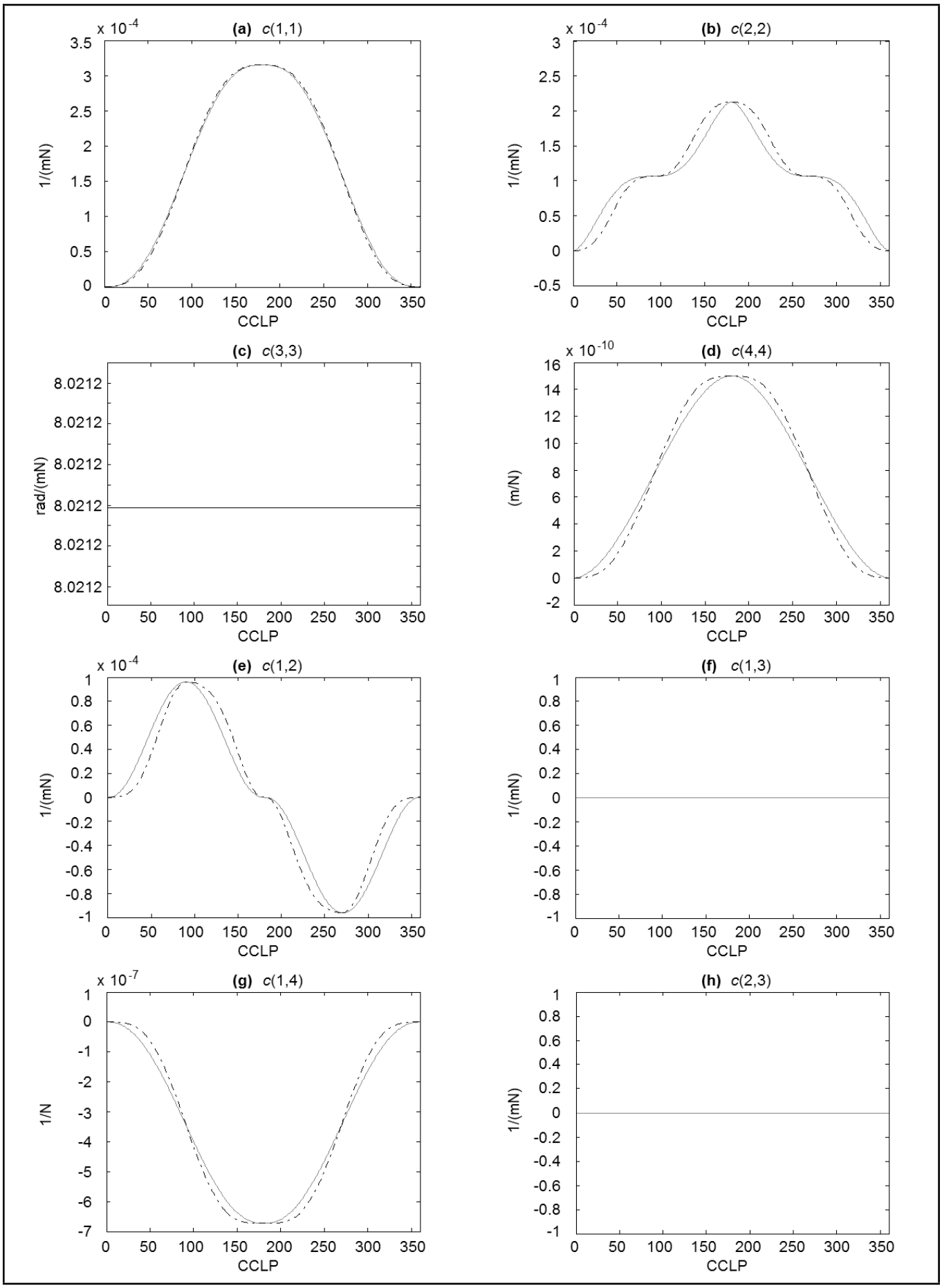

Figure 11. Variations of the elements of the $[\Delta c_{ij}]$ matrix for a crack depth $a = D/3$ and $D = 9.5$ mm; continuous line: CCLP model; dashed line: ICCLP. (a) $c(1,1)$, (b) $c(2,2)$, (c) $c(3,3)$, (d) $c(4,4)$, (e) $c(1,2)$, (f) $c(1,3)$, (g) $c(1,4)$, (h) $c(2,3)$, (i) $c(2,4)$, and (j) $c(3,4)$.

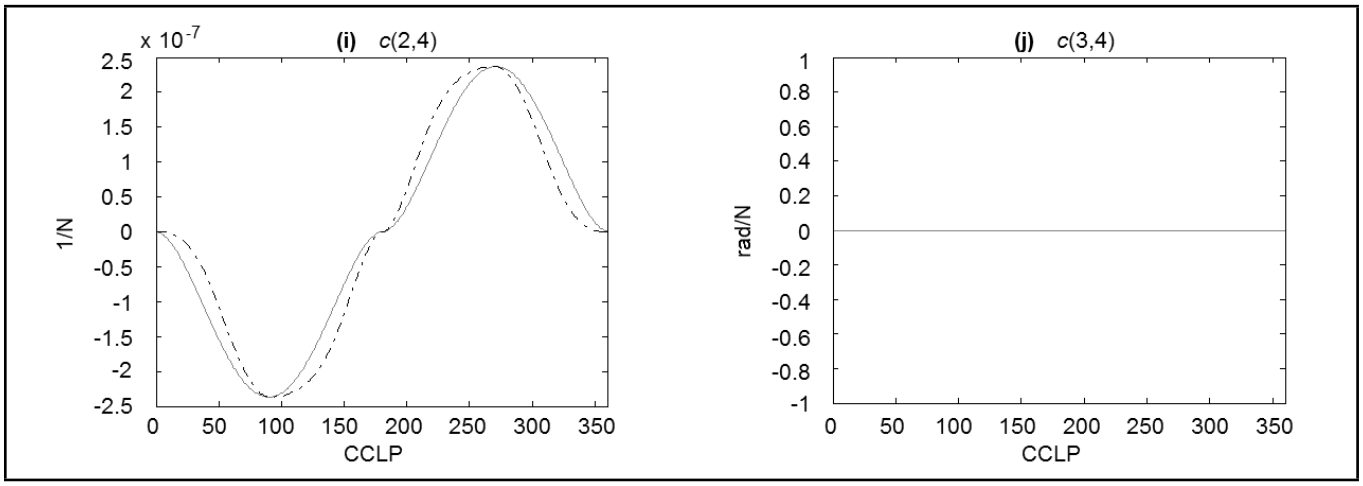

Figure 11. (cont.) Variations of the elements of the $[\Delta c_{ij}]$ matrix for a crack depth $a = D/3$ and $D = 9.5$ mm; continuous line: CCLP model; dashed line: ICCLP. (a) $c(1,1)$, (b) $c(2,2)$, (c) $c(3,3)$, (d) $c(4,4)$, (e) $c(1,2)$, (f) $c(1,3)$, (g) $c(1,4)$, (h) $c(2,3)$, (i) $c(2,4)$, and (j) $c(3,4)$.

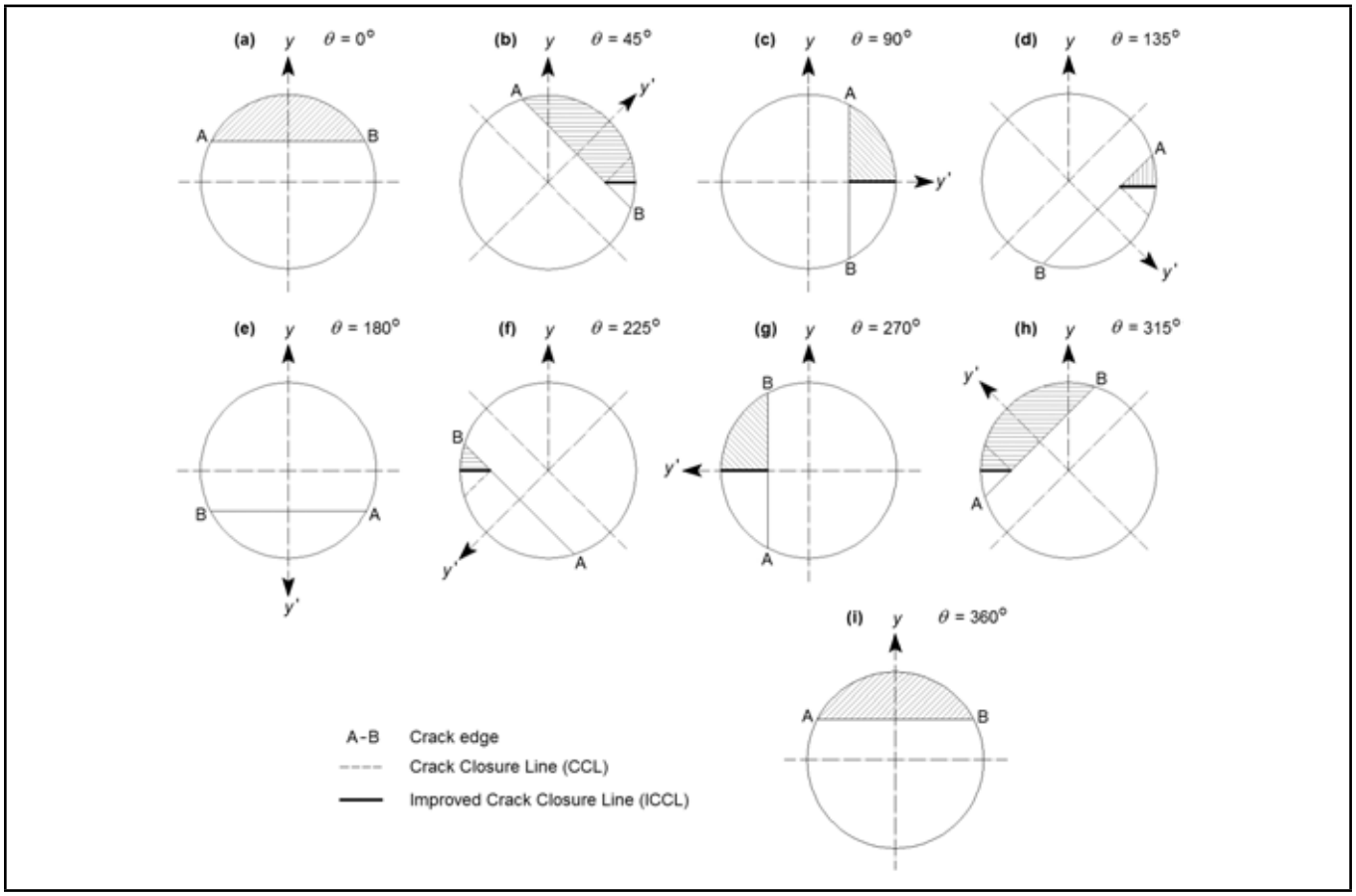

Figure 12. Comparison between ICCLP and CCLP from Darpe et al.[13]

90°, 180°, 270°, and 360°, points A and B coincide with each other. This is why the values of the crack compliance matrix for these angles are the same for the models of CCLP and ICCLP. However, for angles of 90° and 180°, the open and closed parts of the crack area are equal to each other.

Figure 15 shows the time domain steady state responses for the cracked shaft with a transverse crack for four directions (i.e. two transverse, one torsional, and one longitudinal). In Fig. 15, the horizontal axis is the time (in seconds) and the vertical axis is the magnitude of the responses (in metres for transverse and longitudinal responses and in radians for the torsional response). These responses are evaluated for a cracked Jeffcott rotor ($\alpha = a/D$). Furthermore, a continuous line identifies the CCLP model and a dashed line identifies the ICCLP model.

According to Fig. 15, in general, the time responses for the two models are not the same. In other words, except for the torsional response, the other responses in transverse and longitudinal directions are different. The response in the torsional direction is the same for two models, and this can be explained

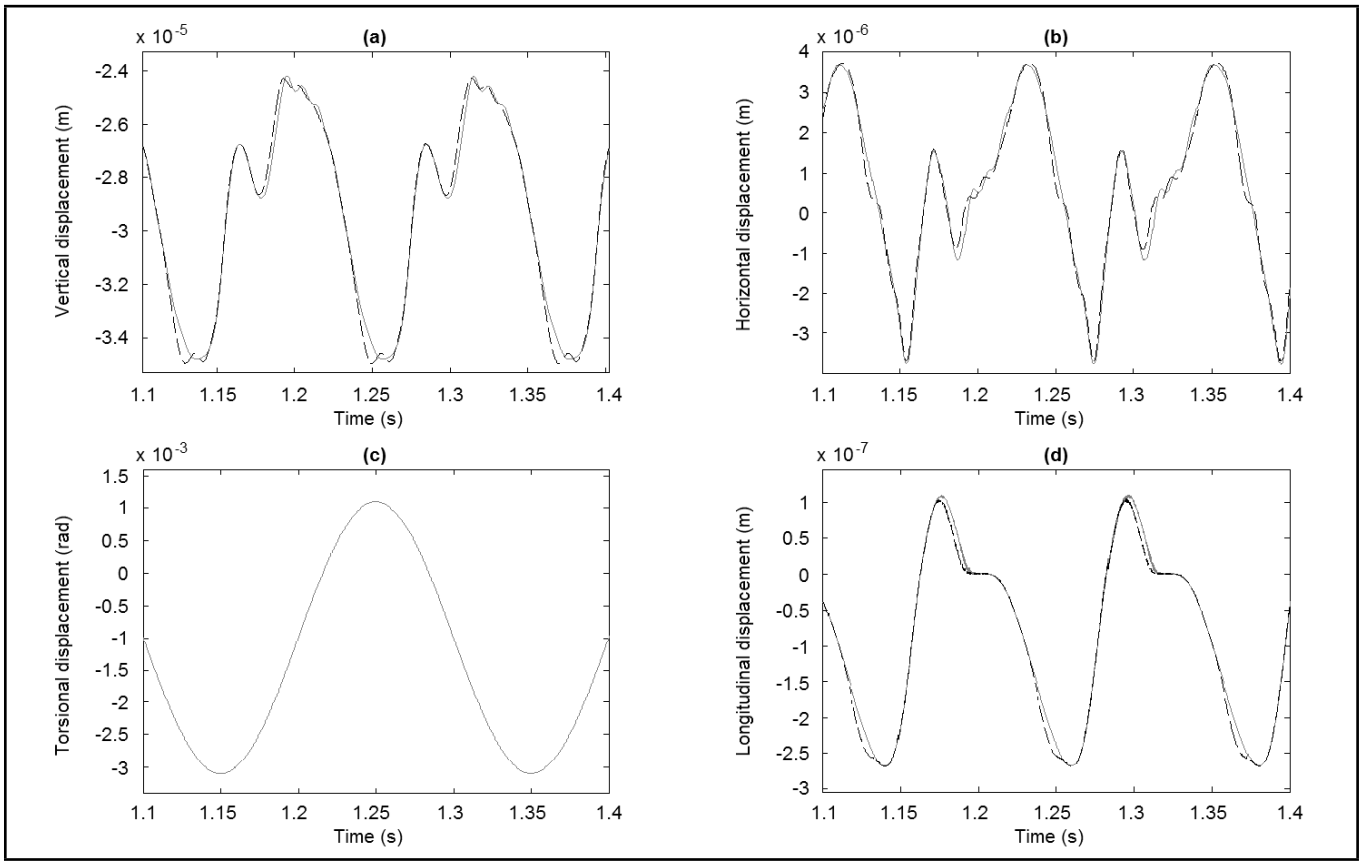

Figure 15. Time domain steady state responses for the cracked shaft with a transverse crack. Continuous line: CCLP model; dashed line: ICCLP model. (a) Vertical displacement, (b) Horizontal displacement, (c) Torsional displacement, and (d) Longitudinal displacement.

by using Fig. 11. According to this figure, the elements that are related to torsional direction—i.e. $c(1,3)$, $c(2,3)$, $c(3,3)$, and $c(3,4)$—are zero and are thus the same for the two models. Therefore, the two models show the same behaviour, as can be seen in Fig. 15(c). Figure 16 displays a comparison between the amplitude-frequency spectrums of the steady state responses of the shaft with respect to the two crack breathing models (i.e. CCLP and ICCLP). In this figure, the horizontal axis is the frequency (revolutions per minute), and the vertical axis is the log scale of amplitude (metres or radians). According to this figure, the frequency components of the responses are the same for the CCLP and ICCLP models. Furthermore, there is no difference between the torsional spectrums for CCLP and ICCLP models. In fact, they are coincident with each other. However there is a slight difference in the amplitude of the spectrums of the responses (except for the torsional response). It can be seen that by increasing the frequency, the difference between the amplitudes of the responses calculated by the two models also increases. Figure 17 identifies the reason for this. According to this figure, the difference between the amplitudes of the frequency components is observable, especially at high frequencies. In summary, the use of the two models for crack breathing discussed has no effect on the frequency components of the responses, but changes in the amplitude of the spectrums is apparent in some high frequencies.

7. CONCLUSIONS

In this paper, the dynamic behaviour of a cracked Jeffcott rotor has been investigated. The main scope of this work is to modify the existing breathing model. Using several contour plots over the crack surface, it has been shown that CCLP, which separates the open and closed parts of a breathing crack, cannot be considered perpendicular to the crack tip. A new breathing model—ICCLP—was introduced and showed that the results obtained are in good agreement with those proposed in the literature. The effects of ICCLP on the coefficients of the local flexibility matrix have also been investigated.

It is concluded that the value of the element of the crack compliance matrix is not equal for CCLP and ICCLP; it depends on the value of the crack rotation angle when the rotor in under steady state conditions.

The time response and frequency response of the system have been compared. It is shown that there are differences between the responses obtained from the two models. It was observed that when the value of the frequency increases, the difference between the amplitudes of the responses computed from the two models also increases.

REFERENCES

[1] Georgantzinos, S. K. and Anifantis, N. K. An insight into the breathing mechanism of a crack in a rotating shaft, *Journal of Sound and Vibration*, **318** (1–2), 279–295, (2008).

[2] Papadopoulos, C. A. The strain energy release approach for modeling cracks in rotors: A state of the art review, *Mechanical Systems and Signal Processing*, **22** (4), 763–789, (2008).

[3] Papadopoulos, C. A. and Dimarogonas, A. D. Stability of cracked rotors in the coupled vibration mode, *Journal*

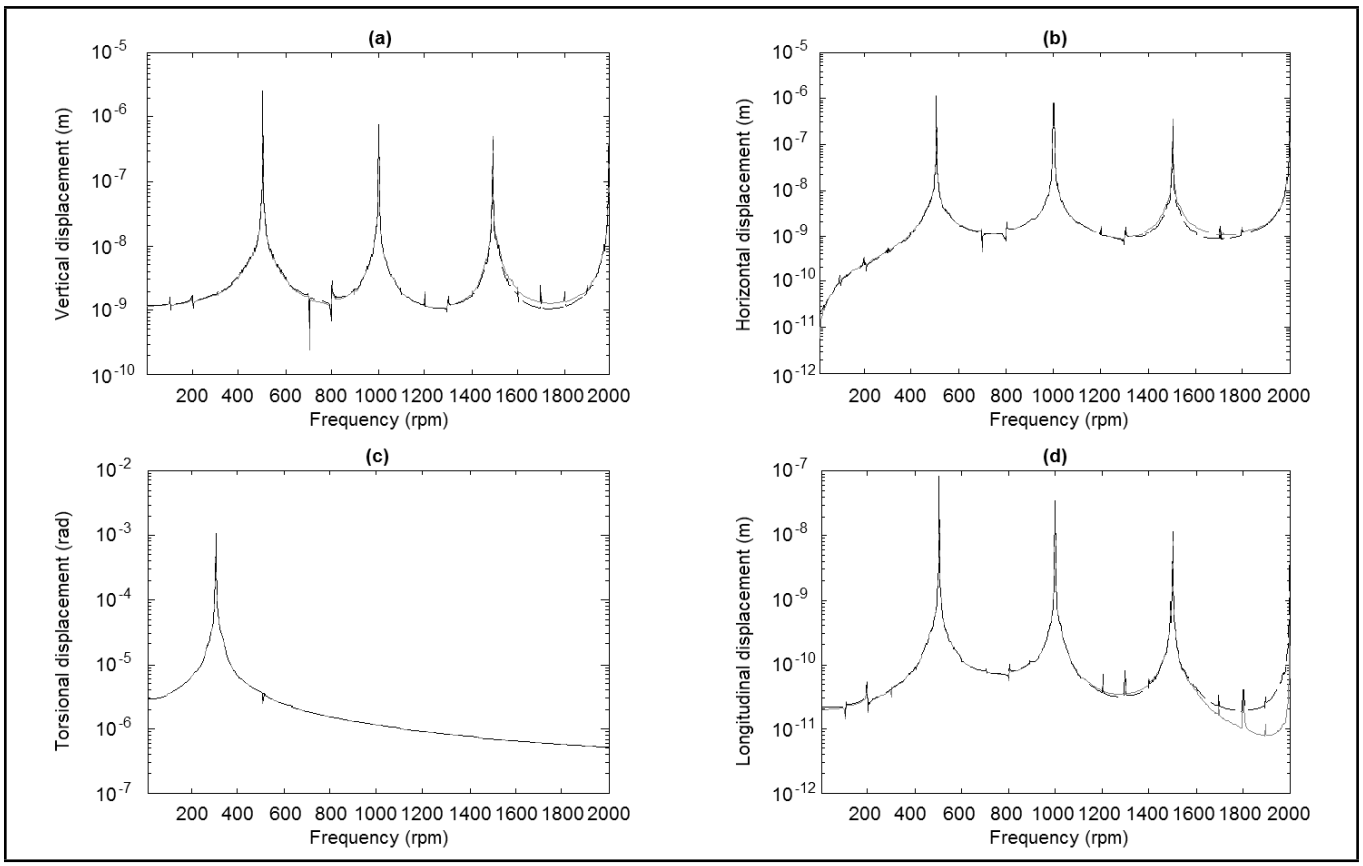

Figure 16. Comparison between amplitude-frequency spectrums of steady state responses of the shaft with respect to two crack breathing models: CCLP and ICCLP. (a) Vertical displacement, (b) Horizontal displacement, (c) Torsional displacement, and (d) Longitudinal displacement. Continuous line: CCLP model; dashed line: ICCLP.

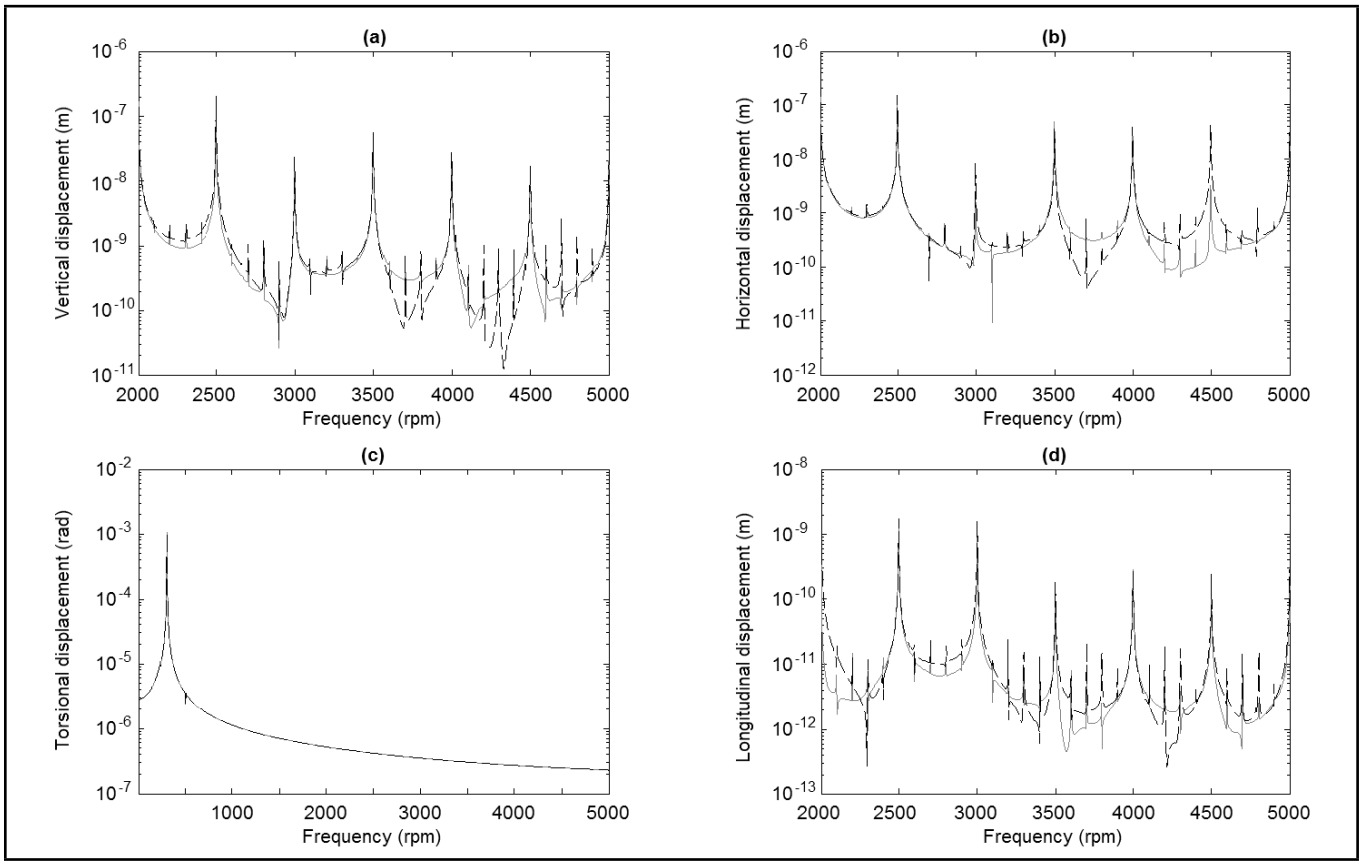

Figure 17. Comparison between amplitude-frequency spectrums of steady state responses of the shaft with respect to two crack breathing models: CCLP and ICCLP. (a) Vertical displacement, (b) Horizontal displacement, (c) Torsional displacement, and (d) Longitudinal displacement. Continuous line: CCLP model; dashed line: ICCLP.

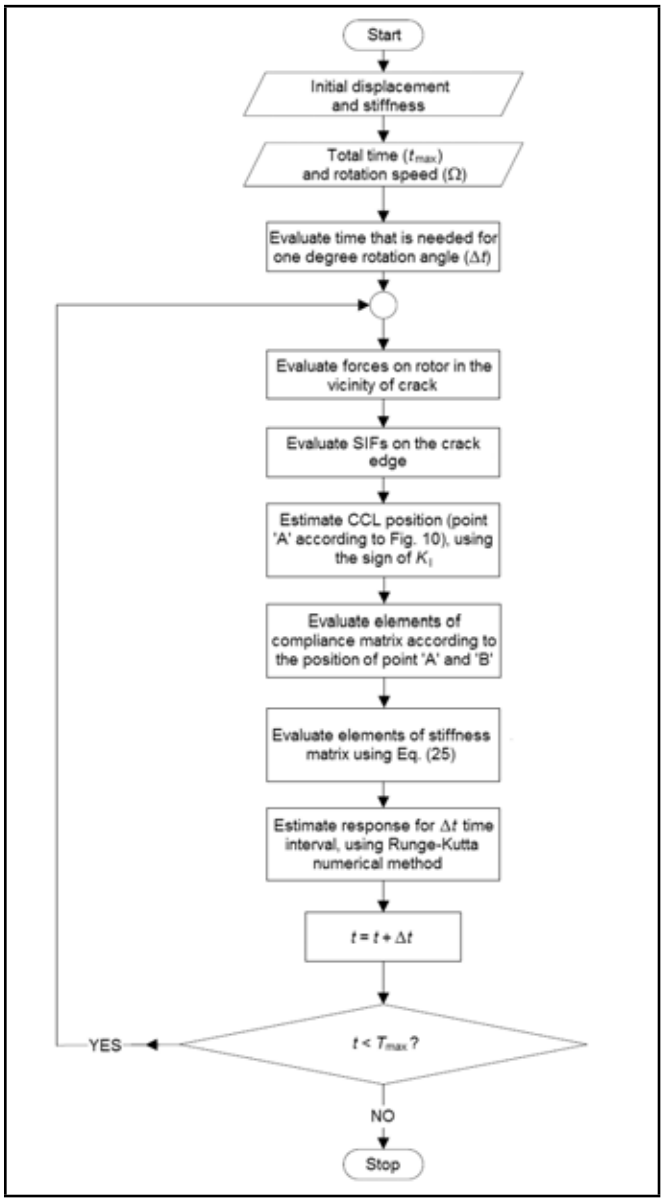

Figure 13. Solution procedure used in the numerical process.

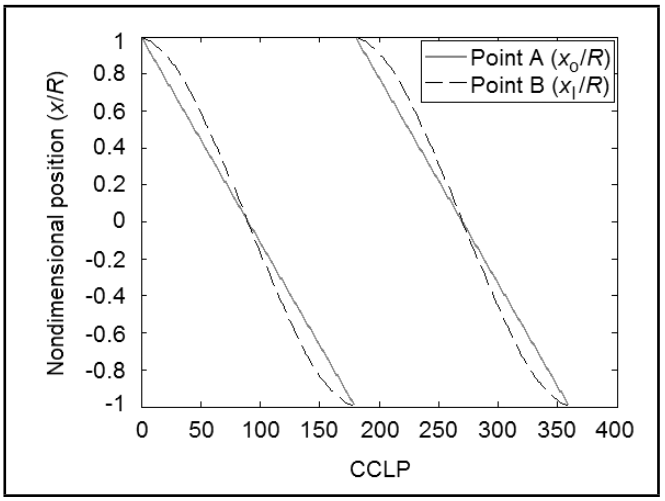

Figure 14. Non-dimensional position of point A and B versus rotor rotation angle. Continuous line: point A; dashed line: point B.

of Vibration, Acoustics, Stress, and Reliability in Design, **110** (3), 356–359, (1988).

[4] Wauer, J. Modeling and formulation of equations of motion for cracked rotating shafts, *International Journal of Solids and Structures*, **26** (8), 901–914, (1990).

[5] Jun, O. S., Eun, H. J., and Earmme, Y. Y. Modeling and vibration analysis of a simple rotor with a breathing crack, *Journal of Sound and Vibration*, **155** (2), 273–290, (1992).

[6] Dimarogonas, A. D. and Papadopoulos, C. A. Vibration of cracked shafts in bending, *Journal of Sound and Vibration*, **91** (4), 583–593, (1983).

[7] Papadopoulos, C. A. and Dimarogonas, A. D. Coupled longitudinal and bending vibrations of a rotating shaft with an open crack, *Journal of Sound and Vibration*, **117** (1), 81–93, (1987).

[8] Grabowski, B. *The vibrational behaviour of a rotating shaft containing a transverse crack*, O. Mahrenholtz (Ed.), Springer Press, (1984).

[9] Mayes, I. W. and Davies, W. G. R. Analysis of the response of a multi-rotor-bearing system containing a transverse crack in a rotor, *Journal of Vibration, Acoustics, Stress, and Reliability in Design*, **106**, 139–145, (1984).

[10] Papadopoulos, C. A. and Dimaragonas, A. D. Stability of cracked rotors in the coupled vibration mode, *Journal of Vibration, Acoustics, Stress, and Reliability in Design*, **110**, 356–359, (1988).

[11] Changhe, L., Bernasconi, O., and Xenophontidis, N. A generalized approach to the dynamics of cracked shafts, *Journal of Vibration, Acoustics, Stress, and Reliability in Design*, **111** (3), 257–263, (1989).

[12] Ballo, I. Non-linear effects of vibration of a continuous transverse cracked slender shaft, *Journal of Sound and Vibration*, **217** (2), 321–333, (1998).

[13] Darpe, A. K., Gupta, K., and Chawla, A. Coupled bending, longitudinal and torsional vibrations of a cracked rotor, *Journal of Sound and Vibration*, **269** (1–2), 33–60, (2004).

[14] Bachschmid, N., Pennacchi, P., and Tanzi, E. Some remarks on breathing mechanism, on non-linear effects and on slant and helicoidal cracks, *Mechanical Systems and Signal Processing*, **22** (4), 879–904, (2008).

[15] Sekhar, A. S. Vibration characteristics of a cracked rotor with two open cracks, *Journal of Sound and Vibration*, **223** (4), 497–512, (1999).

[16] Darpe, A. K., Gupta, K., and Chawla, A. Dynamics of a two cracked rotor, *Journal of Sound and Vibration*, **259** (3), 649–675, (2003).

[17] Darpe, A. K. A novel way to detect transverse surface crack in a rotating shaft, *Journal of Sound and Vibration*, **305** (1–2), 151–171, (2004).

[18] Lin, Y. and Chu, F. The dynamic behavior of a rotor system with a slant crack on the shaft, *Mechanical Systems and Signal Processing*, **24** (2), 522–545, (2010).

[19] Tada, H., Paris, H., and Irwin, G. R. *The stress analysis of cracks*, Professional Engineering Publishing, (2000).

Generation of Acoustic Disturbances in Supersonic Laminar Cavity Flows

Weipeng Li

Dept. of Aeronautics and Astronautics, Shanghai Jiaotong University, Shanghai, 200-240, China

Taku Nonomura and Kozo Fujii

Institute of Space and Astronautics Science/JAXA, Sagamihara, Kanagawa, 252-5210, Japan

(Received 13 May 2012; accepted 20 October 2014)

The generation of acoustic disturbances in supersonic laminar cavity flows is investigated by large-eddy simulations of supersonic laminar flow ($M = 1.2$, 2.0, and 3.0) past a rectangular cavity with a length-to-depth ratio of 2. Results suggest that well-originated large-scale vortical structures with strong spanwise coherence are present in the shear layer. Compressibility effects have significant impacts on the shear-layer development and the fluctuation properties. The dominant mechanism for the acoustic radiation in supersonic laminar cavity flows is shown to be associated with the successive passage of large-scale vortices over the cavity trailing edge. It is found that Mach waves radiated from the cavity shear layer may have significant contributions for the noiseradiation in terms of enhancing the strength of the feedback compression waves.

1. INTRODUCTION

Supersonic flow past cavities has been studied for many years, both in practical and academic interest. In general, when the length-to-depth ratio (L/D) of a rectangular cavity is less than ten, the shear layer reattaches on the cavity aft wall. This type of cavity flow is termed open cavity flow.[1,2] An undesirable problem in open cavity flow is the existence of intense resonant noise. For instance, a resonance with a sound pressure level of 160 decibels is observed in a cavity flow at Mach number 2.0.[3] The resonant noise may harm the nearby equipment and the environment, for example, by causing structural vibrations and fatigue, adverse effects on store separation, and undesirable noise.

Reviews of cavity flows were conducted by Grace, Colonius, Rockwell and Naudascher,[4] and Lawson and Barakos.[5] The driving mechanism of cavity oscillations is widely regarded as a feedback mechanism between shear-layer instabilities and acoustic disturbances. It was first proposed by Powell for the study of edge tones.[6] In 1964, Rossiter developed a semi-empirical formula to predict the resonance frequencies based on his extensive experimental data with freestream Mach number within the range of 0.5 and 1.2.[7] Heller et al. improved Rossiters formula by introducing a temperature recover factor.[8] A typical feedback cycle consists of four key procedures: (1) the shear layer near the leading edge of the cavity is excited by acoustic disturbances, which leads to the generation of discrete vortices; (2) the vortices grow large as they convect downstream and eventually impact on the cavity trailing edge; (3) feedback compression waves (upstream-traveling) are radiated near the cavity trailing edge; and (4) the feedback compression waves propagate upstream and excite the shear layer again. Then, the feedback cycle is closed.

Despite the fact that the feedback mechanism itself has been well established and accepted, the mechanism driving the self-sustained oscillations in supersonic cavity flows is still not precisely resolved. One of the most important factors is the generation of acoustic disturbances near the downstream cavity lip. Rossiter observed that discrete vortices are shed periodically from the leading edge of the cavity and convect downstream until they encounter the downstream cavity lip.[7] He assumed that the passage of vortices over the trailing edge is responsible for the acoustic radiation. Heller and Bliss emphasized that discrete vortices were not usually observed in their experiment with a Mach number varying from 0.8 to 2.0.[9] They stated that the generation of acoustic disturbances is caused by the periodic mass addition and removal near the cavity trailing edge. Zhang reported that the compression wave emission is related to the shear layer deflection, which, in turn, is associated with the vortex production and convection.[10] By description of an oscillation cycle, Tam et al. stated that the upstream-travelling compression wave is generated by a pressure wave reflection at the bottom aft wall.[11] An experimental study by Schmit et al. showed that the entrained waves are the start of the feedback loop process rather than the shear layer impingement on the downstream cavity wall, as many references have indicated.[12] Supersonic laminar flow past cavities usually exists over the orbiter launch/reentry trajectories; however, limited investigations have been conducted. Krishnamurty experimentally observed that the laminar cavity flow produced louder resonant noise than that of turbulent cavity flow.[13] Heller et al. reported that no resonance was observed in the turbulent cavity flow at Ma3.0; however, a strong resonant peak occurred in the laminar cavity flow.[14] Based on large-eddy simulations of high subsonic laminar cavity flow, Gloerfelt et al. stated that the strong unsteadiness of the internal recirculation flow can be associated with the possible vortex coalescence.[15] The physical mechanisms underlying the self-sustained oscillations in supersonic laminar cavity flows are in need of more study, especially on the generation of acoustic disturbances.

This paper aims to address the generation mechanism of

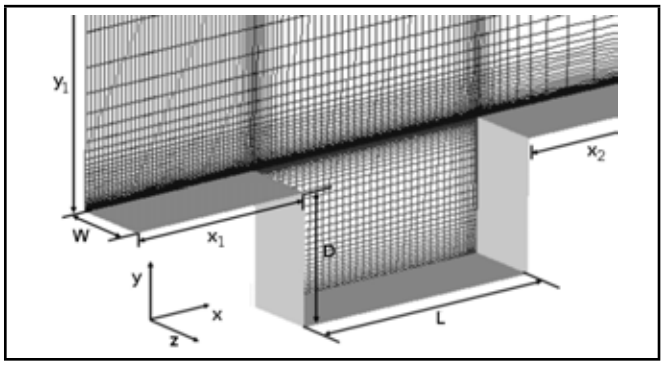

Figure 1. Computational grids (shown every other five points).

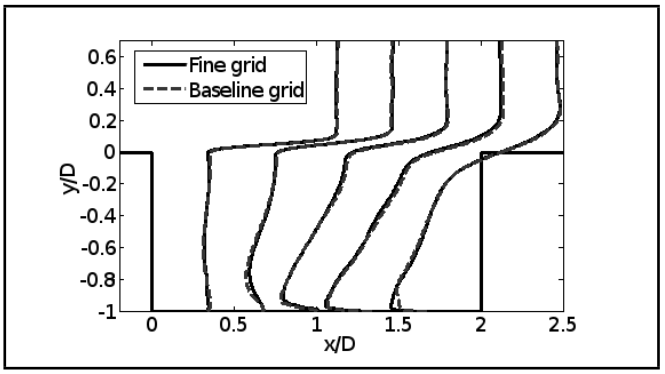

Figure 2. Distributions of time-averaged streamwise velocities.

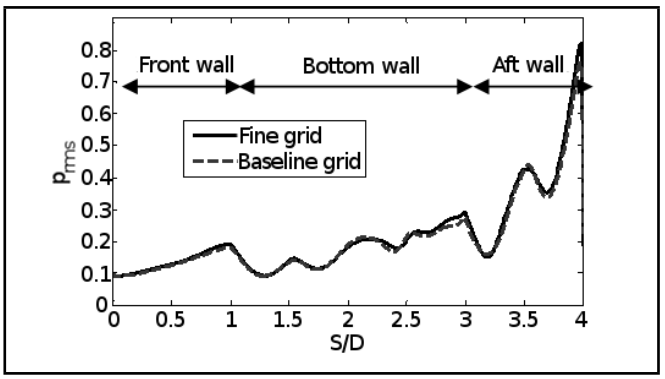

Figure 3. Distributions of root-mean-square of pressure fluctuations along the internal cavity walls.

acoustic disturbances in supersonic laminar cavity flows. An introduction of numerical methods is given in Section 2. In Section 3, we describe the features of flow fields with an increase of the freestream Mach number. In Section 4, the generation of acoustic disturbance in the vicinity of the downstream cavity lip is investigated. This paper will be concluded in Section 5.

2. NUMERICAL METHODS

2.1. Flow Conditions

Supersonic flows past a cavity of $L/D = 2$, $W/D = 0.6$ were numerically studied, where L is the length of the cavity, W is the width of the cavity, and D was the depth of the cavity. Three simulations were conducted with freestream Mach numbers of 1.2, 2.0, and 3.0. The Reynolds number based on the cavity depth was set to 10^5. The reference velocity was set as the sound speed. The boundary layer thickness δ_0 was $0.075D$.

2.2. Numerical Methods

The governing equations were three-dimensional compressible Navier-Strokes equations in conservative form. Implicit large-eddy simulations (ILES) were conducted, which rely on numerical dissipation to dissipate high-frequency turbulent energy. In order to meet the low-dispersive and low-dissipative requirements of computational aeroacoustics (CAA), a modified seventh-order weighted compact nonlinear scheme (WCNS) was employed for spatial derivatives.[16–18] The numerical fluxes were evaluated by the simple high-resolution upwind scheme (SHUS) which was a family of advection-upstream-splitting-method (AUSM) type schemes.[19] Viscous terms were evaluated by a sixth-order central difference scheme. Alternate directional implicit symmetric Gauss-Seidel (ADI-SGS) scheme was applied for time integration.[20] A second-order temporal accuracy is obtained using three Newton-like sub-iterations. The CFL number was equal to 1.2.

The computational domain consisted of inside cavity region and upper cavity region, as shown in Fig. 1. Structured grids were adopted, and the total grid points were about 7.0 million. The grid had $200\times169\times80$ points inside the cavity and $360\times150\times80$ points in the region above the cavity. The origin of the coordinate system was located at the middle of the leading-edge lip. The length from the inflow boundary to the leading edge x_1 was equal to $1.5D$, and a length of $x_2 = 4D$ was extended from the trailing edge to the outflow boundary. A length of $4D$ was extended in the vertical direction, and no buffer region was set because of supersonic freestream. The grid spacing was refined in the near-wall regions. The minimum and maximum grid spacing was $0.0005D$ and $0.012D$, respectively. The Blasius profile was imposed for the initial inflow. No-slip adiabatic wall boundary condition is imposed for all wall boundaries. Zero-gradient pressure condition was employed at the outflow and upper boundary. Periodic boundary condition was given in the spanwise direction.

2.3. Validations

The baseline grid was refined by a factor of 1.333 in each direction for a validation of grid convergence. The fine grid contains 18.3 million grid points in total. Flow conditions were the same as those in the Ma2.0 case. Figure 2 shows the distributions of the time-averaged streamwise velocities. It indicates that the simulation with the baseline grid had almost the same velocity profiles as that with the fine grid. Figure 3 shows the distributions of root-mean-square of pressure fluctuations p_{rms} along the internal cavity walls. Apparently, a fairly good agreement is calculated between the two simulations.

Figure 4 shows the pressure spectra at the mid-point of the cavity front wall (P_1). The sound pressure level (SPL) was defined by $SPL = 20log_{10}(p/p_{ref})$, where $p_{ref} = 2.0 \times 10^{-5}[Pa] \times p_\infty$. The standard Strouhal number St was defined by $St = fL/U_\infty$, where f is frequency and U_∞ is freestream velocity. The resonance frequencies observed with the baseline grid and fine grid agree well with each other and also match with the experimental study of Zhuang et al.

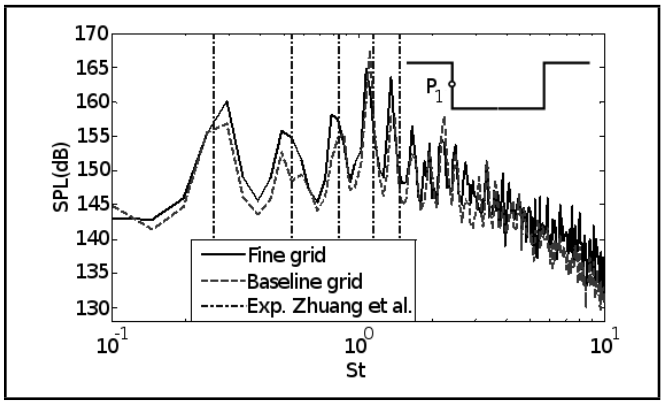

Figure 4. Pressure spectra at the mid-point of the cavity front wall.

($M_\infty = 2.0$, $ReD = 5.4\times10^5$,turbulent inflow).[21] The differences in the SPL amplitude do not influence our conclusions since the objective of this paper is to address the fundamental physics rather than to accurately predict the cavity tones. The following simulations are conducted with the baseline grid.

3. FLOW FIELDS

Snapshots of instantaneous flow fields are shown in Fig. 5. Large-scale vortical structures with strong spanwise coherence are present in the cavity shear layer. They convect downstream with their own trajectories and speeds. Plenty of small-scale vortical structures are observed in the shear-layer region as well as the internal recirculation region. It shows a good turbulence resolution with the high-order numerical schemes. It is noted that, in our preliminary two-dimensional simulations, the cavity shear layer consisted of much larger size of vortical structures, and behaves more violently than that in these three-dimensional simulations.

Figure 6 shows the variation of vorticity thickness between cavity lips, and its slope was used to measure the shear-layer growth rate. Dashed lines are used to indicate linear shear-layer growth rates. Basically, the growth of the cavity shear layer is similar to that of free shear layers. After the upstream boundary layer separated from the leading edge, the cavity shear layer started to grow due to the Kelvin-Helmholtz instabilities. In this region, the cavity shear layer was dominated by a transition procedure from laminar inflow to turbulence, and a slow shear-layer growth rate appeared near the cavity leading edge which is quite different from that in turbulent cavities.[22] This transition procedure was impacted by compressibility effects, that is, higher-speed inflow corresponds to a longer distance to complete this transition procedure. In the Ma3.0 case, the shear-layer growth rate remains at low values across the cavity lips, and it seems that the transition procedure does not complete within the cavity length. However, in the Ma1.2 and Ma2.0 cases, the shear-layer growth rate resumed a standard value after the transition procedure, indicating that the cavity shear layer grows linearly and obeys a self-similarity rule which can always be observed in free shear layers. Three-dimensional characteristics are dominant in this region. Near the cavity trailing edge, the shear-layer growth rate drops quickly because of the distortion of the mean velocity.

Two differences may exist between the cavity shear layer and free shear layers: (1) the cavity shear layer is subjected to strong acoustic disturbances, which lead to strong spanwise coherent vortices near the leading edge. However, the free shear layers at supersonic speed are generally dominated by oblique modes, (2) the interactions between the cavity shear layer and recirculation flows cannot be omitted in the supersonic cavity flows since high-speed recirculation flow exists inside the cavity.[23]

In order to assess the fluctuation properties, contours of turbulence kinetic energy (TKE) were plotted in Fig. 7. Great velocity distortions and deformations are generated near the

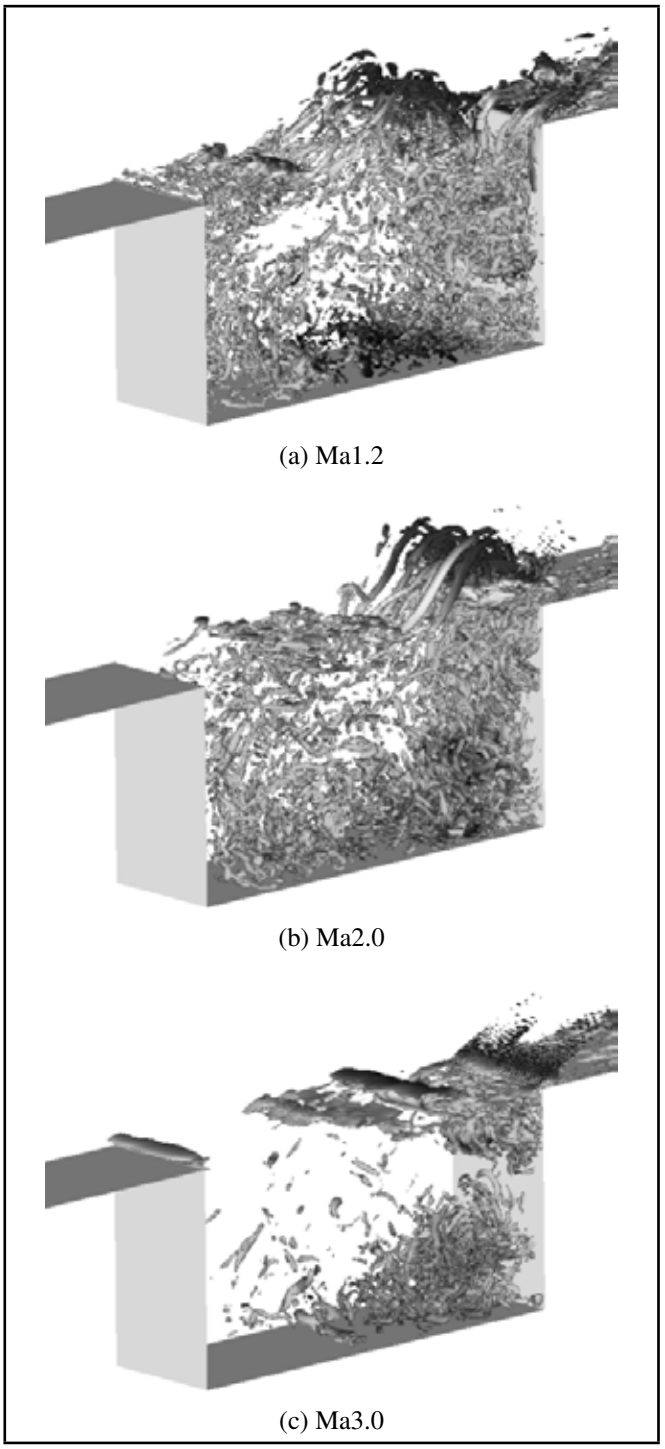

(a) Ma1.2

(b) Ma2.0

(c) Ma3.0

Figure 5. Snapshots of instantaneous flow-fields. Iso-surface of the second invariant of velocity gradient tensors, $Q_{2nd} = 50(a_\infty/D)^2$; colored with streamwise velocity, $-0.5 < u/u_\infty < 1$.

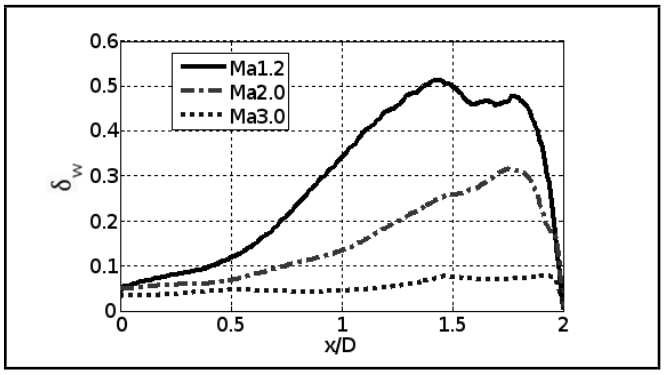

Figure 6. Variations of vorticity shear-layer thickness.

cavity trailing edge due to the impingement of the shear layer, corresponding high values of TKE near the cavity trailing edge. The distribution of TKE in the Ma1.2 case has broad distributions in the vertical direction, while the fluctuations in the Ma3.0 case are mostly constrained in a thin layer. This result may be associated with the compressibility effects of high-speed flows.

4. GENERATION OF ACOUSTIC DISTURBANCES

In our previous work, the mechanism driving supersonic laminar cavity oscillations has been verified to be a feedback mechanism between discrete vortices and acoustic disturbances.[24] The acoustic disturbances in terms of feedback (upstream-travelling) compression waves were radiated from the region near the cavity trailing edge. But their generation mechanism was discussed less. In the present study, we attempt to demonstrate that the generation of acoustic disturbances is highly associated with two mechanisms: the successive passage of large-scale vortices over the trailing edge and the reflection of Mach waves. A schematic of large-scale vortices and Mach waves is plotted in Fig. 8. In the Ma2.0 and Ma3.0 cases, the large-scale vortices convect at supersonic speed, and intense Mach waves propagate with the large-scale vortices; in the Ma1.2 case, no Mach wave is radiated from the cavity shear layer since the convection velocity of large-scale vortices is at subsonic speed.[24]

4.1. The Passage of Large-scale Vortices over the Trailing Edge

Rossiter assumed that the passage of large-scale vortices over the cavity trailing edge was responsible for the acoustic radiation, but no quantitative discussion was given.[7] Here, we attempt to provide more quantitative evidence by use of a phase-averaging analysis.[25]

Figure 9 shows the convection trajectories of vortex cores from the leading edge to the trailing edge of the cavity. The vortex cores are marked by detecting the maximum value of Q criterionin the phase-averaged flow fields.[24] The upstream boundary-layer rolls up into two well-originated vortices (S_1 and S_2) in phases of each acoustic excitation. Vortex pairing occurs in the Ma1.2 case. Based on our animations and vortex trajectories in $x-y$ axes, the vortex S_1 goes inside the cavity and is not critical for the generation of acoustic disturbances.

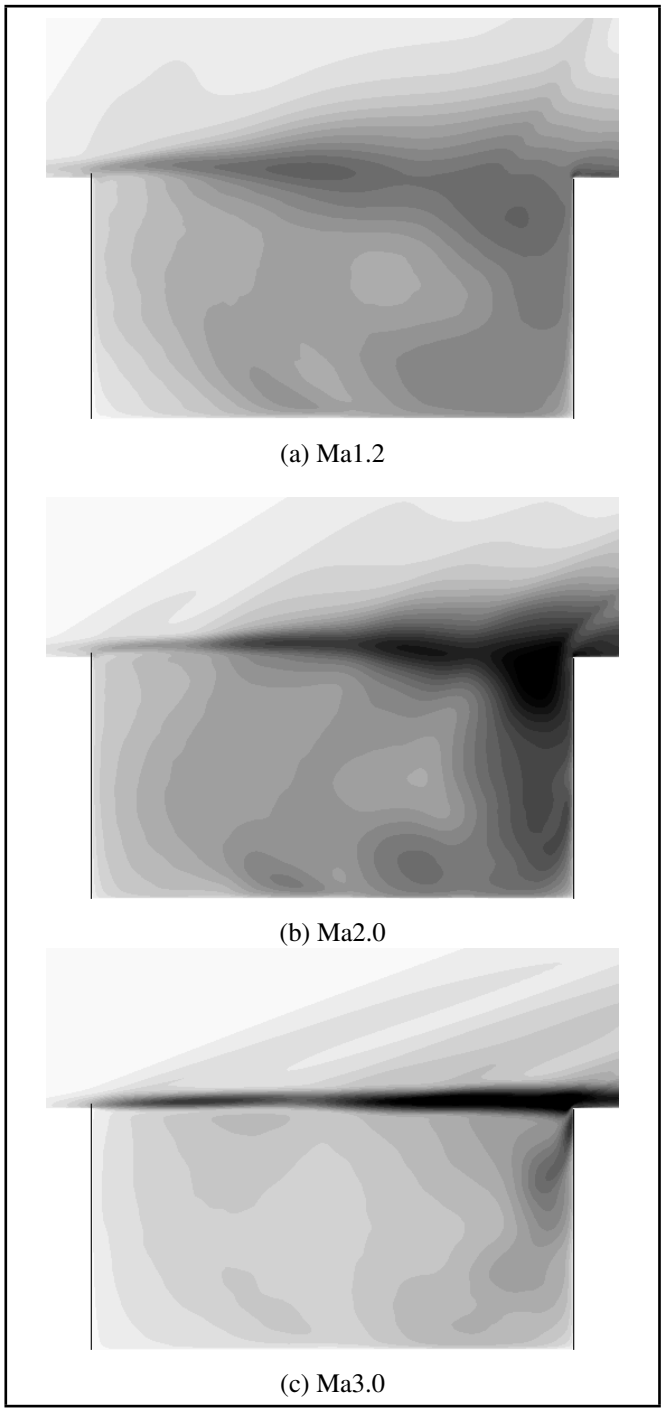

(a) Ma1.2

(b) Ma2.0

(c) Ma3.0

Figure 7. Contours of turbulence kinetic energy ($0 < TKE < 0.5_\infty a_\infty^2$).

Therefore, we mainly focus on the impinging and passage of vortex S_2. A quadratic polynomial is used to interpolate the convection trajectories of vortex S_2. It showed that the vortex S2 impinges on the trailing edge at a phase angle of approximately $-2/15\pi$, $-2/15\pi$ and $-1/30\pi$ in the Ma1.2, Ma2.0 and Ma3.0 case, respectively. The vortex S_1 in the Ma3.0 case is not shown since it is somehow too flat to be detected. Figure 10 shows pressure oscillations at P_2 (depicted in Fig. 8). The P_2 is selected among several points close to the trailing-edge lip. All the points have similar variation tendencies but are different in the amplitude of the pressure.

In Fig. 9 and 10 the lowest pressure values occur when the cores of the vortex S_2 impinges on the cavity trailing-edge lip, and the lowest pressure values are smaller than the freestream

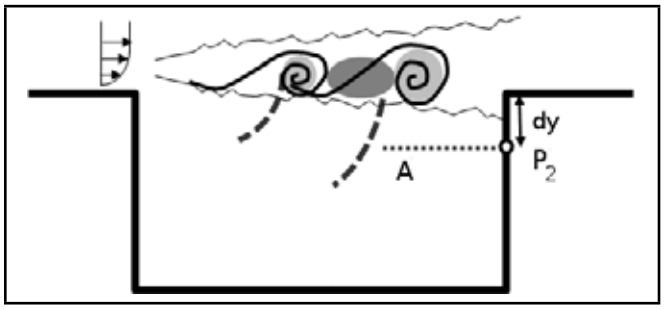

Figure 8. Schematic of large-scale vortices and Mach waves.

pressure. It indicates that the pressure decreasing is related to the vortices impingement. After the core of the vortex S_2 passes over the cavity, the pressure value begins to increase. The feedback compression wave is generated when the large-scale vortices passes over the trailing edge, rather than when they impinge on the trailing edge.

A more physical explanation is given here. Before the vortices impingement low pressure values are associated with the cores of the vortices.[26,27] The pressure gradient near the vortices cores is balanced with the centrifugal force of large-scale vortices. When the large-scale vortices impinge on the trailing edge, large velocity distortions and deformations are produced. The balance between the pressure gradient and the centrifugal force of vortices is broken up. The low pressure values are consequently no longer associated with the large-scale vortices and begin to spread near the aft wall. After the vortices impingement the pressure begins to increase since a stagnation region exists in the adjacent point of two neighbor vortices. In summary, the successive passage of large-scale vortices over the cavity trailing edge, which are associated with periodic vorticity productions and pressure pulses near the cavity trailing-edge lip, results in the generation of acoustic disturbances represented by internal upstream-traveling compression waves.

4.2. Reflection of Mach Waves

Figures 11 and 12 are plotted to reveal that the reflection of Mach waves occurs in the Ma2.0 and Ma3.0 cases. Phases-averaged flow fields are used. The background contours are the divergence of velocity ($-2 < div\mathbf{u} < -0.1$), and black contour lines represent the second-order invariant of velocity gradient tensors ($2(a_\infty/D)^2 < Q_{2nd} < 20(a_\infty/D)^2$). Following the definition in Li et al., the Mach wave and feedback (upstream-travelling) compression wave are named as III and IV, respectively.[24] As shown in Fig. 11(a), a Mach wave III propagates downstream associated with the vortex S_2. As time passes, the Mach wave III encounters the cavity aft wall, and a small part of it is reflected off the aft wall, as illustrated in Fig. 11(b). Point R is the reflection position. This reflection procedure continues as long as the Mach wave travels downstream. In Fig. 11(c), an upstream-traveling feedback compression wave IV is generated near the cavity trailing edge. Figure 11(d) shows that a large part of the Mach wave III has been reflected off the aft wall, and the feedback compression wave IV is leaving the aft wall. Similar results are shown in Fig.12 for the Ma3.0 case. This phenomenon is not observed in the Ma1.2 case since no Mach wave is radiated.

Figure 13 shows the propagation of compression waves

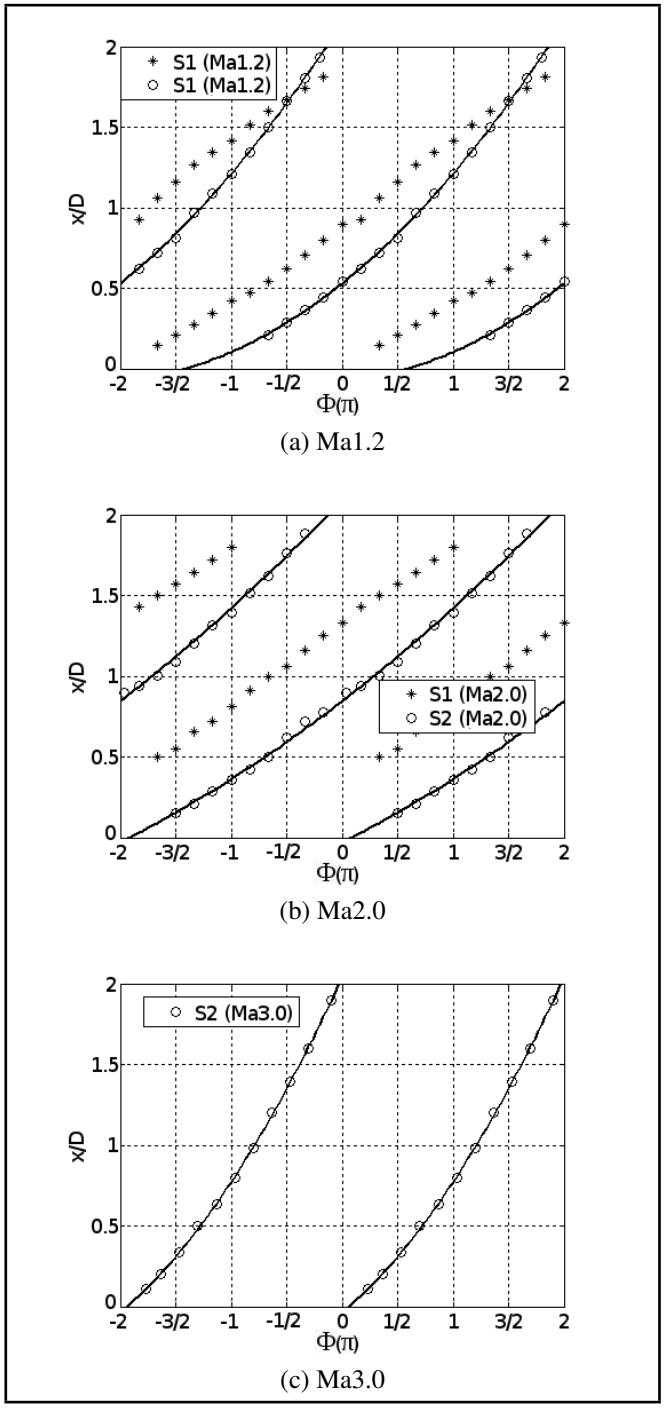

Figure 9. Convection trajectories of vortices in streamwise direction.

through Line A (depicted in Fig. 8). The x-coordinates are the streamwise distances, and the y-coordinates represent phase angles. The contours in Fig. 13 are the variations of $div\mathbf{u}$ along Line A. Roughly, the angle α and β can indicate the streamwise velocity of the Mach wave propagating toward the aft wall and the feedback compression wave propagating against the aft wall, respectively. Based on the $x-t$ diagrams in Fig. 13(b) and Fig. 13(c), it is indicates that the phase lag between the Mach wave reaching the aft wall and the feedback compression wave leaving the aft wall are very small. It can be concluded that the reflection of Mach wave is one important factor for the generation of acoustic disturbances in the Ma2.0 and Ma3.0 cases. However, it is not the only reason because the feedback compression waves have higher strength than the

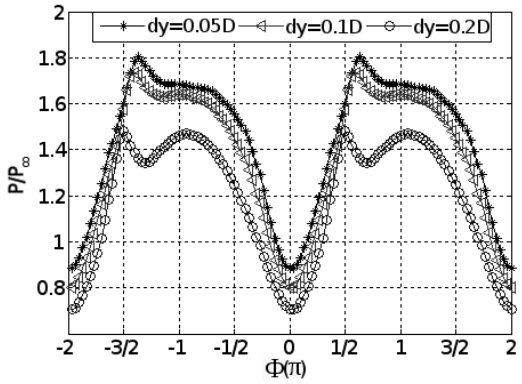

(a) Ma1.2

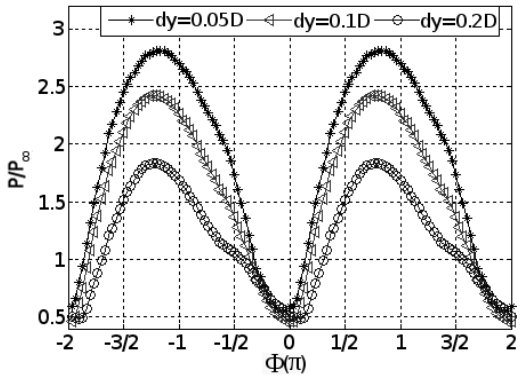

(b) Ma2.0

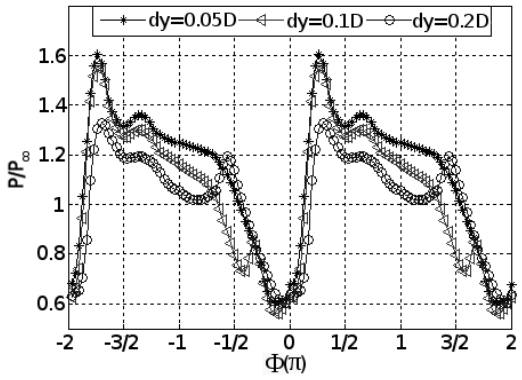

(c) Ma3.0

Figure 10. Pressure oscillations at P_2.

Mach waves, and no Mach wave is radiated in the Ma1.2 case in which strong self-sustained oscillations are also exhibited.

It is difficult to distinguish the action caused by the passage of large-scale vortices and the reflection of Mach wave in the Ma2.0 and Ma3.0 cases. In the Appendix, a two-dimensional simulation of a laminar free shear layer subjected to an artificial acoustic source is performed. Results suggest that the successive passage of large-scale vortices over the tailing edge is the dominant reason for the generation of acoustic disturbances, but the Mach waves could significantly enhance the strength of the acoustic disturbances and cavity instabilities. In engineering and presumably in other fields, controlling the upstream laminar flow by facilitating shear-layer three-dimensionality would be desirable in order to suppress the contributions of Mach waves and reduce the pressure oscillations inside the cavity.

5. CONCLUSIONS

Supersonic laminar flows ($M = 1.2/2.0/3.0$ and $Re_D = 10^5$) past a rectangular cavity ($L/D = 2$) are studied with high-resolution implicit large-eddy simulations. Results show that a transition procedure from laminar inflow to turbulence exists near the leading edge of the cavity before the shear layer resumes a linear growth rate. Compressibility effects have significant impacts on the shear-layer development and fluctuation properties. Two mechanisms are addressed for the generation of acoustic disturbances in supersonic laminar cavity flows. First, the successive passage of large-scale vortices over the cavity trailing edge, associated with periodical vorticity productions and pressure pulses, is the dominant reason for the acoustic radiation in the vicinity of the cavity trailing edge. Secondly, Mach waves may be radiated from the cavity shear layer once the large-scale vortices convect at supersonic speed with respect to the sound speed of surrounding streams. The reflection of Mach waves could take place at the cavity aft wall and have large contributions for the acoustic radiation in terms of enhancing the strength of the feedback compression waves.

REFERENCES

[1] Grace, S. M. An Overview of Computational Aeroacoustic Techniques Applied to Cavity Noise Prediction, *AIAA Paper* 2001-0510.

[2] Colonius, T. An Overview of Simulation, Modeling, and Active Control of Flow/acoustic Resonance in Open Cavities, *AIAA Paper 2001-0076*, (2001).

[3] Zhuang, N. Alvi, F. S., Alkislar, M. B., and Shih, C. Supersonic Cavity Flows and Their Control, *AIAA Journal*, **44**(9), 2118–2128, (2006).

[4] Rockwell, D. and Naudascher, E. Review: Self-Sustaining Oscillations of Flow Past Cavities, *Journal of Fluids Engineering*, **100**(2), 152–165, (1978).

[5] Lawson, S. J. and Barakos, G. N. Review of Numerical Simulations for High-speed, Turbulent Cavity Flows, *Progress in Aerospace Science*, **47**(3), 186–216, (2011).

[6] Powell, A. On the Edge Tone, *Journal of the Acoustical Society of America*, **33**(395), 395–409, (1961).

[7] Rossiter, J. E. Wind-Tunnel Experiments on the Flow over Rectangular Cavities at Subsonic and Transonic Speeds, *Aeronautical Research Council Reports and Memoranda*, 3438, (1964).

[8] Heller, H. H., Holmes, G., and Covert, E. Flow-induced Pressure Oscillations in Shallow Cavities, AFFDL TR-70-104.

[9] Heller, H. H. and Bliss, D. B. The Physical Mechanism of Flow-induced Pressure in Cavities and Concepts for Their Suppression, AIAA Paper 1975–491.

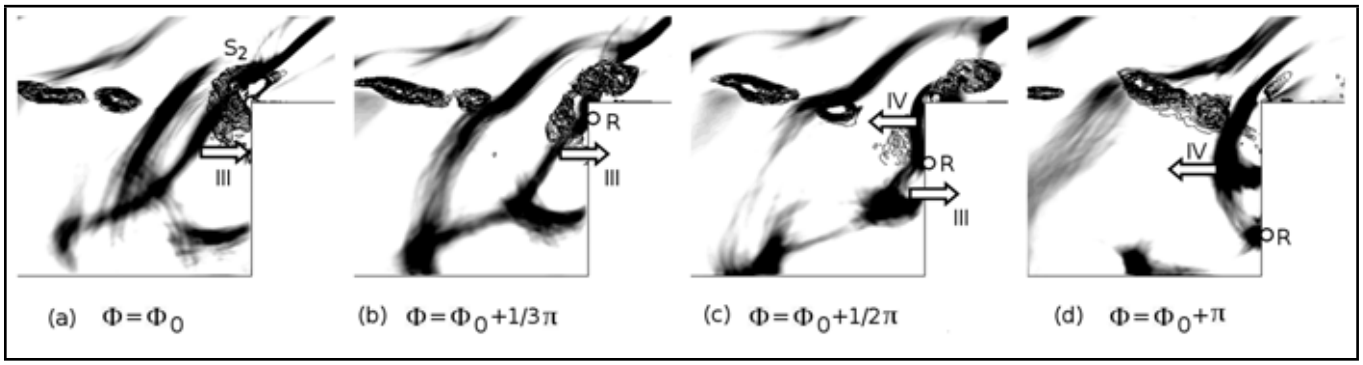

Figure 11. Reflection of Mach waves in Ma2.0 case. Background contours represent the divergence of velocity $(-2 < div\mathbf{u} < -0.1)$, and black contour lines represent the second-order invariant of velocity gradient tensors $(2(a_\infty/D)^2 < Q_{2nd} < 20(a_\infty/D)^2)$.

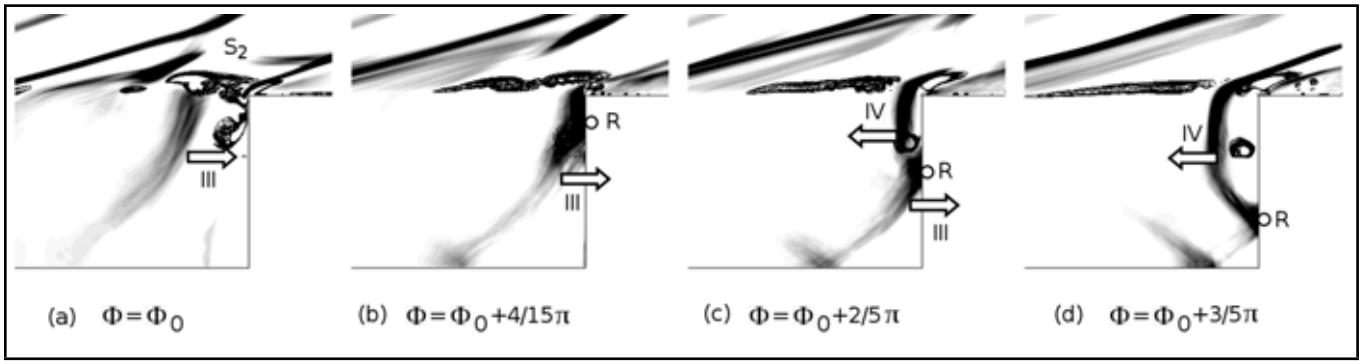

Figure 12. Reflection of Mach waves in the Ma3.0 case. Background contours represent the divergence of velocity $(-2 < div\mathbf{u} < -0.1)$, and black contour lines represent the second-order invariant of velocity gradient tensors $(2(a_\infty/D)^2 < Q_{2nd} < 20(a_\infty/D)^2)$.

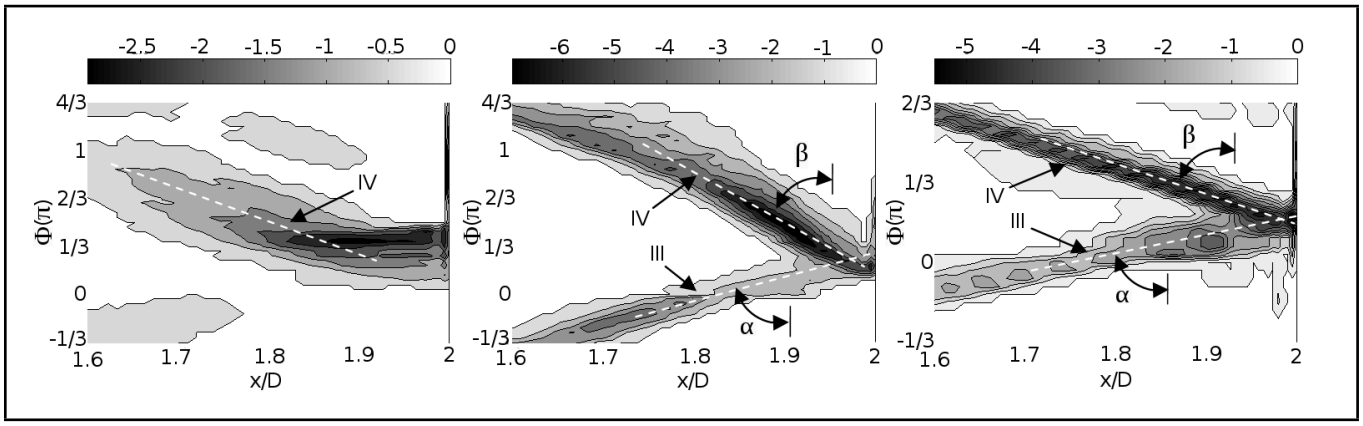

Figure 13. $x - t$ diagrams of compression wave propagating through Line A.

[10] Zhang, X. Compressible Cavity Flow Oscillation due to Shear-layer Instabilities and Pressure Feedback, *AIAA Journal*, **33**(8), 1404–1411, (1995).

[11] Tam, C. J., Orkwis, P. D., and Disimile, P. J. Supersonic Open Cavity Flow Physics Ascertained from Algebraic Turbulence Model Simulations, AIAA Paper 1996–0075.

[12] Schmit, R. F., Semmelmayer, F., Haverkamp, M., and Grove, J. E. Fourier Analysis of High Speed Shadowgraph Images around a Mach 1.5 Cavity Flow Field, AIAA 2011–3961.

[13] Krishnamurty, K. Acoustic Radiation from Two-dimensional Rectangular Cutouts in Aerodynamic Surfaces,Tech. Rep., NACA-TN-3487, 1955.

[14] Heller, H. H., Holmes, D. G., and Covert, E. E. Flow-Induced Pressure Oscillations in Shallow Cavities, *Journal of Sound and Vibration*, **18**(4), 545–553, (1971).

[15] Gloerfelt, X., Bogey, C., Baillyand, C., Juvé, D. Aerodynamic Noise Induced by Laminar and Turbulent Boundary Layers over Rectangular Cavities, AIAA 2002–247.

[16] Nonomura, T. and Fujii, K. Effects of Difference Scheme Type in High-order Weighted Compact Nonlinear Schemes, *Journal of Computational Physics*, **228**, 3533–3539, (2009).

[17] Nonomura, T., Iizuka, N., and Fujii, K. Freestream and Vortex Preservation Properties of High-order WENO and WCNS on Curvilinear Grids, *Computers and Fluids*, **39**, 197–214, (2010).

[18] Nonomura, T., Li, W., Goto, Y., and Fujii, K. Efficiency Im-

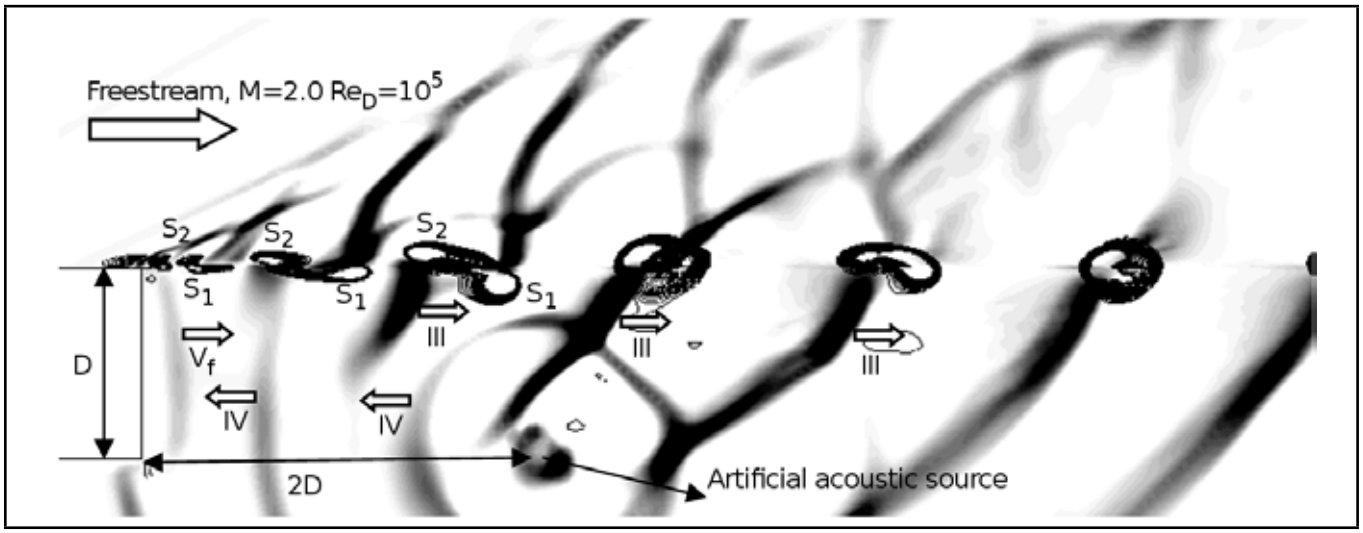

Figure A1. Free shear-layer subjected to an artificial acoustic source. Background contours represent the divergence of velocity ($-2 < div\mathbf{u} < -0.1$), and black contour lines represent the second-order invariant of velocity gradient tensors ($(a_\infty/D)^2 < Q_{2nd} < 15(a_\infty/D)^2$).

provements of Seventh-order Weighted Compact Nonlinear Scheme, *CFD Journal*, **18**(2), 193–198, (2010).

[19] Shima, E. and Jounouchi, T. Role of CFD in Aeronautical Engineering (No. 14) -AUSM type Upwind Schemes, *Proceedings of the 14th NAL Symposium on Aircraft Computational Aerodynamics*, National Aeroautical Laboratory, 7–12, (1997).

[20] Nishida, H. and Nonomura, T. ADI-SGS Scheme on Ideal Magnetohydrodynamics, *Journal of Computational Physics*, **228**, 3182–3188, (2009).

[21] Zhuang, N., Alvi, F. S., and Shih, S. Another Look at Supersonic Cavity Flows and Their Control, AIAA Paper 2005–2803.

[22] Forestier, N., Jacquin, L., and Geffroy, P. The Mixing Layer over a Deep Cavity at High-subsonic Speed, *Journal of Fluid Mechanics*, **475**, 101–145, (2003).

[23] Sandham, N. D. and Reynolds, W. C. Compressible Mixing Layer: Linear Theory and Direct Simulation, *AIAA Journal*, **18**(4), 618–624, (1990).

[24] Li, W., Nonomura, T., Oyamaand, A., and Fujii, K. Feedback Mechanism in Supersonic Laminar Cavity Flows, *AIAA Journal*, **51**(1), 253–257, (2013).

[25] Larchevêque, L., Sagaut, P., Maryand, I., Labbé, O. Large-eddy Simulation of a Compressible Flow Past a Deep Cavity, *Physic1 of Fluids*, **15**(1), 193–210, (2003).

[26] Lele, S. K. Direct Numerical Simulation of Compressible Free Shear Flows, AIAA1989-0374.

[27] Robinson, S. K. Coherent Motions in the Turbulent Boundary Layer, *Annual Review of Fluid Mechanics*, **23**, 601–639, (1991).

[28] Yokoyama, H. and Kato, C. Fluid-acoustic Interactions in Self-sustained Oscillations in Turbulent Cavity Flows. I. Fluid-dynamic Oscillations, *Physics of Fluids*, **21**, 105103, (2009).

APPENDIX

A two-dimensional simulation of laminar free shear layer subjected to an artificial acoustic source was conducted. The aft wall and bottom wall of the cavity were removed. The flow conditions were the same as the Ma2.0 case. The artificial acoustic source locateed at the same position of the cavity's right bottom corner. Its definition follows Eqs. (16)-(18) described in Lele's work.[26] The non-dimensional amplitude $A/_\infty$ are 3.0×10^{-5}, and the frequency f is the same as the dominant frequency for the cavity flow.

Figure A1 shows a scenario of phase-averaged flow-fields. The background contours represent the divergence of velocity, and black contour lines represent the second-order invariant of velocitygradient tensors. Wave IV represents the compression waves radiated from the artificial acoustic source; III represents the Mach waves; V_f represents the front-wall reflection waves. Similar to the cavity flow, two vortices S_1 and S_2 roll up from the leading edge periodically in the phase of each acoustic excitation caused by the compression waves radiated from the artificial acoustic source. The scales of vortices are amplified by Kelvin-Helmholtz instability. Vortex pairing occurs downstream.

The Mach waves radiated from the shear layer are just beneath the large-scale vortices. Assuming that a cavity aft wall is located downstream, when the large-scale vortical structures impinge on the cavity aft wall, it is surely followed by an action of the reflection of Mach waves. Since the radiation of Mach waves is essentially caused by the convection of large-scale vortices, it is desirable to state that the dominant reason for the generation of acoustic disturbances in supersonic laminar cavity flows is the successive passage of large-scale vortices over the trailing edge.

Meshless Numerical Solution of Boundary Integral Equations based on Non Uniform Rational Basis-Splines

Vincenzo Marchese and Umberto Iemma

Department of Engineering, Roma Tre University, via Vito Volterra, 62, Roma, Italy

(Received 15 August 2013; accepted 11 December 2014

The paper deals with the use of Non Uniform Rational Basis-Splines (NURBS) for the global representation of domain geometry and unknown functions aimed at the numerical solution of Boundary Integral Equations (BIE). The use of a global NURBS function basis yields a meshless method which does not need the partition of the boundary into elements. The level of the accuracy in the representation of dependent and independent variables can be changed in each simulation, according to the problem requirements, thanks to the recursive definition of NURBS. The solving system of equations is assembled by means of the collocation of the integral equation onto the Greville abscissae in the NURBS parametric space. The unknowns are the locations of the control points in the vector space the unknown function belongs to. Preliminary numerical results have been obtained in potential aerodynamics and acoustic scattering. The numerical solution reveals a remarkable level of accuracy in all the test cases analyzed with a convergence rate always higher than the order of the NURBS adopted.

1. INTRODUCTION

In many fields of application, the Boundary Integral Equations (BIE) approach is a well established technique to address the solution of Boundary Value Problems (BVP). Using the BIE, it is possible to represent the unknown function at any location in the domain as a function of its Cauchy data set. This approach is more recently considered as standard in incompressible and compressible potential aerodynamics, structural elasticity, heat conduction, electromagnetism, acoustics, and aeroacoustics. The numerical solution typically relies on the Boundary Element Method (BEM), in all its variants and declinations. In classic BEM the boundary of the domain is partitioned into finite elements, where the dependent and independent variables are approximated using suitable local basis functions. The greatest advantage of the numerical methods based on BIE resides in the reduction of the computational burden required for the numerical solution, due to the reduced dimensionality of the problem. Although this approach is usually convenient with respect to the so-called *field* methods, such as Finite Volumes Method (FV), Finite Difference Method (FDM), or Finite Element Method (FEM), in some specific application the number of boundary elements required to capture a specific feature of the phenomenon may become extremely high. This is the case, for example, for acoustic propagation and scattering problems, where the wave length of the perturbation at high frequencies can be orders of magnitude smaller than the characteristic length of the domain of interest, thus requiring a huge amount of boundary panels to correctly reproduce the scattering and interference effects. One of the possible approaches to mitigate this difficulty is improving the accuracy of the local representation of the variables using higher-order functions. This allows for the reduction of the number of elements needed to achieve the desired level of accuracy. In this respect, the literature available is very extensive, and an in-depth review is beyond the scope of the paper. Among others, it is worth mentioning the use of third order polynomials based on Overhauser[1,2] or Hermite[3,4] elements, recently coupled with Coons patches.[5] The typical limitation of all the approaches based on the local representation of the variables is the restriction of the resulting numerical formulation to a single order of accuracy, fixed by the order of the polynomial shape functions used. The possibility to overcome this limitation has already been investigated within the context of the finite element method[6] using an approach based on generalized Hermite polynomials. However, a similar attempt for the solution of BIE is still missing. This goal has been the driving motivation in the development of the method presented here. Indeed, using a global representation of the variables based on NURBS, the order of the basis functions can be improved when needed by the specific application in discussion. This is a consequence of the iterative definition of the NURBS, which makes possible the increase of the NURBS degree simply by changing an input parameter. The use of the NURBS for the representation of curves and surfaces is a common technique in the CAD community for the modeling of complex geometries with strict requirements of smoothness and continuity between patches.[7,8] Their use in the numerical solution of BIE is not new, although it is relatively recent. NURBS have been used to develop boundary element solutions of integral equations in elastostatics,[9] in radiation and diffraction problems,[10] and in potential aerodynamics.[11] As already mentioned, the peculiarity of the present method is in the use of the NURBS for the development of a global isogeometric approach aimed at the meshless numerical solution of the BVP. The control points used for the representation of the dependent variables are obtained through the *h*-refinement of the optimal NURBS

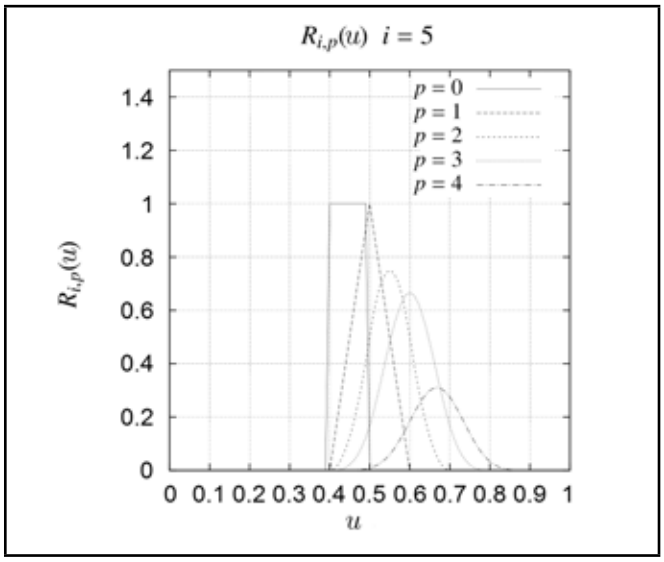

Figure 1. Function $R_{i,p}(u)$ for $u_i = 0.5$ and $0 \leq p \leq 5$.

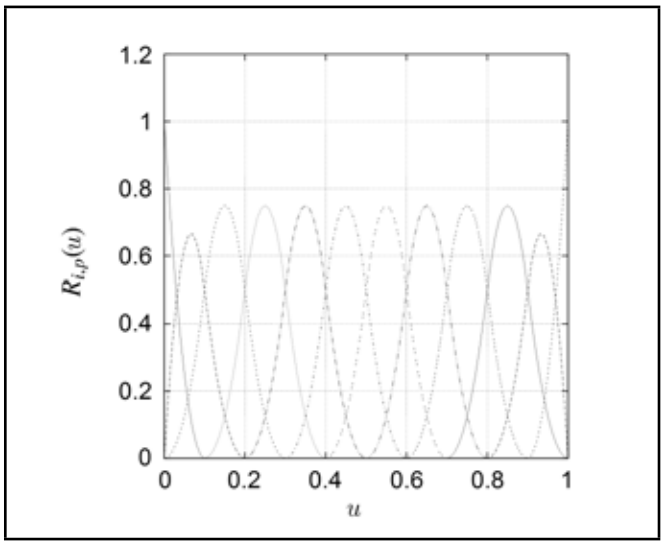

Figure 2. NURBS basis for $p = 2$.

representation of the geometry. The final system of equation is obtained by means of a collocation method based on the use of the Greville abscissae in the parametric space.

The paper is organized as follows: The global NURBS decomposition of a generic BIE formulation is presented in section 2, whereas the collocation method and the *h*-refinement technique are outlined in section 3. Section 4 reports the results of preliminary numerical simulations, and includes the analysis of the convergence of the solution as a function of the number of control points used. Appendix A is dedicated to some consideration about the integration strategy adopted to handle the singularity of the kernels.

2. NURBS REPRESENTATION OF BIE

Consider a physical phenomenon governed by the Laplacian of the function $\varphi(\boldsymbol{x})$, for $\boldsymbol{x} \in \Omega$. The BIE formulation of such a problem has the form

$$E(\boldsymbol{y})\,\varphi(\boldsymbol{y}) = \oint_\Gamma \left(G \frac{\partial \varphi}{\partial n} - \frac{\partial G}{\partial n}\,\varphi \right) \mathrm{d}\Gamma(\boldsymbol{x}); \qquad (1)$$

where $G(\boldsymbol{x}, \boldsymbol{y})$ is the fundamental solution of the governing partial differential equation, Γ is the boundary of the domain Ω, $\boldsymbol{x} \in \Gamma$, $\boldsymbol{y} \in \overline{\Omega} = \Omega \cup \Gamma$, and $\partial\varphi/\partial n = \nabla\varphi \cdot \boldsymbol{n}$, being $\boldsymbol{n}$ the unit normal to Γ pointing into Ω. The value of the domain function $E(\boldsymbol{y})$ is $1, 1/2, 0$ for $\boldsymbol{y} \in \Omega$, $\boldsymbol{y} \in \Gamma$ or $\boldsymbol{y} \notin \overline{\Omega}$, respectively (see appendix A). When the Cauchy data of the problem are known, Eq. 1 is an integral representation of $\varphi(\boldsymbol{y})$ for $\boldsymbol{y} \in \Omega$. On the other hand, when only part of the Cauchy set is known from the boundary conditions, Eq. (1) can be used as an integral equation for the unknown corresponding to the missing part of the boundary data. If, for example, the differential problem exhibits Neumann boundary conditions, then Eq. (1) can be written as

$$E(\boldsymbol{y})\,\varphi(\boldsymbol{y}) = \oint_\Gamma \mathcal{K}(\boldsymbol{y}, \boldsymbol{x})\;\varphi(\boldsymbol{x})\mathrm{d}\Gamma(\boldsymbol{x}) + b(\boldsymbol{y}); \qquad (2)$$

which is a Fredholm integral equation of the second kind in the unknown $\varphi(\boldsymbol{x})$, with kernel $\mathcal{K}(\boldsymbol{y}, \boldsymbol{x}) = -\nabla G(\boldsymbol{y}, \boldsymbol{x}) \cdot \boldsymbol{n}$, and where

$$b(\boldsymbol{y}) = \oint_\Gamma G(\boldsymbol{y}, \boldsymbol{x})\;\frac{\partial \varphi}{\partial n}\mathrm{d}\Gamma(\boldsymbol{x}) \qquad (3)$$

is known.[12,13] The BIE so obtained can be solved numerically through the BEM, by partitioning the boundary Γ into M elements and introducing a local representation of the dependent and independent variables using an appropriate function basis. In the present work, the numerical solution of Eq. (2) is obtained using a global, isogeometric NURBS decomposition. The general form of a NURBS curve is

$$f(u) = \frac{\sum_{i=1}^{N} N_{i,p}(u) W_i q_i}{\sum_{i=1}^{N} N_{i,p}(u) W_i}, \qquad u \in [0,1]; \qquad (4)$$

where the rational basis functions of order p, $N_{i,p}(u)$ are defined in a recursive way as

$$N_{i,p}(u) = \frac{u - u_i}{u_{i+p} - u_i} N_{i,p-1}(u) + \frac{u_{i+p+1} - u}{u_{i+p+1} - u_{i+1}} N_{i+1,p-1}(u); \qquad (5)$$

with

$$N_{i,0}(u) = \begin{cases} 1 & \text{if} \quad u_i \leq u < u_{i+1} \\ 0 & \text{otherwise} \end{cases} . \qquad (6)$$

The points q_i are called *control points* and the quantities W_i are the weights of the NURBS. The set of abscissae u_i needed to fully define the basis functions forms the *knot vector*. If the knot vector has $p + 1$ elements repeated at its beginning and at its end, it is called an *open* knot vector. In general, for a NURBS curve the following two properties hold:

1. if a knot u_i is repeated k times, the continuity of the curve at that point is C^{p-k}.
2. if the curve is C^0 at a point, the control point belongs to the curve.

As a consequence, for a given open knot vector the resulting NURBS passes through the first and last control points. Equation (4) can be written as

$$f(u) = \sum_{i=1}^{N} R_{i,p}(u) q_i, \qquad u \in [0,1]; \qquad (7)$$

with

$$R_{i,p}(u) = \frac{N_{i,p}(u)W_i}{\sum_{i=1}^{n} N_{i,p}(u)W_i}. \quad (8)$$

The function $R_{i,p}(u)$ for $u_i = 0.5$ and $0 \leq p \leq 5$ is depicted in Fig. 1, whereas Fig. 2 shows the complete basis in $u \in [0, 1]$, for $p = 2$.

On the basis of Eqs. (4) to (8) the NURBS representation of φ has the form

$$\varphi(u) = \sum_{i=1}^{N} R_{i,p}(u)q_i; \quad (9)$$

with coefficients q_i and basis functions as reported in Eq. (8). Applying Eq. (9) to the RHS of Eq. (2), and limiting, for the sake of simplicity, the notation to the two-dimensional case, we obtain

$$E(\boldsymbol{y})\varphi(\boldsymbol{y}) = b(\boldsymbol{y}) - \sum_{i=1}^{N} q_i \oint_{\Gamma} \frac{\partial G(u, \boldsymbol{y})}{\partial n} R_{i,p}(u)J(u)du; \quad (10)$$

where $J(u)$ is the Jacobian of the transformation from the physical space coordinate $\boldsymbol{x}$ to the NURBS parametric space one u. It is worth noting that the integrals in Eq. (10) span the whole boundary. Indeed, the use of the global NURBS representation makes the concept of surface elements no longer required for the numerical solution of Eq. (10) and thus the partition of Γ is not strictly needed. On the other hand, the integrals in Eq. (10) must be accurately evaluated and, unless we have an analytical solution for them (and this could happen for very simple geometries and/or boundary conditions), a suitable numerical integration strategy must be identified. To this aim, a possible solution for complex geometries and/or boundary conditions could be the partition of the boundary into macro patches on which suitable quadrature formulas can be easily applied. However, it is important to notice that this partitioning, if needed, would have nothing to do with the number of unknowns of the solving linear system, but only with the proper evaluation of the integrals in Eq. (10). In appendix A the effects of the partition of Γ on the convergence of the integrals in Eq. (10) is analyzed for two different geometries.

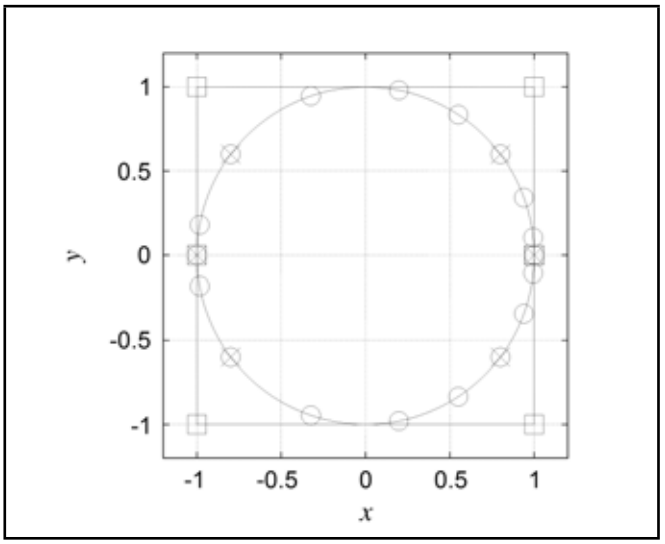

Figure 3. NURBS Circle, (□) control points, (×) Greville's abscissae in the physical space, (○) refined Greville's abscissae in the physical space.

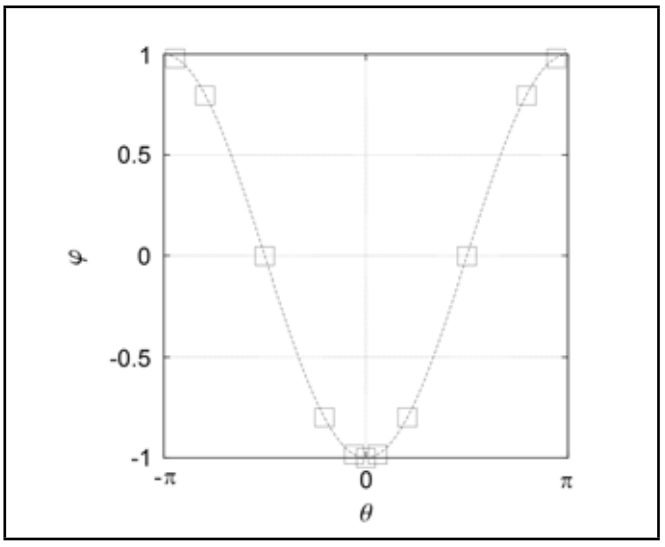

Figure 4. Velocity potential φ for a uniform flow U_∞ in x-direction. $(-)$ Analytical solution, (□) BIE-NURBS, $p = 3$.

3. THE NUMERICAL SOLUTION

The numerical solution of Eq. (10) can be obtained using the collocation method, with collocation points lying on the boundary Γ. To this aim, it is necessary to identify a set of collocation points $\boldsymbol{y}_k \in \Gamma$. In the present approach, this requires the identification of a set of abscissae u_k in the NURBS parametric space corresponding to points on Γ in the physical space through the relationship

$$\boldsymbol{y}(u_k) = \sum_{i=1}^{N} R_{i,p}(u_k)\boldsymbol{\eta}_i; \quad (11)$$

where n is the number of the control points $\boldsymbol{\eta}_i$ used to build the NURBS reproducing the geometry of Γ. To ensure that $\boldsymbol{y}(u_k)$ is located on the boundary, the abscissa u_k must be chosen according to the Greville distribution[9,14]

$$u_k^{'} = \frac{u_{i+1} + u_{i+2} + \ldots + u_{i+p}}{p}, \quad i = 1, \ldots, n-1. \quad (12)$$

The abscissae $u_k^{'}$ satisfying Eq. (12) correspond to points in the physical space such that $\boldsymbol{y}(u^{'}) \in \Gamma$ (see Fig. 3). A key aspect in the numerical evaluation of the integrals in Eq. (10) is the management of the singularities of the kernels arising from the collocation of the observation point $\boldsymbol{y}$ on the boundary. In this respect, the meshless approach presents a significant advantage with respect to the classic BEM, as the integration is now extended to the whole boundary or, for complex geometries, to a part of it significantly larger than a single boundary element. As a consequence, the verification for singularity occurrence, which is not a straightforward task with NURBS, is less critical, or even not required at all, thus simplifying the numerical integration procedure. The asymptotic behavior of the integral appearing in Eq. (2) is briefly explained in appendix A for the sake of clarity and completeness of the paper. Once that the location of the collocation points is fixed using the Greville abscissae we can apply the same decomposition given in Eq. (9)

to the left hand side of Eq. (10). For $\boldsymbol{y} \in \Gamma$ we obtain

$$\frac{1}{2}\mathsf{R}\,\mathsf{q} = \mathsf{b} - \mathsf{C}\,\mathsf{q}; \tag{13}$$

where the elements of b and C have the form

$$b_j = \oint_\Gamma G(\boldsymbol{x}, \boldsymbol{y}_j)\frac{\partial \varphi}{\partial n} d\Gamma,\ C_{ij} = \oint_\Gamma \frac{\partial G(u, \boldsymbol{y}_j)}{\partial n} R_{i,p}(u) J(u) du; \tag{14}$$

where $u \in [0, 1]$. The entries of the $N \times N$ matrix R have the form $\mathsf{R}_{ij} = R_{i,p}(u_j^{'})$. The final form of the linear system is $(0.5\,\mathsf{R} + \mathsf{C})\ \mathsf{q} = \mathsf{b}$, which can be solved using the most appropriate solver.

3.1. Knots *h*-refinement

In the derivation performed so far we assumed, without loss of generality, unit weights in Eq. (8). This choice is certainly not optimal for the representation of complex functions, but is the only one possible to easily represent the unknowns. Indeed, for a generic function φ could be possible, in principle, to identify an optimal set of weights and control points capable to achieve a high level of accuracy with a limited number of degrees of freedom. In real applications, this can easily be done to represent regular geometries (for example, simple geometries of the boundary Γ). On the contrary, in complex phenomena, the optimal representation of the unknown φ could be not a simple task. As an example, consider a domain bounded a circle. It can be represented exactly with the six control points depicted by squares in Fig. 3, provided that the vectors of the corresponding weights and nodes are $\mathsf{W}_c^T = \{1\ 0.5\ 0.5\ 1\ 0.5\ 0.5\ 1\}$ and $\mathsf{u}_c^T = \{0\ 0\ 0\ 0.25\ 0.5\ 0.5\ 0.75\ 1\ 1\ 1\}$, respectively (see, *e.g.*, Piegl[8]). On the other hand, the physical phenomenon described by the function φ can be extremely complex, even if the boundary of the domain is so simple. If, for example, we are dealing with the scattering of an acoustic wave impinging on the circle at medium-high frequencies, W_c and u_c are clearly not suitable to accurately reproduce the scattering pattern. In order to increase the number of collocation points for the numerical solution of the BIE, the *h*-refinement technique is used, starting from the NURBS optimal representation of Γ. With the *h*-refinement technique, the non-zero intervals between the components of the knot vector u_c are refined with equally spaced knots. The number of inserted knots does not need to be the same for each interval, and thus the NURBS representation can be enriched only where needed. These new knots become the control points of the representation of the unknown φ. The refinement obtained using an uneven distribution of knots in the different intervals is depicted in Fig. 3 ($\circ$), along with the original knot vector ($\times$).

4. RESULTS AND DISCUSSION

The method presented in the paper was first applied to simple problems, for which analytical solutions are available, in order to validate the accuracy of the numerical results and assess its convergence for an increasing NURBS order, p. The problems chosen for this assessment were the incompressible, two-dimensional potential flow around an impermeable circular cylinder, and the scattering of a planar wave impinging on a sound-hard cylindrical obstacle.

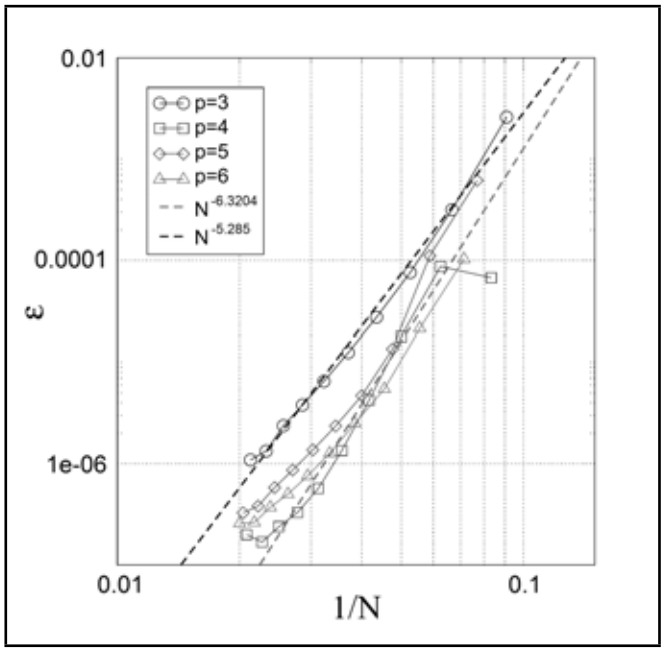

Figure 5. Convergence of ϵ for the solution of potential incompressible aerodynamics.

After this analysis, the method was tested on a boundary geometry of class $\mathcal{C}^0$, to demonstrate the capability of the method in the modelling of slope discontinuities of the boundary profile. Indeed, such a situation, which is very common in practical applications, could become critical for a global representation based on (at least) $\mathcal{C}^1$ continuous functions, so a careful treatment of the corner points is needed. Here, the two-dimensional scattering of a plane wave by a cylinder with a squared cross section is compared with an accurate numerical solution obtained with a widely assessed, highly accurate, commercial FEM code.

4.1. Assessment Against Analytical Solutions

As already mentioned, this section includes an analysis of the convergence of the numerical error with the order p of the NURBS. This particular aspect deserves some preliminary clarification to put the obtained results in the proper perspective.

The method presented in this paper exhibits a $p-$type convergence to the asymptotic solution by increasing the order p of the spline resulting from Eq. (9). On the other hand, the improvement of the solution for a given value of p is obtained by refining the control points distribution (see section 3.1). On the other hand, the convergence obtained by increasing the number N of control points cannot be exactly interpreted as an h-type convergence, because there is no mesh, and thus talking about mesh size h would not apply. Nevertheless, the knots refinement improves the representation for a fixed order p. For these reasons, in the following the convergence diagrams are plotted as a function of the number of knots (*i.e.*, the number of unknowns) N using p as a parameter, similarly to what is done

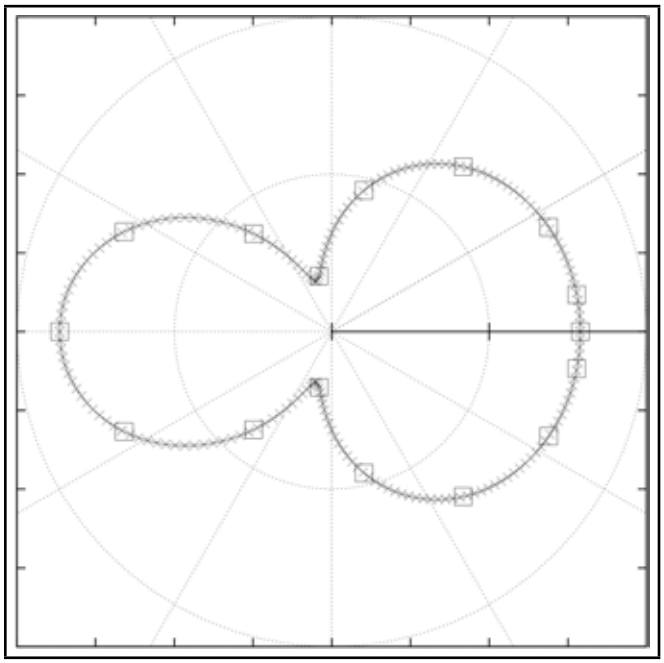

Figure 6. Scattering field on the cylinder, $f = 50Hz$. $(-)$ Analytical, $(\times)$ BIE-NURBS, $(\square)$ BIE-NURBS at Greville's abscissae.

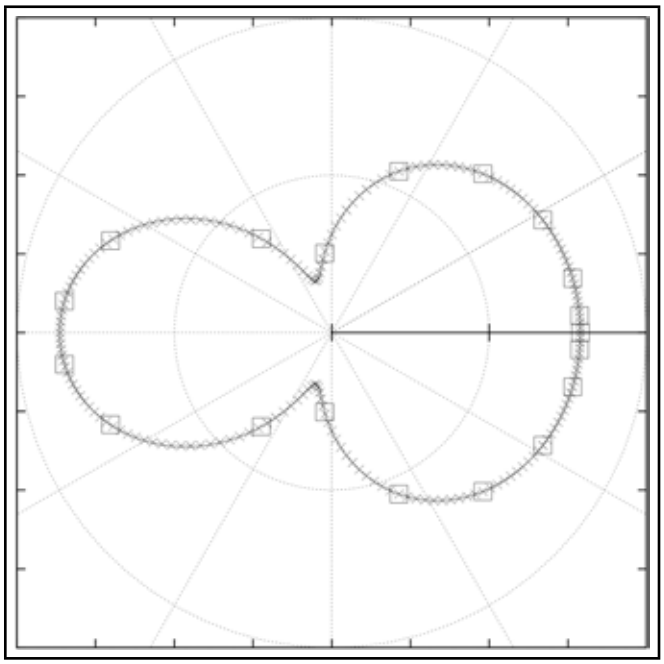

Figure 7. Effect of refinement at $f = 50Hz$. Scattering field, $(-)$ analytical, $(\times)$ BIE-NURBS, $(\square)$ BIE-NURBS at Greville's abscissae, $N = 20$, $p = 3$.

with h-type convergences. It is important to notice that the structure of the algorithm is such that for each value of p, the minimum number of unknowns is fixed (see Eq. (9)), and thus each convergence curve starts from a different N. To clarify, the convergence diagrams depict only the minimum and maximum convergence rates measured for the problem analysed, whereas the complete report of the rates observed is presented in Tables 1 and 2, including the minimum error.

For the sake of completeness, in appendix A the convergence of the numerical integration of the boundary integral in Eq. (10) is discussed for the case of a complex geometry. Indeed, the integrals resulting from the present global approach are defined over the entire boundary and for complex geometries the accuracy of their numerical evaluation can be improved by partitioning the domain into *macro-elements*. It must be stressed that this partition has nothing to do with the asymptotic behavior of the method, and is only intended for the accurate calculation of the matrix coefficients.

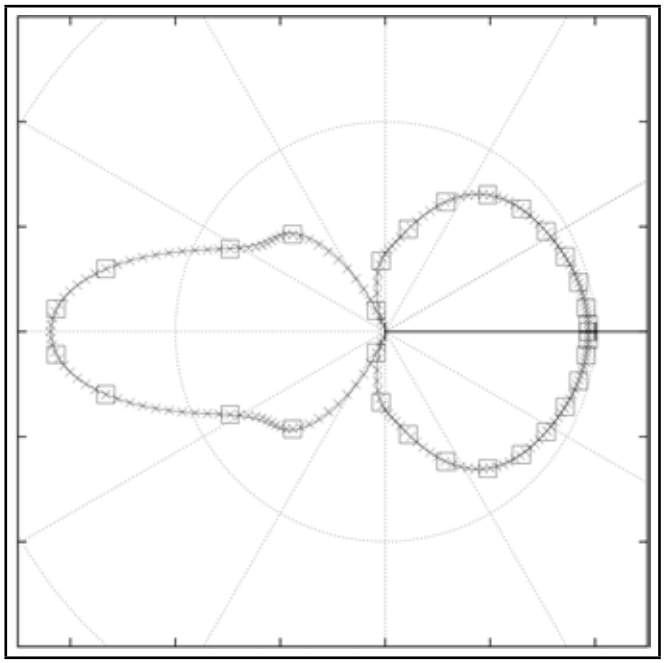

Figure 8. Scattering field at $f = 200Hz$, $(-)$ analytical, $(\times)$ BIE-NURBS, $(\square)$ BIE-NURBS at Greville's abscissae, $N = 32$, $p = 3$.

4.1.1. Incompressible Potential Flow Around a Unit Circle

In the first application, the function φ has the physical meaning of the velocity potential associated to the irrotational flow of an inviscid fluid. In such a flow $\boldsymbol{v} = \nabla\varphi$, and the phenomenon is governed by the Laplace equation for φ. Here, we consider an impermeable circular cylinder immersed within a main flow at speed $\boldsymbol{v}_0$. The velocity field is given by the superposition of the main stream velocity and the perturbation $\boldsymbol{v}'$ induced by the obstacle. The fundamental solution of the problem and its normal derivative on Γ are

$$G(\boldsymbol{x},\boldsymbol{y}) = -\frac{1}{2\pi}\,\ln r, \quad \frac{\partial G}{\partial n} = -\frac{1}{2\pi}\,\frac{\boldsymbol{r}\cdot\boldsymbol{n}}{r^2}; \tag{15}$$

where $r = \|\boldsymbol{x} - \boldsymbol{y}\|$. The analytical solution φ_a exists and has the form (in polar coordinates) $\varphi_a = v_0 r\left(1 + R^2/r^2\right) cos(\theta)$. Fig. 4 shows the comparison of the numerical solution of the present method, φ, with the analytical solution φ_a. The convergence of the global error ϵ, defined as

$$\epsilon = \sqrt{\int_\Gamma \left\| \frac{\varphi - \varphi_a}{\varphi_a} \right\|^2 d\Gamma}, \tag{16}$$

is presented in Fig. 5 as a function of $1/N$ for different values of the the degree of the NURBS representation. Table 1 reports the values of the convergence rates measured using a linear regression of the error in the log-log plane, and the minimum error observed. What can be observed first, is that the

Table 1. Convergence rates for the solution of the Laplace equation.

p	Convergence rate	Error at N max
3	5.2850	1.88240447163443e-06
4	6.3204	1.98627799279891e-07
5	5.6809	5.88921480592586e-07
6	4.9574	3.86320539590748e-07

Table 2. Convergence rates for the scattering of a plane wave by a cylindrical obstacle.

p	Convergence rate		Error at N max	
	$f =$ 50 Hz	$f =$ 200 Hz	$f = 50$ Hz	$f = 200$ Hz
2	4.0698	3.5075	0.000765660508167538	0.0444788053349804
3	5.2460	5.1965	0.000182807195261099	0.0149446263946068
4	7.4613	5.8926	2.02511544866008e-05	0.0051694130089412
5	8.4307	8.5100	1.02520999392619e-05	0.0016074909579270
6	9.2709	10.336	5.56624126228440e-06	0.0008186444737082

convergence curves are non linear in the log/log plane, and, consistently with the use of a rational function basis, the rate of convergence cannot be inferred directly from the order p of the NURBS. The rate of convergence is slightly higher for lower N, gradually diminishes in finer simulations, and appears to be marginally dependent on the order p of the NURBS. Indeed, the average rate is between N^{-4} and N^{-5} for $3 \leq p \leq 6$. Moreover, the best results are surprisingly obtained for $p = 4$. This phenomenon is not present in the acoustic simulations (see next section), and is currently under investigation. A possible reason could be related to the adoption of a uniform sampling in the NURBS parameter space which may produce unwanted oscillations of the higher-order functions.[8]

4.1.2. Scattering of a Planar Wave by a Circular Cylinder

In this case, the function φ represents a physical quantity satisfying the wave equation in Ω. The equation governing the propagation of an acoustic perturbation of angular frequency ω at speed c_0 is the Helmholtz equation, $\nabla^2\varphi + \kappa^2\,\varphi = 0$, where $\kappa = \omega/c_0^2$. Adopting the $e^{\mathrm{i}\omega t}$ time convention, the fundamental solution and its normal derivative on Γ are

$$G(\boldsymbol{x}, \boldsymbol{y}, \kappa) = \frac{\mathrm{i}}{4}\,\mathcal{H}_0^{(2)}(\kappa\, r), \quad \frac{\partial G}{\partial n} = -\frac{\mathrm{i}\,\kappa}{4}\,\mathcal{H}_1^{(2)}(\kappa r)\frac{\boldsymbol{r}\cdot\boldsymbol{n}}{r}; \tag{17}$$

where $r = \|\boldsymbol{x} - \boldsymbol{y}\|$ and $\mathcal{H}_m^{(2)}(\kappa\, r)$ is the second-kind Hankel function of order m. The case study at hand consists of a plane wave of unit amplitude impinging on a circular cylinder of infinite length, for which the analytical solution is known (for example, see Morse and Ingard[15]). Indicating $\boldsymbol{\kappa}$ as the wave vector, the incident field is given by $\varphi_i = e^{i\,\boldsymbol{\kappa}\cdot\boldsymbol{r}}$. Figure 6 shows the solution at $f = 50$ Hz. The values of $|\varphi|$ at the solution points are indicated with squares, whereas the NURBS reconstruction of the solution along the whole boundary is depicted with the times sign. The agreement with the analytical solution is remarkable. The effect of the *h*-refinement can be observed in Fig. 7, where four knots have been inserted in the first and last intervals and two knots in the second and third ones. The refined solution is substantially indistinguishable from the analytical one. This excellent behavior is preserved also at higher frequencies, as Figs. 8, 9, and 10 show for $f = 200$ Hz, $f = 500$ Hz, and $f = 1000$ Hz, respectively.

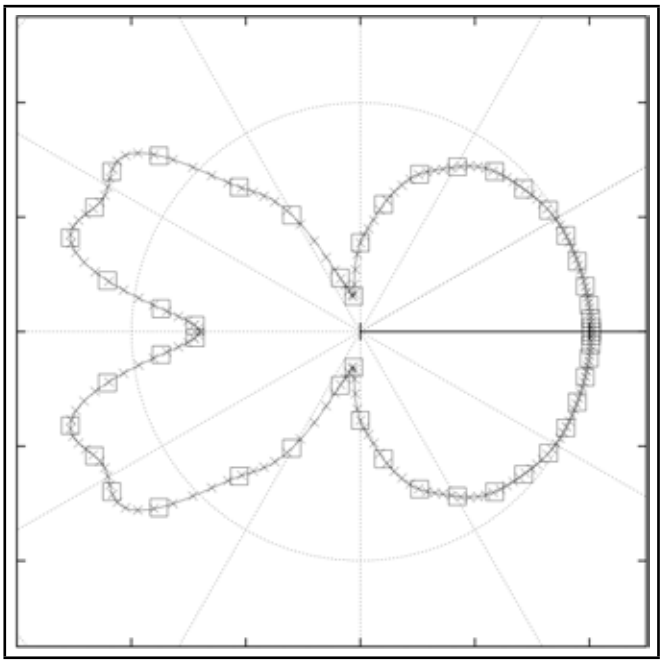

Figure 9. Scattering field at $f = 500Hz$, $(-)$ analytical, $(\times)$ BIE-NURBS, $(\square)$ BIE-NURBS at Greville's abscissae, $N = 50$, $p = 5$.

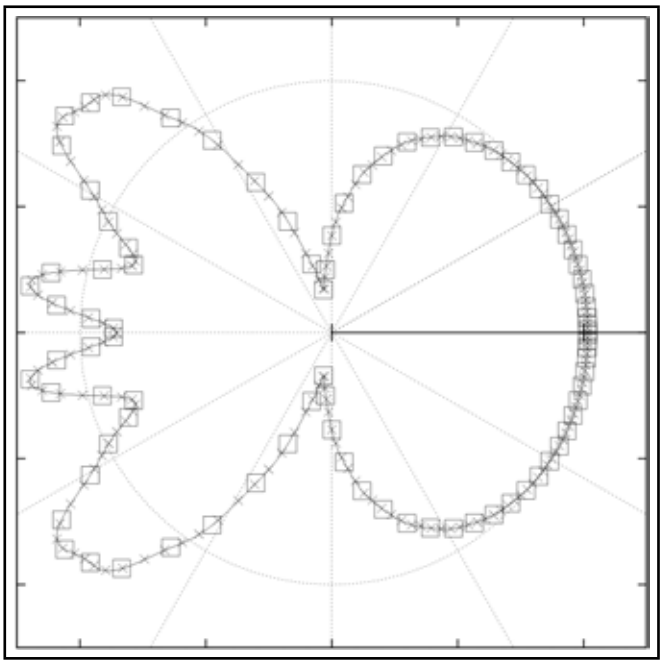

Figure 10. Scattering field at $f = 1kHz$, $(-)$ analytical, $(\times)$ BIE-NURBS, $(\square)$ BIE-NURBS at Greville's abscissae, $N = 90$, $p = 5$.

Also in this case, the convergence of the proposed formulation is evaluated using the global error ϵ defined in Eq. (16). The convergence analysis is performed using the *h*-refinement by inserting equally spaced knots. The convergence of ϵ as a function of $1/N$ is presented in Figs. 11 and 12 for $p = 2, 3, 4, 5, 6$ at $f = 50$ Hz and $f = 200$ Hz, respectively, whereas the convergence rates measured and the errors are reported in Table 2. As in the aerodynamic application, the log-log plots show a non-linear behavior. The major difference in the present application is in the progressive enhancement of the accuracy and rate of convergence as p increases.

It can be observed that the rate of convergence is greater than

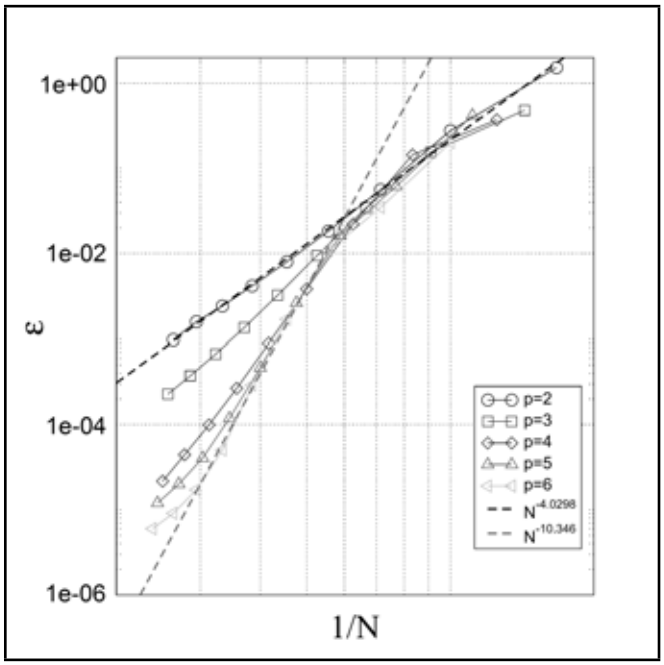

Figure 11. Convergence of ϵ at $f = 50Hz$.

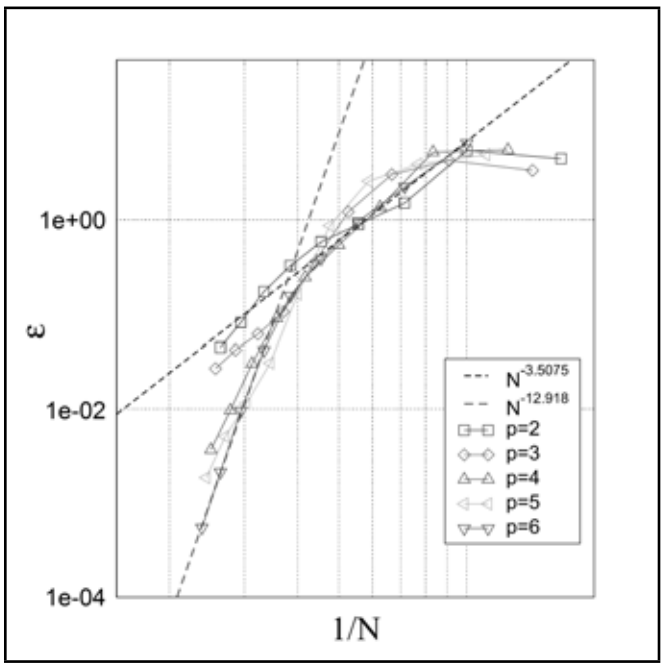

Figure 12. Convergence of ϵ at $f = 200Hz$.

p for all the degrees tested, reaching values close to $\mathcal{O}(N^{-13})$ for $p = 6$ at the higher frequency, confirming the remarkable level of accuracy achievable with the *h*-refinement.

4.2. 2D Scattering of a Sound-Hard Quadrilateral Obstacle

After the assessment of the method by comparison with analytical results, it is worth testing its performance with a test case presenting features that can be critical for the global NURBS iso-geometric representation. It is the case of a geometry profile with corners, where the curvature becomes infinite, and where the NURBS could give meaningless results if not treated appropriately. The analyzed geometry is that of a cylinder with a square cross section, with side edge dimension $l = 2$. Figures 13 and 14 show the geometry of the cross section, as well as a close-up of one of the corner. In order to avoid the curvature singularity, there are two possible strategies. The first one is to divide the boundary profile into four macro-elements corresponding to the four edges of the square. This possibility falls in the same case analyzed in appendix A and is not repeated here. The second one relies on the elimination of the curvature singularity at the corner points by imposing a small, finite curvature radius r_c (see Fig. 13). The global NURBS representation is directly applied to the approximated geometry so obtained, setting $r_c/l = 0.025$.

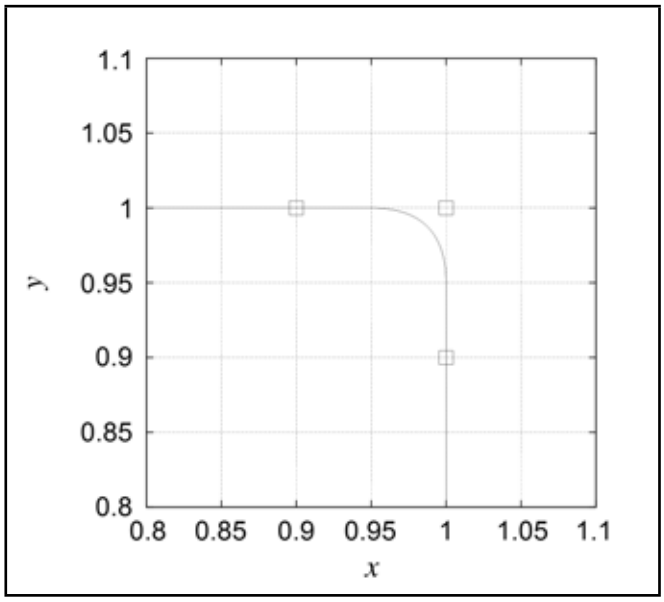

Figure 13. NURBS representation of the quadrilateral geometry. Markers indicate the control points used. The side dimension is $l = 2$, whereas the curvature radius r_c of the approximated corner is such that $r_c/l = 0.025$.

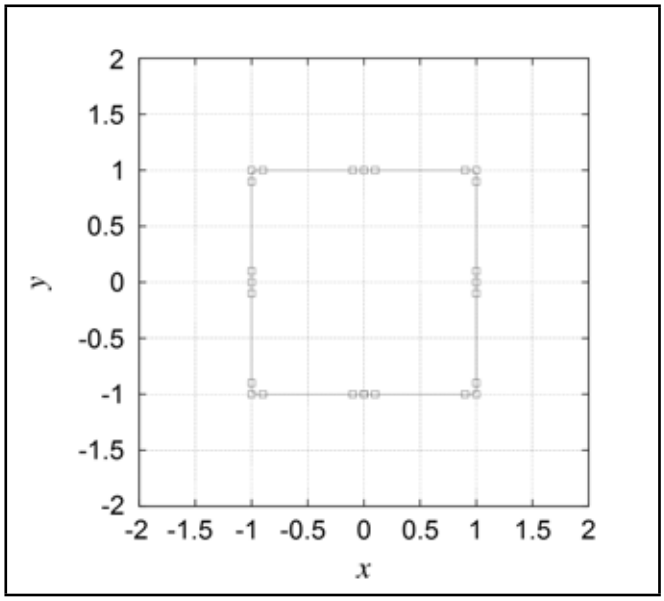

Figure 14. NURBS representation of the quadrilateral geometry. Close–up of the top right corner.

The solution of the present approach has been compared with the numerical solution obtained with the widely assessed commercial FEM software COMSOL.[16] The maximum ratio

between the mesh element size and the wavelength has been set to 0.05, in order to guarantee a converged reference solution with at least 20 elements per wavelength. The simulations of the present method are compared to the reference FEM solution in Figs. 15, 16 and 17. The first one depicts the absolute value of the scattered pressure on a circle of virtual microphones of radius $r_m = 20l$, whereas the second shows the total pressure along the upwind portion of the $x-$axis. In both cases, the frequency is 50 Hz. The solution obtained with the proposed approach is in remarkable agreement with the FEM solution, revealing that the approximation of the corner points with a finite curvature profile does not significantly affect the numerical solution. It is important to stress that the integral coefficients were obtained here by numerical integration along the entire boundary, confirming that the global representation yields accurate results also for geometries with potentially critical features.

Figure 17 presents a direct qualitative comparison of the two fields obtained with the NURBS (left) and FEM (right) simulations. The absolute value of the total pressure obtained with the two methods is in remarkable agreement on all the domain portion analyzed.

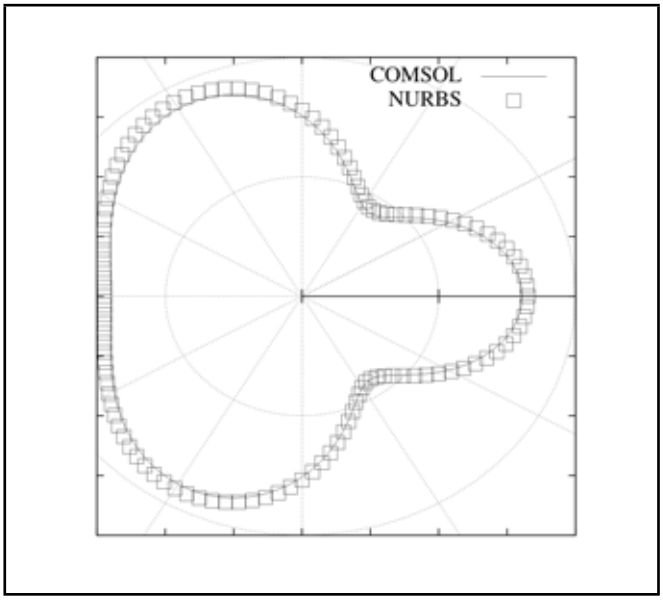

Figure 15. Scattered pressure evaluated at a circle of microphones with $r_m/l = 20$ (left) for $f = 50$ Hz. The continuous line indicates the FEM solution obtained with the COMSOL software.

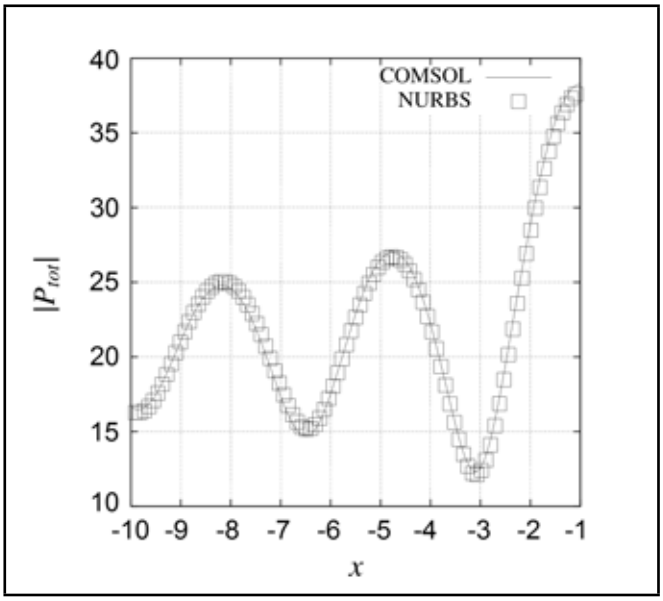

Figure 16. Total pressure evaluated along the upwind portion of the $x-$axis, for $f = 50$ Hz. The continuous line indicates the FEM solution obtained with the COMSOL software.

5. CONCLUDING REMARKS

A methodology for the numerical solution of BIE based on a global NURBS representation of dependent and independent variables has been presented. The non-local NURBS decomposition yields a meshless solution algorithm, which can be solved using a collocation method on the Greville abscissae in the NURBS parametric space. The unknowns of the resulting system of equations are the locations of the control points in the vector space the unknown function belongs to. The main advantage of the proposed methodology is the possibility to choose the order of the approximation at runtime, exploiting the recursive definition of the NURBS function basis. The method has been applied to problems of potential aerodynamics and acoustics for which analytical solutions are available. The preliminary results obtained reveal a remarkable agreement with the exact solutions. A very high convergence rate is achieved, reaching $\mathcal{O}(N^{-13})$ using sixth-order NURBS in the acoustic application. The reliability of the meshless isogeometric approach has been verified for geometries presenting critical features, such as corners and curvature changes. In all the test cases addressed, the global NURBS representation has revealed a very high accuracy and a substantial insensitivity to the extent of the numerical integration domain. The method is currently being extended to the analysis of three-dimensional problems, focusing on the treatment of the spurious eigenfrequencies affecting the numerical solution of exterior acoustics based on integral equations. Indeed, the peculiarities of the present approach observed and validated in the two-dimensional case suggest that the implementation of the classical regularization techniques, such as the CONDOR (Burton and Miller,[17]) or the CHIEF (Schenck,[18]), must be substantially revised to take advantage of the global NURBS representation. Specifically, a robust strategy to treat the hypersingular kernels arising in the Burton and Miller regularization is currently under analysis and will be the object of a future paper.

REFERENCES

[1] Johnston, P. R. Second order Overhauser elements for boundary element analysis, *Mathematical and Computer Modelling*, **23** (5), 61–74, (1996).

[2] Camp, C. V. and Gipson, G. S. Overhauser elements in boundary element analysis, *Mathematical and Computer Modelling*, **15** (3), 59–69, (1991).

[3] Gennaretti, M., Giordani, A., and Morino, L. A third-order boundary element method for exterior acoustics with appli-

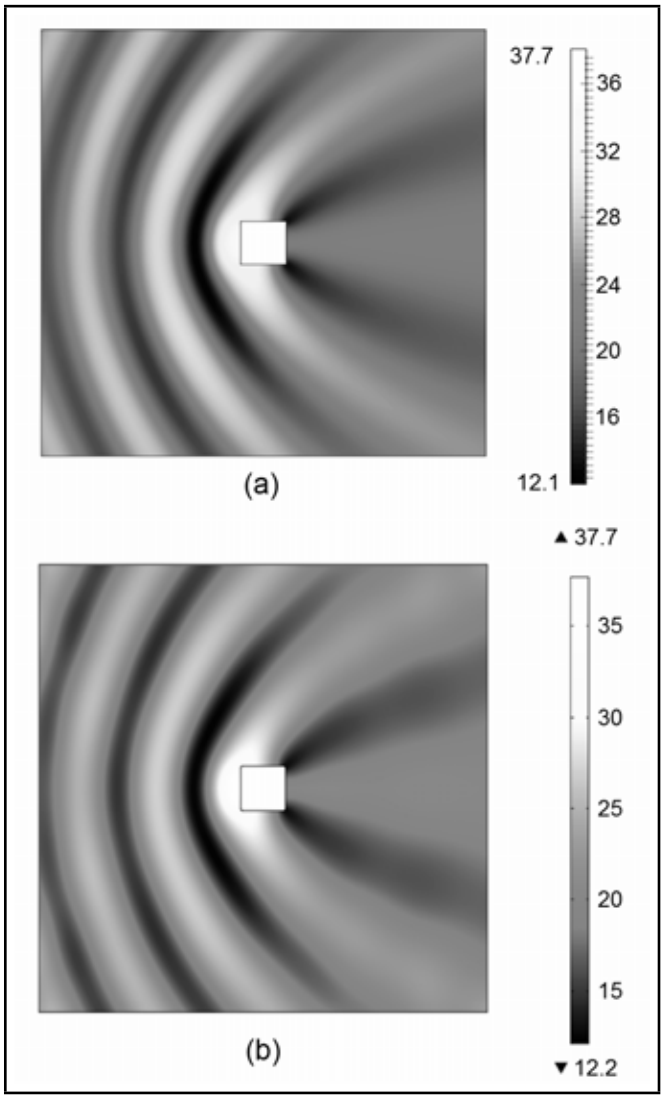

Figure 17. Absolute value of the total pressure field around the squared obstacle. The solution of the present method (a) is compared to the COMSOL FEM solution (b).

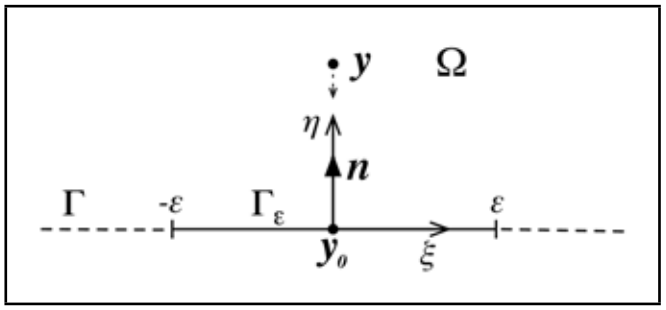

Figure 18. Observation point $\boldsymbol{y}$ approaching the boundary at $\boldsymbol{y}_0$.

cations to scattering by rigid and elastic shells, *Journal of Sound and Vibration*, **222** (5), 699–722, (1999).

[4] Iemma, U., Marchese, V., and Morino, L. High-order BEM for potential transonic flows, *Computational Mechanics*, **21** (3), 243–252, (1998).

[5] Iemma, U. and Burghignoli, L. A Hermite-Coons boundary element method, *Proc. 16th International Congress on Sound and Vibration, ICSV16*, Krakow, Poland, (2009).

[6] Morino, L., Iemma, U., and Cetta, F. Combining Hermite, Coons and Guyan: a highly efficient high-frequency finite element, In *Proc. 15th AIAA/CEAS Aeroacoustic Conference*, Miami, FL, USA, (2009).

[7] Rogers, D. F. *An Introduction to Nurbs: With Historical Perspective*, Morgan Kaufmann Series in Computer Graphics, Morgan Kaufmann Publishers, (2001).

[8] Piegl, L. On NURBS: a survey, *IEEE Computer Graphics and Applications*, **11** (1), 55–71, (1991).

[9] Simpson, R. N., Bordas, S. P. A., Trevelyan, J., and Rabczuk, T. A two-dimensional isogeometric boundary element method for elastostatic analysis, *Computer Methods in Applied Mechanics and Engineering*, **209-212**, 87–100, (2012).

[10] Kim, B. and Shin, Y. S. A NURBS panel method for three-dimensional radiation and diffraction problems, *Journal of Ship Research*, **47** (2), 177–186, (2003).

[11] Politis, C., Ginnis, A. I., Kaklis, P. D., Belibassakis, K., and Feurer, C. An isogeometric BEM for exterior potential-flow problems in the plane. *Proc. 2009 SIAM/ACM Joint Conference on Geometric and Physical Modeling*, 349–354, (2009).

[12] Hochstadt, H. *Integral Equations*, Wiley Classics Library, Wiley, (2011).

[13] Tricomi, F. G. *Integrals Equations*, Dover Books on Mathematics Series, Dover Publications, Incorporated, (1957).

[14] Johnson, R. W. Higher order b-spline collocation at the Greville abscissae, *Applied Numerical Mathematics*, **52** (1), 63–75, (2005).

[15] Morse, P. C. M. and Ingard, K. U. *Theoretical Acoustics*, International series in pure and applied physics, Princeton University Press, (1968).

[16] COMSOL Multiphysics, 1997-2008 COMSOL AB.

[17] Burton, A. J. and Miller, G. F. The application of integral equation methods to the numerical solution of some exterior boundary-value problems, *Proceedings of The Royal Society A*, **323**, 201–210, (1971).

[18] Schenck, H. A. Improved integral formulation for acoustic radiation problems, *Journal of the Acoustical Society of America*, **44** (1), 41–89, (1967)

[19] Kreyszig, E. *Advanced Engineering Mathematics*, John Wiley & Sons, (2010).

[20] Galassi, M., Davies, J., Theiler, J., Gough, B., Jungman, G., Alken, P., Booth, M., and Rossi, F. GNU Scientific Library—Reference Manual, Version 1.15. 2011. http://www.gnu.org/software/gsl/, (Accessed August 13, 2013).

Table 3. Real part of the double-layer integrals ($\times 10^3$) as a function of number of Gaussian abscissae N_G and number of partition of the boundary N_Γ.

circle			
	N_G=15	N_G=30	N_G=60
N_Γ=1	5.13868867036	5.13868866829	5.13868867004
N_Γ=2	5.13868867036	5.13868866829	5.13868867004
N_Γ=4	5.13868867036	5.13868866829	5.13868867004
flower-like			
N_Γ=1	8.567698577476	8.567693658759	8.567712281749
N_Γ=2	8.567698577476	8.567693658759	8.567712281749
N_Γ=4	8.567698577476	8.567693658759	8.567712281749

APPENDIX A: KERNEL SINGULARITIES AND NUMERICAL INTEGRATION

The aim of the present section is to analyze the asymptotic behavior of the kernel $\mathcal{K}$ of Eq. (2) for $\boldsymbol{y} \to \boldsymbol{y}_0 \in \Gamma$ and its relationship with the strategy used for the numerical integration. The analysis deals with the two specific applications covered. Assume that the observation point $\boldsymbol{y}$ approaches Γ from Ω (*i.e.*, from the positive side of the boundary) pointing to the boundary point $\boldsymbol{y}_o$ (see Fig. 18). The integral on the right hand side of Eq. (2) can be decomposed into two contributions: the integral over a straight segment Γ_ε centered in $\boldsymbol{y}_o$ of length 2ε, plus the integral over the remaining part of Γ

$$\mathcal{I}(\boldsymbol{y}) = \int_{\Gamma_\varepsilon} \varphi(\boldsymbol{x}) \frac{\partial G(\boldsymbol{y},\boldsymbol{x})}{\partial n}\, \mathrm{d}\Gamma + \int_{\Gamma\setminus\Gamma_\varepsilon} \varphi(\boldsymbol{x}) \frac{\partial G(\boldsymbol{y},\boldsymbol{x})}{\partial n}\, \mathrm{d}\Gamma. \tag{A.1}$$

Assuming ε sufficiently small, $\mathcal{I}$ can be approximated as

$$\mathcal{I}(\boldsymbol{y}) \simeq \varphi(\boldsymbol{y}_o)\, \mathcal{I}^\varepsilon + \int_{\Gamma\setminus\Gamma_\varepsilon} \varphi(\boldsymbol{x}) \frac{\partial G(\boldsymbol{y},\boldsymbol{x})}{\partial n}\, \mathrm{d}\Gamma. \tag{A.2}$$

The kernels associated to the aerodynamic and the acoustic problems are

$$\begin{aligned} \mathcal{K}_{\mathsf{ae}}(\boldsymbol{x},\boldsymbol{y}) &= -\frac{1}{2\pi}\, \frac{\boldsymbol{r}\cdot\boldsymbol{n}}{r^2}, \\ \mathcal{K}_{\mathsf{ac}}(\boldsymbol{x},\boldsymbol{y}) &= -\frac{1}{4}\, \mathrm{i}\,\kappa\, \mathcal{H}_1^{(2)}(\kappa R)\, \frac{\boldsymbol{r}\cdot\boldsymbol{n}}{r}. \end{aligned} \tag{A.3}$$

Recalling the asymptotic form of $\mathcal{H}_1^{(2)}$ for small values of its argument (for example, see Kreyszig[19]), it can be easily seen that both $\mathcal{K}_{\mathsf{ae}}$ and $\mathcal{K}_{\mathsf{ac}}$ go to infinity as r^{-1}. Introducing the local coordinate (ξ,η), such that $\boldsymbol{y} \equiv (0,\eta)$ and $\boldsymbol{x} \equiv (\xi,0)$ (see Fig. 13), it follows that

$$\mathcal{I}^\varepsilon_{\mathsf{ac}} = \int_{-\varepsilon}^{\varepsilon} \left[\frac{-\eta}{2\pi\,(\xi^2+\eta^2)} + \mathrm{i}\,\eta \frac{\kappa^2}{16} \right] \mathrm{d}\xi = \mathcal{I}^\varepsilon_{\mathsf{ae}} + \frac{\mathrm{i}\varepsilon\kappa^2}{8}\,\eta. \tag{A.4}$$

It can be easily seen that

$$\mathcal{I}^\varepsilon_{\mathsf{ae}} = -\frac{1}{\pi} \arctan\frac{\varepsilon}{\eta}. \tag{A.5}$$

Taking the limit for $\boldsymbol{y} \to \boldsymbol{y}_0$ yields $\lim_{\eta\to 0} \mathcal{I}^\varepsilon_{\mathsf{ae}} = \lim_{\eta\to 0} \mathcal{I}^\varepsilon_{\mathsf{ac}} = -0.5$. Now, substituting the result into Eq. (A.2), it is possible to indefinitely shrink Γ_ε to obtain for both acoustic and aerodynamics

$$\lim_{\varepsilon\to 0} \mathcal{I}(\boldsymbol{y}_0) = -\frac{1}{2}\, \varphi(\boldsymbol{y}_o) + \int_\Gamma \varphi(\boldsymbol{x}) \frac{\partial G(\boldsymbol{y},\boldsymbol{x})}{\partial n}\, \mathrm{d}\Gamma. \tag{A.6}$$

Substituting Eq. (A.6) into Eq. (2) follows that the domain function $E(\boldsymbol{y})$ equals 0.5 at a regular point $\boldsymbol{y}_0 \in \Gamma$. The remaining part of the integral (*i.e.*, the integral appearing in Eq. (A.6)) is a convergent improper integral and can be integrated using standard adaptive quadrature formulae capable of isolating the singularity of the integrand function.

In the present work, the Gauss-Kronrod adaptive quadrature rules have been used, as implemented in the GNU Scientific Library.[20] The results obtained are presented in Table 3, where the value of the real part of the integral in Eq. (A.6) is reported for different number of Gaussian integration points N_G. The influence of a partition of the boundary Γ into N_Γ parts has been also included. Two geometries have been analyzed: a circle and a flower-like geometry represented by the parametric equations $x(\theta) = [1+0.5\sin(5\theta)]\cos(\theta)$, $y(\theta) = [1+0.5\sin(5\theta)]\sin(\theta)$. As can be seen, the convergence of the integration is extremely fast, giving values substantially converged even with the coarsest quadrature rule. In addition, the partition of Γ has no effects on the integral values, confirming the validity of the NURBS global representation for the meshless solution of the BIE. Needless to say, in presence of complex geometries, presenting slope and curvature discontinuities, the assumption of unit weights in Eq. (8) makes the accurate approximation of the integrand impossible, thus causing the numerical convergence of the quadrature rule impossible to be achieved when extended to the whole boundary. Nevertheless, in those specific cases the geometry can be partitioned into macro patches having the desired level of smoothness and the integrals in Eqs. (2) and (3) can be split into their restrictions to each continuous patch.

Rotor Faults Diagnosis Using Artificial Neural Networks and Support Vector Machines

Sukhjeet Singh and Navin Kumar

School of Mechanical, Materials and Energy Engineering, Indian Institute of Technology Ropar, Nangal Road, Rupnagar, Punjab, India

(Received 3 June 2013; accepted 1 January 2014)

Unbalance and misalignment are the commonly occurring faults in rotating mechanical systems. These faults are caused mainly due to improper installation or premature failure of the machine components. Detection and diagnosis of faults in rotating machinery is crucial for its optimal performance. In this study artificial neural networks (ANN) and support vector machine (SVM) techniques have been used to determine the effectiveness of statistical features for fault diagnosis in rotating mechanical system using healthy and faulty rotors. The vibration signature responses are obtained and analyzed for healthy shaft without disk (HSWD), healthy shaft with an unbalanced disk (HSWUD), centrally bent shaft without disk (CBSWD) and centrally bent shaft with an unbalanced disk (CBSWUD) with zero bow phase angle. Their predominant features were fed as input for training and testing ANN and SVM, whereas the relative efficiency of these techniques have been compared for classifying the faults in the test system. The study concludes that these machine learning algorithms can be used for fast and reliable diagnosis of rotor faults.

NOMENCLATURE

T	Bias or threshold
λ_i	Lagrange multipliers
$U(\lambda)$	Lagrange function
ϕ_j^h	Bias for hidden layer
net_{mn}^h	Net input to hidden layer
net_{mk}^o	net input to output layer
μ_{mn}	n^{th} input of the m^{th} input vector
κ_i	Distance between the margin and the examples μ_i that are lying on the wrong side of the margin
ϕ_j^o	Bias for output layer
E_m	Sum of squares error
O_{mk}^o	Output of output layer
V_m	Sum of squares error
$\triangle_m^o$	Change in weight w.r.t weight change
O_{mj}^h	Output of hidden layer
u_{jk}^h	Synaptic weight between hidden and output layer
M	Number of iterative step
Z_{mk}	Desired output

1. INTRODUCTION

Rotating machinery diagnostics is an essential function in industrial processes and power generation applications. Failures in a rotating machinery system are quite common and their proper diagnosis depends upon accurate detection of the fault and its location. Most of the faults are caused either because of the incorrect manufacturing practices or because of the extreme operating conditions. These may result in excessive heat generation, looseness and other unwanted wears and tears of the rotating parts causing financial losses. Therefore, a continuous monitoring system is required to detect and diagnose the faults to avoid any such situation.

Faults associated with the rotor-bearing system like unbalanced rotor,;[1,2] bent rotor,;[3] misaligned rotor,[4] and rotor rub[5,6] are discussed in the literature. Many techniques and tools are already in practice for the continuous diagnosis of the various components of the rotating machinery. Li et al.[7] used the hidden Markov models (HMM) techniques in order to detect various faults namely: rotor unbalance, rotor to stator rub, oil whirl and pedestal looseness in a rotating machinery under speed-up and speed-down conditions. Rolling element bearings defects like outer race, inner race, ball spin and cage faults were discussed by different researchers[8–12] using different techniques. Also, back-propagation learning algorithm and a multi-layer network have been used to validate the test data for unknown faults.[13]

Fault diagnosis of load machines like gearboxes for common defects like missing tooth and wear of the gear tooth were carried out using wavelet techniques.[14] Kolmogorov-Smirnov test was used by Kar and Mohanty for the detection of faulty gears.[15] The performance of gear fault was detected using ANN and SVM by Samanta.[16] Support vector machines (SVM) were used in the fault diagnosis of machines.[17]

The present work deals with the extraction of statistical features from the vibration signatures of a rotor-bearing system and classification of shaft faults using artificial neural network (ANN) and support vector machine (SVM). The flow chart for the shaft health diagnosis is shown in Fig. 1.

A group of statistical features like range, root mean square value, crest factor, kurtosis, skewness and standard deviation have been extracted from time domain. The setup details for simulating the combined unbalance and bent rotor fault in a real experimental machine have been discussed in Section 2.

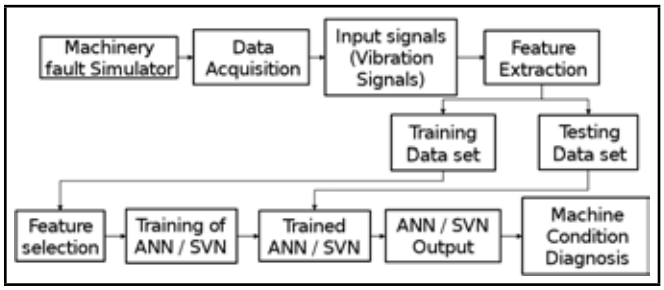

Figure 1. Flow chart of shaft health diagnosis

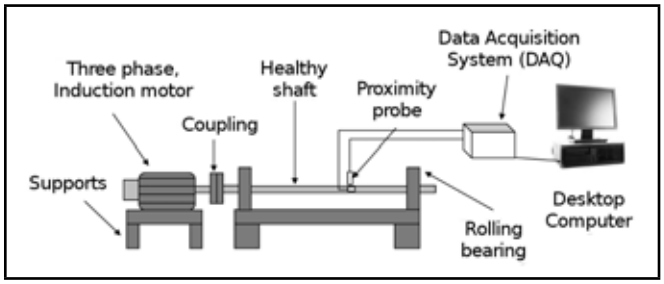

Figure 2. Line diagram of the experimental setup

Section 3 presents the background of the ANN and SVM. The wave forms of the healthy and faulty shaft signals are presented in Section 4. Salient statistical features from the acquired signals were extracted and compiled to form a feature vector which is fed to ANN/SVM for training and testing it is discussed in Section 4. The conclusions are discussed in Section 5.

2. EXPERIMENTAL SETUP AND DATA ACQUISITION

The experimental setup consists of a slotted aluminium disc mounted on a 19.05 mm diameter shaft (cold rolled steel) and the shaft was supported on two identical roller bearings. The schematic of the experimental setup is shown in Fig.2. A three phase 0.75 kW induction motor coupled with a variable frequency drive (VFD) was used for running this arrangement. Reverse dial gauge method was used to align the shaft with the motor end shaft. A pair of proximity probes were mounted radially (in horizontal and vertical directions) with an attachment on the rotor system.

Two shafts, one healthy (HS) and one centrally bent (CBS) with a bend of 200 microns were used to simulate different shaft unbalance conditions. For simulating unbalance, the aluminium disc has threaded holes in which nuts and bolts of predetermined weight of 17 g could be screwed. The bending natural frequency (ω_n) of the healthy and centrally bent shafts was 59.9 Hz as obtained from the rap test. Data was acquired using a NI 9234 data acquisition card at the sampling rate of 1651 Hz for 1.24 seconds. The numbers of acquired samples were 2048. The system was run from 1.15 Hz to 40.25 Hz with an increment of 1.15 Hz and data was acquired for healthy and faulty shaft conditions. These time-domain data were pre-processed to extract the features which are used as inputs to the classifiers - ANN and SVM techniques.

3. FEATURE EXTRACTION AND SELECTION

The optimal performance of fault diagnosis of a rotating machine depends on appropriate features extraction and features selection techniques. The selection of essential features from the test machine is an important step towards increasing the overall effectiveness of the fault diagnosis process. For analyzing signals and extracting features various techniques are used such as time domain, frequency domain and time-frequency domain.[18]

Six statistical features including range, root mean square value, crest factor, kurtosis, skewness and standard deviation were used each for horizontal and vertical response (acquired with a pair of proximity probes) for the healthy and faulty shafts. Then, statistical features of the healthy and the faulty shafts were compiled to form a vector as shown in Table 1 along with speed as an additional feature. A total of 140 instances of experiments were used for the present work. These features are discussed below in detail:

- Range is the difference between the maximum and minimum value of a signal.

- Standard deviation is the measure of dispersion of data sets from its mean. The more spread of data produce higher deviation. Mean and standard deviation can be described as following:

$$x_{mean} = \frac{1}{m}\sum_{i=1}^{m} x(i);$$
$$x_{std} = \sqrt{\frac{\sum_{i=1}^{m}(x(i) - x_{mean})^2}{m-1}}; \qquad (1)$$

  where $x(i)$ is a signal series for $i = 1, 2, \ldots, m$ and m is the number of data points.

- RMS is used to measure the overall power content of the signal. Skewness use the normalized third central moment. Mathematically RMS and skewness can be defined as:

$$x_{rms} = \sqrt{\frac{\sum_{i=1}^{m}(x(i)^2}{m}};$$
$$x_{skew} = \sqrt{\frac{\sum_{i=1}^{m}(x(i) - x_{mean})^3}{(m-1)x_{std}^3}}. \qquad (2)$$

- Kurtosis measures the relative peak-edness of the distribution as compared to a normal distribution. Crest factor computes the ratio of the peak level of data over the RMS level. There-fore, the results from the crest factor show the peak of data corresponding to an increase in crest factor value.

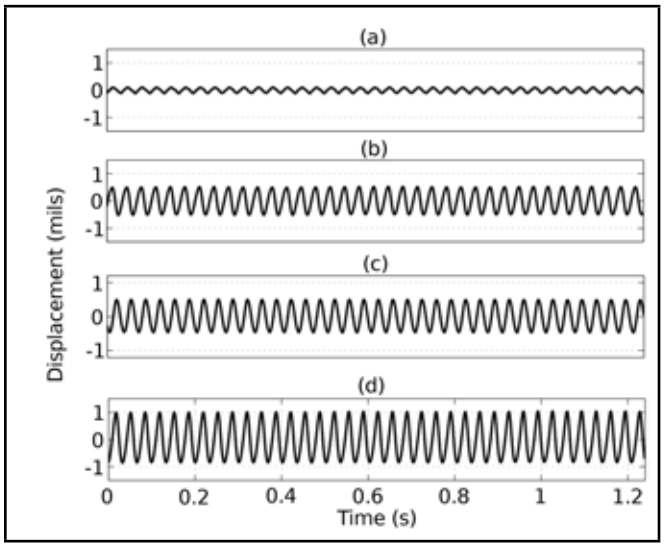

Figure 3. (a, b, c and d) Displacement waveform of the healthy shaft without disk, healthy shaft with unbalanced disk, centrally bent shaft without disk and centrally bent shaft with unbalanced disk with BP of 0° at $\omega_n/2$ respectively

$$x_{kurt} = \sqrt{\frac{\sum_{i=1}^{m}(x(i) - x_{mean})^4}{(m-1)x_{std}^4}};$$

$$x_{cf} = \frac{x_{max}}{x_{rms}}. \tag{3}$$

The faults which are fully developed or are in incipient stage may not be detected in time domain signals, or could be masked/buried in the noise along with the signals. But, it has already been established by many authors that the fault can be detected using the time domain statistical features even for the shortest duration of the data acquired for the fault.[10,11,19] The displacement waveforms of the HSWD, HSWUD, CBSWD and CBSWUD with BP of 0° at $\omega_n/2$ are shown in Fig. 3.

3.1. Artificial neural network

Artificial neural network (ANN) is an interconnected network of models based on the biological learning processses of human brain. There are a number of applications of the ANNs in regression analysis, robotics, data analysis, pattern recognition and control. Multi-layer perceptron (MLP) has been used by different researchers in the past for different types of faults and signals taken with the different sensors.[20] Essentially, an ANN consists of an interconnected group of artificial neurons. These neurons use a mathematical or computational model for information processing. ANN is an adaptive system that takes its decisions based on information that passes through the network.[21] The neuronal model as explained in Fig. 4 also includes bias (threshold) which is an external parameter of neural network with constant input.[22]

3.2. Back propagation (BP) algorithm

The structure of neurons in a neural network is known as the network architecture. Three different classes of network architecture are: single layer feed-forward network, multi-layer feed-forward network and recurrent networks. Another important type of neural networks is a multi-layer feed forward network, which is also known as multi-layer perceptrons (MLPs). Back propagation (BP) algorithm is shown in Fig. 5. It consists of two steps which are known as forward pass and backward pass.

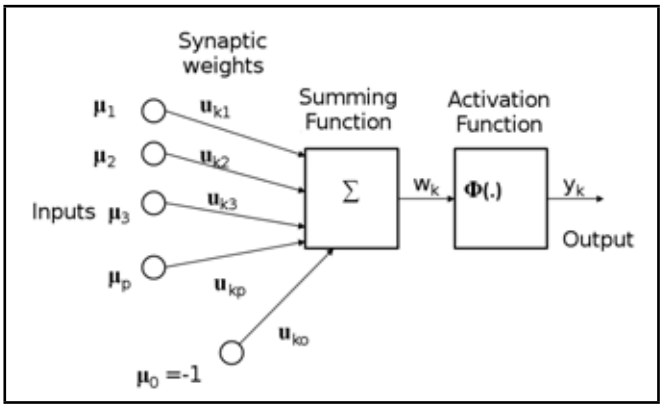

Figure 4. Model of a single non-linear neuron

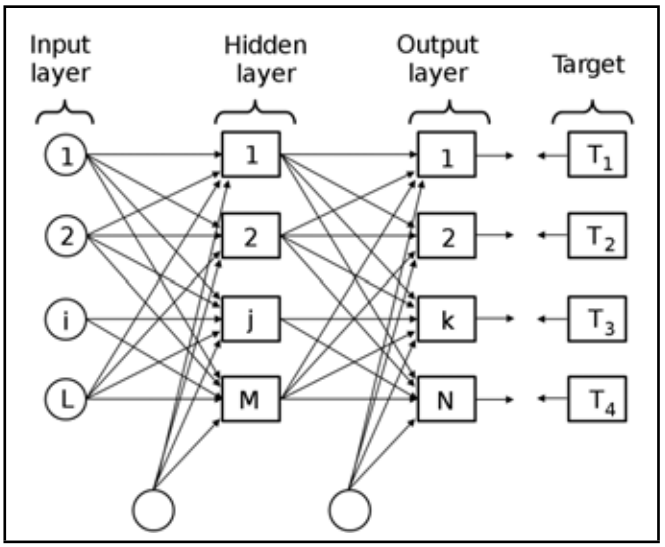

Figure 5. Back propagation algorithm in multi-layer neural network

3.3. Support vector machine

Support Vector Machines (SVMs) are a new generation learning systems which are based on the statistical learning theory. They belong to the class of supervised learning algorithms in which the learning machine is given a set of inputs with the associated outputs. Cristianini (2000) used SVM for pattern recognition and classification.[23] A simple case of two classes separated by a linear classifier points are shown by triangles and squares in Fig. 6. The plane that separates the two classes is called hyper plane, H. H_1 and H_2 (shown by dashed lines) are the planes that are parallel to plane H and pass through the sample points closest to plane H in these two classes. The planes parallel to H are designated as H_1 and H_2 and they pass through the sample points nearest to H amongst these classes. The distance between the two parallel planes is known as margin. The closest placed data points that are used

Table 1. Sample input vector for ANN/SVM techniques

Horizontal Proximity Probe Response						Vertical Proximity Probe Response							
Features													
Range	RMS	Crest Factor	Kurto-sis	Skew-ness	Standard Deviation	Range	RMS	Crest Factor	Kurto-sis	Skew-ness	Standard Deviation	Speed	Class
1	2	3	4	5	6	7	8	9	10	11	12	13	
0.164	0.053	1.519	1.661	-0.286	0.052	0.343	0.117	1.421	1.965	-0.599	0.113	1.15	HSWD
0.18	0.06	1.464	1.585	-0.037	0.059	0.388	0.124	1.501	1.697	-0.026	0.123	2.3	HSWD
0.105	0.036	1.621	1.643	-0.401	0.035	0.29	0.097	1.607	1.466	-0.029	0.096	1.15	HSWUD
0.127	0.04	1.713	1.573	0.222	0.04	0.334	0.104	1.698	1.626	0.234	0.103	2.3	HSWUD
0.748	0.26	1.492	1.769	0.464	0.251	1.928	0.651	1.518	1.579	-0.13	0.645	1.15	CBSWD
0.79	0.278	1.475	1.545	0.193	0.277	2.035	0.707	1.458	1.561	0.152	0.705	2.3	CBSWD
0.674	0.23	1.527	1.582	-0.066	0.229	1.282	0.454	1.44	1.762	0.47	0.439	1.15	CBSWUD
0.74	0.266	1.46	1.473	0.131	0.266	1.386	0.476	1.489	1.572	-0.122	0.472	2.3	CBSWUD

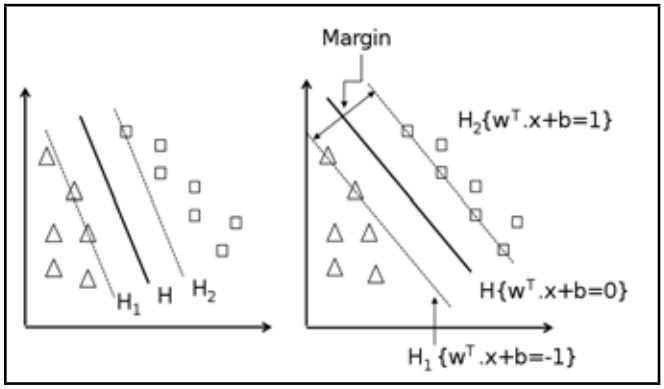

Figure 6. Hyper-plane classifying two classes : (a) small margin (b) large margin

to define the margin are recognized as support vectors or margin of separation.[20] The aim of the SVM is to obtain a linear hyper-plane between the H_1 and H_2 hyper-planes so that the margin is maximized.

This problem is solved by reducing it to a convex optimization problem: that is minimizing a quadratic function under linear inequality constraints.[23]

4. RESULTS

The displacement waveforms of the HSWD, HSWUD, CBSWD and CBSWUD with BP of 0° at $\omega_n/2$ are shown in Fig. 3. The vibration amplitude of the HSWD is 0.095 mils (r.m.s. value), whereas for HSWUD it is 0.2482 mils (r.m.s. value) at $\omega_n/2$ rotational speed as shown in Figs. 3(a) and 3(b).

Similarly, for the CBSWD CBSWD with an unbalance running at 29.9 Hz with a bow phase angle of 0°, the vibration responses at $(\omega_n/2)$ are 0.4974 and 0.6428 mils (r.m.s. value) respectively. The term bow phase angle at 0° means that the unbalance and the bow are on the same side. So the amplitude of vibration of such a rotor should be higher than that of a healthy rotor running under same conditions.[24]

An increase in the amplitude of vibration is an indication of a deteriorating shaft condition. Also, the rate of increase of the amplitude is proportional to the degree of defect. It is quite possible to predict the trend of increase in the amplitude of the defective shafts by continuously monitoring the vibration responses. The operator of the machine should be skilled to predict about the type of the fault after looking into the vibration responses. Skilled operators are more difficult to hire because of their demand for higher salaries. Therefore, it becomes necessary to have an automatic fault diagnostic system which can predict the defect and advise the operator of an appropriate remedy to the problem.[25]

ANN/SVM training and classification of faults are carried out in WEKA software.[26] Training vectors are already compiled and are put as an input. The defects considered in the study are classified using ANN/SVM techniques are as follows: HSWD, HSWUD, CBSWD and CBSWUD zero bow phase angle.

The training vector extracted from the data is shown in Table 1. In Table 2, the magnitudes of the various statistical parameters like range, root mean square value, crest factor, kurtosis, skewness and standard deviation features for every shaft condition have been mentioned at the rotor speed $\omega_n/2$. It is pertinent to mention here that at $\omega_n/2$ speed an increase in the magnitude of statistical variables namely- range, r.m.s., standard deviation and skewness was observed with an increase in the fault condition in comparison to HSWD condition. However, the crest factor and kurtosis variable values show an increase for HSWD condition and they become almost constant for all the remaining shaft conditions at this speed.

The effect of speed on the statistical variables identified for the present study were also studied. It was observed that except for crest factor and kurtosis, all other statistical variables followed a general trend of an increase in the magnitude with an increase of speed as shown in Figs. 7-10.

From the acquired responses, it was analyzed that the amplitude of the vibrations increase with an increase in rotor speed (Fig.3). But it becomes very difficult to differentiate shaft faults individually on the basis of time and frequency domain. Therefore, ANN and SVM techniques were applied to closely related faults for speedy diagnosis on the basis of their statistical features.

These features were fed to WEKA software[26] for selecting the appropriate features in order to make decisions using machine learning algorithms. In a multi-class prediction, the results of a test set are often displayed as a two dimensional confusion matrix (Table 3) with a row and column for each class. Each matrix element showed the number of test examples for which the actual class was the row and the predicted class was the column. Results corresponded to large numbers down the main diagonal and small ideally zero; off-diagonal elements

Table 2. Magnitudes of the various statistical features at the rotor speed ($\omega_n/2$)

	Range	RMS	Crest factor	Kurtosis	Skewness	Standard deviation
HSWD	0.2207	0.0687	1.5235	1.6886	-0.1488	0.0687
HSWUD	1.0431	0.357	1.4714	1.5034	0.0164	0.3571
CBSWD	0.9731	0.3373	1.498	1.508	0.081	0.3374
CBSWUD	1.893	0.6452	1.6146	1.5684	0.2035	0.6454

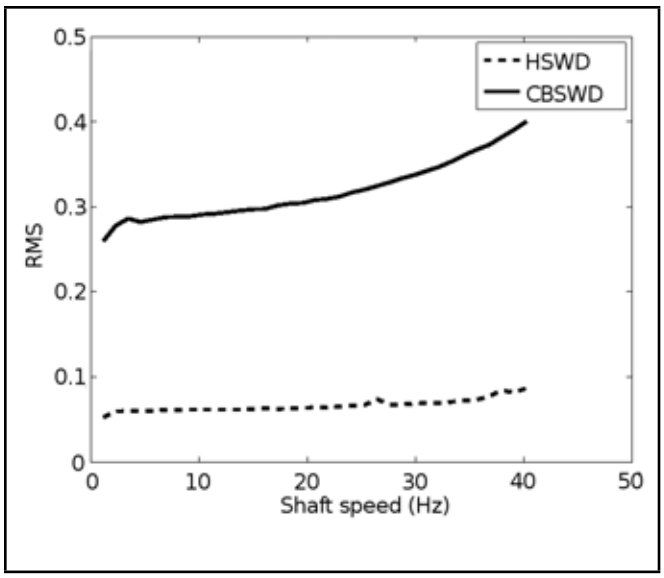

Figure 7. RMS parameter of HSWD and CBSWD at different shaft speeds

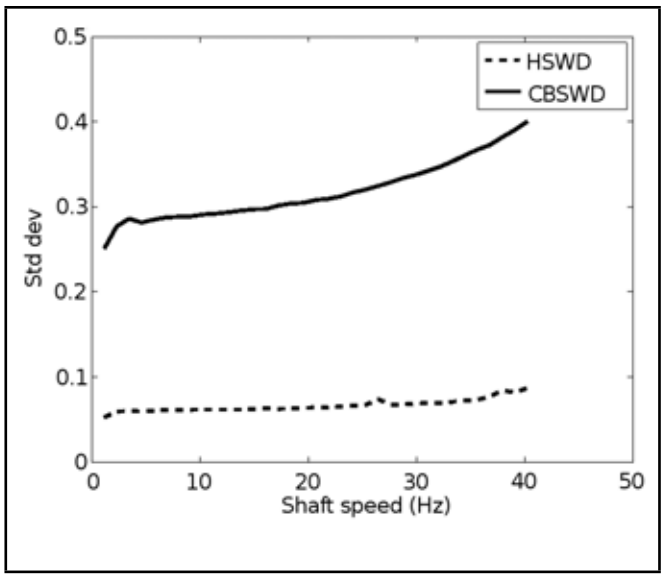

Figure 9. Standard deviation parameter of HSWD and CBSWD at different shaft speeds

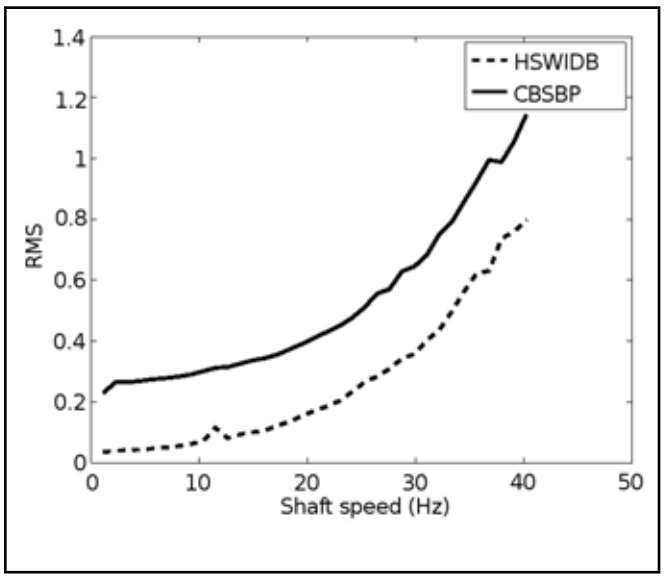

Figure 8. RMS parameter of HSWUD and CBSWUD at different shaft speeds

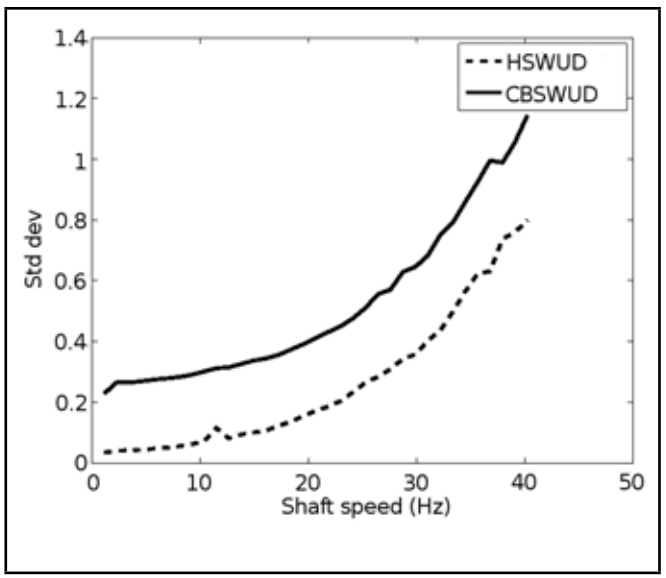

Figure 10. Standard deviation parameter of HSWUD and CBSWUD at different shaft speeds

gave an accurate prediction. After selecting "fault" as an attribute for class, classification was started and the classifier output consisted of the confusion matrix, detailed accuracy by class and evaluation of the success of the numeric prediction.

From Table 3, we inferred that ANN correctly predicted 35, 34, 35 and 35 cases, while SVM classified 35, 34, 35 and 35 cases correctly for HSWD, HSWUD, CBSWD and CBSWUD at zero bow phase angle.

The detailed accuracy of each class has been reported in Table 4. It also gives us the information about TP rate (true positive rate is the number of correctly classified fault divided by the total number of instances for that fault), FP rate (false positive rate is the number of incorrectly classified fault divided by the total number of instances other than the considered fault), precision, recall and F-measure values for the 4 classes by using ANN and SVM.

The values of various measures of correct classification of faults are tabulated in Table 5. In the present study, the results presented in Table 5 are based on the numeric prediction based on 140 instances and accuracy achieved is 99.2857 % which is better than that of reported by Vyas and Kumar[13] (90%) and Kankar et al.[19] (95.54 %). Vyas and Kumar's[13] results are based on 600 instances for different faults and 100 samples for each fault, whereas Kankar et al.[19] have taken 359 instances

Table 3. Confusion matrix

HSWD		HSWUD		CBSWD		CBSWUD		Classified as
ANN	SVM	ANN	SVM	ANN	SVM	ANN	SVM	
35	35	0	0	0	0	0	0	HSWD
1	1	34	34	0	0	0	0	HSWUD
0	0	0	0	35	35	0	0	CBSWD
0	0	0	0	0	0	35	35	CBSWUD

Table 4. Detailed accuracy by class

TP rate		FP rate		Precision		Recall		Fmeasure		Class
ANN	SVM	ANN	SVM	ANN	SVM	ANN	SVM	ANN	SVM	
1	1	0.01	0.01	0.972	0.972	1	1	0.986	0.986	HSWUD
0.971	0.971	0	0	1	1	0.971	0.971	0.986	0.986	HSWUD
1	1	0	0	1	1	1	1	1	1	CBSWD
1	1	0	0	1	1	1	1	1	1	CBSWUD

Table 5. Evaluation of the success of the numeric prediction

Parameters	Values (ANN)		Values (SVM)	
Correctly classified instances	139	99.2857	139	99.2857
Incorrectly classified instances	1	0.7143	1	0.7143
Kappa Statistic	0.905		0.9905	
Mean absolute error	0.013		0.2506	
Root mean squared error	0.0617		0.3128	
Relative absolute error	3.456		66.7765	
Root relative squared error	14.2276		72.1726	
Total number of instances	140		140	

for healthy and faulty rotors and bearings. Also, classification accuracy of SVM and ANN is much better than reported by Meyer et al.[27]

5. CONCLUSIONS

This study presents a potential application of machine learning methods ANNs and SVMs for the fast and reliable detection of shaft faults. Features were extracted from time-domain vibration signals using statistical techniques. The roles of different vibration signals obtained with or without a disc at various speeds have been investigated. The time responses showed that the amplitudes of vibration increase with the addition of different faults. The combined rotor fault that consists of a centrally bent shaft carrying an unbalanced disk at the centre has the high response of the vibrations at almost all the speeds. In total six features have been considered including range, root mean square value, crest factor, kurtosis, skewness and standard deviation features for every shaft condition have been mentioned at the rotor speed $\omega_n/2$. The time taken to run the model by SVM was remarkably less as compared to ANN technique. In our study a healthy and a centrally bent shaft (with zero bow phase angle) have been diagnosed using ANN and SVM at rotor speed $\omega_n/2$ with the success rate as high as 99.2857%. No better results have been reported till date using same conditions at least in the open literature. Present study focuses on the supervised machine learning whereas unsupervised machine learning studies may also be used for detection of rotor faults. Furthermore, this technique can be also used for the diagnosis of multiple fault cases (combination of misalignment, bent rotor and bearing faults). This study presents a potential application of machine learning methods ANNs and SVMs for the fast and reliable detection of shaft faults. Features were extracted from time-domain vibration signals using statistical techniques. The roles of different vibration signals obtained with or without a disc at various speeds have been investigated. The time responses showed that the amplitudes of vibration increase with the addition of different faults. The combined rotor fault that consists of a centrally bent shaft carrying an unbalanced disk at the centre has the high response of the vibrations at almost all the speeds. In total six features have been considered including range, root mean square value, crest factor, kurtosis, skewness and standard deviation features for every shaft condition have been mentioned at the rotor speed n/2. The time taken to run the model by SVM was remarkably less as compared to ANN technique. In our study a healthy and a centrally bent shaft (with zero bow phase angle) have been diagnosed using ANN and SVM at rotor speed n/2 with the success rate as high as 99.2857%. No better results have been reported till date using same conditions at least in the open literature. Present study focuses on the supervised machine learning whereas unsupervised machine learning studies may also be used for detection of rotor faults. Furthermore, this technique can be also used for the diagnosis of multiple fault cases (combination of misalignment, bent rotor and bearing faults).

REFERENCES

[1] Nicholas, J., Gunter, E., and Allaire, P., "Effect of residual shaft bow on unbalance response and balancing of a single mass flexible rotor - 1 Unbalance response," *Journal of Engineering for Power-Transactions of the ASME,* **98**(2), 171–181 (1976).

[2] Nicholas, J., Gunter, E., and Allaire, P., "Effect of residual shaft bow on unbalance response and balancing of a single mass flexible rotor - 2 Balancing," *Journal of Engineer-*

ing for Power-Transactions of the ASME, **98**(2), 182–189 (1976).

[3] Edwards, S., Lees, A., and Friswell, M., "The identification of a rotor bend from vibration measurements," *Society for Experimental Mechanics, Inc, 16th International Modal Analysis Conference* **2**, 1543–1549 (1998).

[4] Patel, T. H. and Darpe, A. K., "Experimental investigations on vibration response of misaligned rotors," *Mechanical Systems and Signal Processing* **23**(7), 2236–2252 (2009).

[5] Bachschmid, N., Pennacchi, P., and Vania, A. , "Thermally induced vibrations due to rub in real rotors," *Journal of Sound and Vibration* **299**(45), 683–719 (2007).

[6] Patel, T. H. and Darpe, A. K., "Study of coast-up vibration response for rub detection," *Mechanism and Machine Theory* **44**(8), 1570–1579 (2009).

[7] Zhinong, Li., Zhaotong, Wu., Yongyong, He., and Chu, Fulei., "Hidden Markov model-based fault diagnostics method in speed-up and speed-down process for rotating machinery," *Mechanical Systems and Signal Processing* **19**(2), 329 – 339 (2005).

[8] Samanta, B. and Al-Balushi K. R., "Artificial neural network based fault diagnostics of rolling element bearings using time-domain features," *Mechanical Systems and Signal Processing* **17**(2), 317–328 (2003).

[9] Kar,C. and Mohanty A. R., "Application of Kolmogorov - Smirnov test in ball bearing fault diagnosis," *Journal of Sound and Vibration* **269**(1-2), 439–454 (2004).

[10] Bhavaraju, K. M., Kankar, P. K., Sharma, S. C., and Harsha, S. P., "A comparative study on bearings faults classification by artificial neural networks and self-organizing maps using wavelets," *International Journal of Engineering Science and Technology* **2**(5), 1001–1008 (2010).

[11] Kankar, P. K., Sharma, S. C. and Harsha, S. P. , "Fault diagnosis of ball bearings using continuous wavelet transform," *Applied Soft Computing* **11**(2), 2300–2312 (2011).

[12] Kankar, P. K., Sharma, S. C. and Harsha, S. P., "Fault diagnosis of high speed rolling element bearings due to localized defects using response surface method," *Journal of Dynamic Systems, Measurement, and Control* **133**(3), 0310071–03100714 (2011).

[13] Vyas, N. S. and Satish kumar, D., "Artificial neural network design for fault identification in a rotor-bearing system," *Mechanism and Machine Theory* **36**(2), 157–175 (2001).

[14] Rafiee, J., Rafiee, M. A., and Tse, P. W., "Application of mother wavelet functions for automatic gear and bearing fault diagnosis," *Expert Systems with Applications* **37**(6), 4568–4579 (2010).

[15] Kar, C. and Mohanty A. R., "Multistage gearbox condition monitoring using motor current signature analysis and Kolmogorov - Smirnov test," *Journal of Sound and Vibration* **290**(1–2), 337–368 (2006).

[16] Samanta, B., "Gear fault detection using artificial neural networks and support vector machines with genetic algorithms," *Mechanical Systems and Signal Processing* **18**(3), 625–644 (2004).

[17] Widodo, A. and Yang, B. S. , "Support vector machine in machine condition monitoring and fault diagnosis," *Mechanical Systems and Signal Processing* **21**, 2560–2574 (2007).

[18] Mahamad, A. K. and Hiyama, T., "Development of artificial neural network based fault diagnosis of induction motor bearing," in *Power and Energy Conference,PECon. IEEE 2nd International*, 1387–1392 (2008).

[19] Kankar, P. K., Sharma, S. C. and Harsha, S. P., "Vibration-based fault diagnosis of a rotor bearing system using artificial neural network and support vector machine," *International Journal of Modelling, Identification and Control* **15**(3), 185–198 (2012).

[20] Haykin, S., *Neural Networks: A Comprehensive Foundation*, Prentice Hall PTR, New York, NY, USA (1998).

[21] Zurada, J., *Introduction to Artificial Neural Systems*, West St. Paul, Minn. (1992).

[22] Kankar, P. K.,*Fault diagnosis of rolling element bearings using vibration signature analysis*. PhD thesis, Department of Mechanical and Industrial Engineering, Indian Institute of Technology, Roorkee, India (2011).

[23] Cristianini, N. and Shawe-Taylor, J., *An introduction to support vector machines: and other kernel-based learning methods*, Cambridge University Press, New York, NY, USA (2000).

[24] Rao, J. S., "A note on Jeffcott warped rotor," *Mechanism and Machine Theory* **36**(5), 563–575 (2001).

[25] Tse, W. P. and Atherton, D. P. , "Prediction of machine deterioration using vibration based fault trends and recurrent neural networks," *Journal of Vibration and Acoustics* **121**(3), 355–362 (1999).

[26] Hall, M., Frank, E., Holmes, G., Pfahringer, B., Reutemann, P., and Witten, I. H., "The WEKA data mining software: an update," *SIGKDD Explor. Newsl.* **11**(1), 10–18 (2009).

[27] Meyer, D., Leisch, F. and Hornik, K. "The support vector machine under test," *Neurocomputing* **55** (12), 169–186 (2003).

Nonlinear Vibration Analysis of Flexible Hoisting Rope with Time-Varying Length

Ji-hu Bao

Hefei General Machinery Research Institute, Hefei 230031, China
School of Mechanical Engineering, Shanghai Jiaotong University, Shanghai 200240, China

Peng Zhang, Chang-ming Zhu and Ming Zhu

School of Mechanical Engineering, Shanghai Jiaotong University, Shanghai 200240, China

(Received 3 March 2013; accepted 14 January 2015)

The nonlinear vibration of a flexible hoisting rope with time-varying length and axial velocity is investigated. The flexible hoisting rope is modeled as a taut translating string with a rigid body attached at its low end. A systematic procedure for deriving the system model of a flexible hoisting rope with time-varying length and axial velocity is presented. The governing equations were developed by employing the extended Hamilton's principle considering coupling of axial movement and flexural deformation of the rope. The derived governing equations are nonlinear partial differential equations(PDEs) with time-varying coefficients. The Galerkin's method and the 4th Runge-Kutta method were employed to numerically analyze the resulting equations. Further, the dynamic stability of the flexible hoisting rope was investigated according to the Lyapunov stability theory. The motions of an elevator hoisting system were presented to illustrate the proposed mathematical models. The results of simulation show that the dynamic motions of the flexible hoisting string are stable during downward movement but are unstable during upward movement. The proposed systematic procedures in analyzing the dynamic stability can facilitate further development in dynamic control of the flexible hoisting system in practice.

NOMENCLATURE

a	Axial acceleration of the string (m/s^2)
$\mathbf{A}$, $\mathbf{B}$	Matrix differential operators
$\mathbf{C}$	Damp matrixes
d	Diameter of the string (m)
E	Young's Modulus of the string (Pa)
E_k	Kinetic energy of flexible hoisting system (J)
E_e	Elastic strain energy of the string (J)
E_g	Gravitational potential energy of flexible hoisting system (J)
g	Gravitational constant (m/s^2)
$\mathbf{i}$	Unit vector along the x-axes
i	Integer
I	Inertia (m^4)
$\mathbf{I}$	$n \times n$ identity matrix
$\mathbf{j}$	Unit vector along the y-axes
j	Integer
k	Integer
$\mathbf{K}$	Stiffness matrixes
l	Length of the string (m)
m	Mass of rigid body (kg)
$\mathbf{M}$	Mass matrixes
n	Number of included modes
P	Longitudinal tension (N)
q_i	Generalized coordinates
$\mathbf{Q}$	Vectors of generalized coordinates
$\mathbf{R}$	Position vector of the string
$\mathbf{R_c}$	Position vector of the rigid body
t	Time (s)
T	Lyapunov candidate function
U	State vector
v	Axial velocity of the string (m/s)
$\mathbf{V}$	Velocity vector of the string
$\mathbf{V_c}$	Velocity vector of the rigid body
x	Spatial variable (m)
y	Transverse displacement of the string (m)
ζ	Transformed spatial variable
ε	Strain measure
ρ	Linear density of the string (kg/m)
λ_k	Eigenvalue ($k = 1, 2, 3, 4$)
ξ_k	Real parts of eigenvalue ($k = 1, 2, 3, 4$)
φ_i	Trial function used in Eq. (19)
δ_{ij}	Kronecker delta
ω_k	Imaginary parts of eigenvalue ($k = 1, 2, 3, 4$)
$\mathbf{\Lambda}$	Eigenvector

1. INTRODUCTION

Ropes with time-varying length are widely used in the hoisting industry such as mine hoists, elevators, cranes, etc; They are subject to vibration due to their high flexibility and relatively low internal damping characteristics.[1,2] Most often these systems are modeled as either an axially moving tensioned beam or as a string with time-varying length and a rigid body at its lower end.[3,4] It was reported that the vibration energy of the rope changed in general during elongation and shortening.[5–7] Zhang[8–11] and Bao[12,13] published a series of studies on vibration of a flexible hoisting system with arbitrarily varying length. Terumichi et al. assumed the velocity of the string was constant and studied the transverse vibrations of a string with time-varying length and a mass-spring system

at the lower end with theoretical and experimental methods.[14] Zhu[15] and Chen[16] investigated the control of an elevator cable with theoretical and experimental methods. A novel experimental method was developed to validate the uncontrolled and controlled lateral responses of a moving cable in a high-rise elevator and showed good agreement with the theoretical predictions. Nguyen and Hong studied the transverse vibration control of axially moving membranes by regulation of axial velocity.[17] A novel control algorithm that suppresses the transverse vibrations of an axially moving membrane system was developed. Ngo et al. investigated the control of an axially moving system. The Lyapunov function taking the form of the total mechanical energy of the system was adopted to ensure the uniform stability of the closed-loop system.[18] The results of experiments showed that the proposed control law was effective. Fung and Lin analyzed the transverse vibration of an elevator rope with time-varying length and the time-varying mass and inertia of rotors were considered.[19] A variable structure control scheme was proposed to suppress the transient amplitudes of vibrations. Chi and Shu calculated the natural frequencies associated with the vertical vibration of a stationary cable coupled with an elevator car.[20] Zhang presented a systematic procedure for deriving the model of a cable transporter system with arbitrarily varying cable length and proposed a Lyapunov controller to dissipate the vibratory energy.[21] Kaczmarczyk and Ostachowicz studied coupled vibration of a deep mine hoisting cable and built a distributed-parameter model. They found that the response of the catenary-vertical rope system may feature a number of resonance phenomena.[22] Zhang and Agrawal derived the governing equation of coupled vibration of a flexible cable transporter system with arbitrarily varying length.[23]

While an extensive number of studies focus individually on vibration characteristics of the rope with time-varying length, the dynamic stability of the rope has also been studied by several researchers. Lee introduced a new technique to analyze free vibration of a string with time-varying length by dealing with traveling waves.[24] As the string length is shortened, free vibration energy increases exponentially, causing dynamic instability. Kumaniecka and Niziol investigated the longitudinal-transverse vibration of a hoisting cable with slow variability of the parameters.[25] The cable material non-linearity was taken into account and unstable regions were identified by applying the harmonic balance method. General stability characteristics of horizontally and vertically translating beams and strings with arbitrarily varying length and various boundary conditions were studied by Zhu and Ni.[26] While the amplitude of the displacement can behave in a different manner depending on the boundary conditions, the amplitude of the vibratory energy of a translating medium decreases and increases during extension and retraction, respectively.

Extensive research on the flexible hoisting rope with time-varying length has been conducted in the last few decades as aforementioned; however, the focus of most studies was restricted to cases with constant transport speed samples. Clearly, with the advancement of high-performance mechanical systems such as high-rise elevators, cranes and mine hoists, etc., the stability analysis of dynamical systems is very important. The linear dynamic characteristics and stability of the flexible hoisting rope with time-varying length and axial velocity are the subject of this investigation. The governing equations were developed employing the extended Hamilton's principle. The derived governing equations are shown to be linear partial differential equations (PDEs) with variable coefficients. On choosing proper mode functions that satisfy the boundary conditions, the solution of the governing equations was obtained using the Galerkin's method. The natural frequencies were computed from the eigenvalues based on the eigenvalue equations. The motions of an elevator hoisting system were illustrated to evaluate the proposed mathematical models. According to the numerical simulations, the dynamic motions of the flexible hoisting string are stable during downward movement but are unstable during upward movement. Based on the proposed fundamental dynamic analyses, further vibration control can be adopted for flexible hoisting systems in the near future.

2. MODEL OF FLEXIBLE HOISTING SYSTEM

A flexible hoisting system is simplify an axially moving string with time-varying length and a rigid body m at its lower end, as shown in Fig. 1. The rail and the suspension of the rail are assumed to be rigid. The string has Young's modulus E, diameter d and mass per unit length ρ. The origin of the coordinate is set at the top end of the string, and the instantaneous length of the string is $l(t)$ at time t. The instantaneous axial velocity, acceleration and jerk of the string are $v(t) = \dot{l}(t)$, $a(t) = \dot{v}(t)$, and $j(t) = \dot{a}(t)$, respectively, where the overdot denotes time differentiation. At any instant t, the transverse displacement of the string is described by $y(x,t)$, at a spatial position x, where $0 \leq x \leq l(t)$. The model is based on the following assumptions:

1. The parameters E, d and ρ of the string are always constants;

2. Only transverse vibration is considered here. The elastic distortion of the string arousing from the transverse vibration is much less than the length of the string;

3. All the damp and friction, and the influence of air currents are ignored.

2.1. Energy of Flexible Hoisting System

After the string is deformed, the position vector $\mathbf{R}$ of a point at x can be written as:[27]

$$\mathbf{R} = x(t)\,\mathbf{i} + y(x,t)\,\mathbf{j}; \tag{1}$$

where $\mathbf{i}$ and $\mathbf{j}$ are the unit vectors along the x-axes and y-axes, respectively. The material derivative of $\mathbf{R}$ yields the velocity vector

$$\mathbf{V} = v(t)\,\mathbf{i} + [y_t + v y_x]\,\mathbf{j}; \tag{2}$$

where the subscript t denotes partial differentiation with respect to time, and subscript x denotes partial differentiation with respect to space. Similarly, the position vector $\mathbf{R_c}$ and

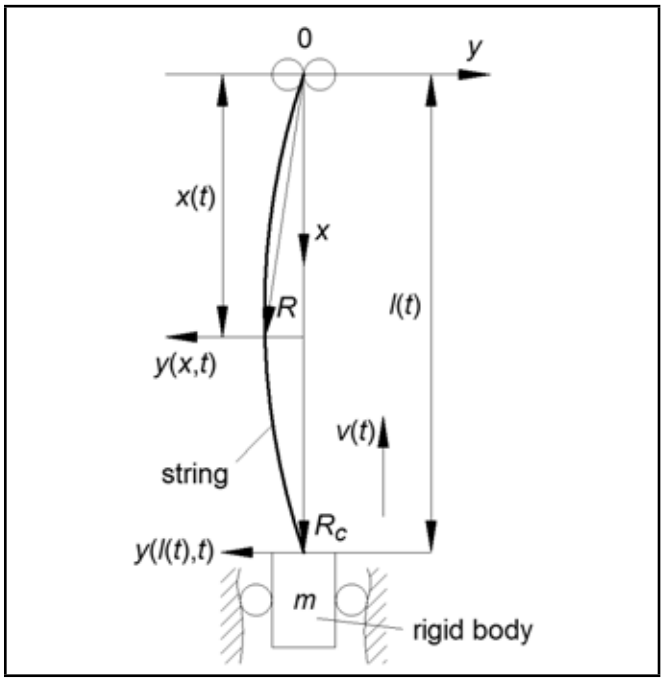

Figure 1. Schematic of a flexible hoisting string with time-varying length.

velocity vector $\mathbf{V_c}$ of the rigid body can be respectively written as:

$$\mathbf{R_c} = l(t)\,\mathbf{i} + y(l(t),t)\,\mathbf{j}; \tag{3}$$

$$\mathbf{V_c} = v(t)\,\mathbf{i} + y_t(l(t),t)\,\mathbf{j}. \tag{4}$$

Then, the kinetic energy of the flexible hoisting system is computed by

$$E_k(t) = \frac{1}{2}m\mathbf{V_c}\cdot\mathbf{V_c}\Big|_{x=l(t)} + \frac{1}{2}\rho\int_0^{l(t)}\mathbf{V}\cdot\mathbf{V}\,dx. \tag{5}$$

The first term on the right of Eq. (5) represents the kinetic energy of the rigid body; The second term represents the kinetic energy of the string. The elastic strain energy of the string is[28]

$$E_e(t) = \int_0^{l(t)}\left(P\varepsilon + \frac{1}{2}EA\varepsilon^2\right)dx. \tag{6}$$

The first term on the right of Eq. (6) represents the axial strain energy of the string, the second term represents the bending strain energy of the string. $P(x,t)$ is the longitudinal tension at spatial position x of the string at time t; The tension in a flexible hoisting string, arising from its weigh, is given by

$$P = [m + \rho\,(l(t) - x)]\,g; \tag{7}$$

and ε represents the strain measure at the spatial position x of the string and can be expressed as

$$\varepsilon = (ds - dx)/dx. \tag{8}$$

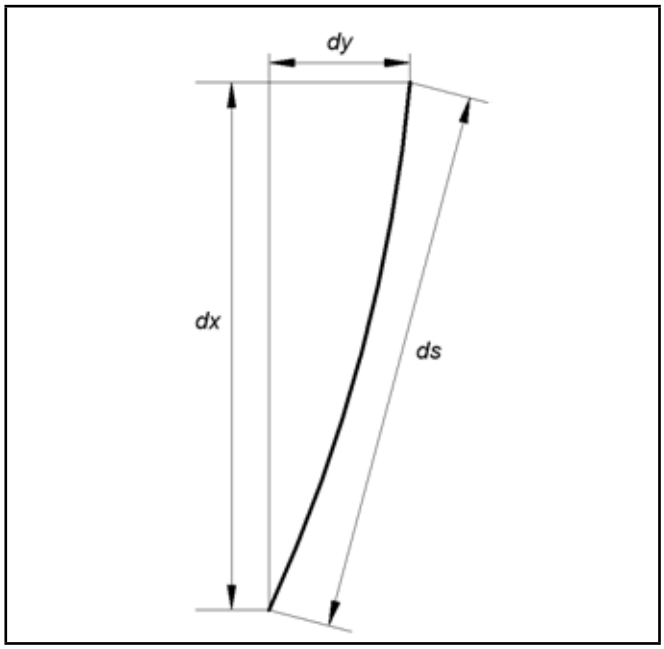

Figure 2. A small element of the string in a deformed position.

As shown in Fig. 2, ds can be expressed as

$$ds \approx \sqrt{1 + (dy/dx)^2}dx \approx \left[1 + \frac{1}{2}\left(\frac{\partial y}{\partial x}\right)^2 - \frac{1}{8}\left(\frac{\partial y}{\partial x}\right)^4 + \ldots\right]dx \approx \left[1 + \frac{1}{2}\left(\frac{\partial y}{\partial x}\right)^2\right]dx. \tag{9}$$

Substituting Eq. (9) into Eq. (8) yields

$$\varepsilon = \frac{1}{2}y_x^2. \tag{10}$$

When the reference elevation of the string with zero potential energy is defined at $x = 0$, then the gravitational potential energy of the flexible hoisting system is

$$E_g(t) = -\int_0^{l(t)}\rho g x(t)\,dx - mgl(t); \tag{11}$$

where g is the gravitational constant, the first term on the right of Eq. (11) represents the gravitational potential energy of the string, and the second term represents the gravitational potential energy of the rigid body.

2.2. Governing Equations of Motion

According to the characteristics of top restriction of the string, the boundary conditions at $x(t) = 0$ are

$$y(0,t) = 0, \qquad y_t(0,t) = 0. \tag{12}$$

Substitute Eqs. (5), (6), and (11) in the extended Hamilton's Principle,

$$\int_{t_1}^{t_2}\Big(\delta E_k(t) - \delta E_e(t) - \delta E_g(t)\Big)dt = 0; \tag{13}$$

and apply the variational operation. Because the length of the string $l(t)$ changes with time, the standard procedure for integration by parts with respect to the temporal variable cannot apply. Applying Leibnitz's rule and part integration results in the following expressions

$$\int_0^{l(t)} \rho\left(y_t + v y_x\right) \delta y_t \, dx = \rho \frac{\partial}{\partial t} \int_0^{l(t)} \left(y_t + v y_x\right) \delta y \, dx - \rho\left[v\left(y_t + v y_x\right) \delta y\right]\Big|_{l(t)} - \rho \int_0^{l(t)} \frac{\partial}{\partial t}\left(y_t + v y_x\right) \delta y \, dx. \quad (14)$$

Following the standard procedure for integration by parts with respect to the spatial variable and invoking Eq. (14), one obtains from Eq. (13),

$$\int_{t_1}^{t_2} \left[m \frac{\partial}{\partial t} y_t(l,t) + \left(P + \frac{1}{2} E A y_x^2\right) y_x\right]\Big|_{l(t)} \delta y(l,t) \, dt + \int_{t_1}^{t_2} \int_0^{l(t)} \left[\rho \frac{\partial}{\partial t}\left(y_t + v y_x\right) + \rho v \frac{\partial}{\partial x}\left(y_t + v y_x\right) - \frac{\partial}{\partial x}\left(\left(P + \frac{1}{2} E A y_x^2\right) y_x\right)\right] \delta y \, dx \, dt = 0. \quad (15)$$

Setting the coefficients of δy in Eq. (15) to zero yields the governing equation for the string,

$$\rho\left(y_{tt} + 2\dot{v} y_x + v^2 y_{xx}\right) - P_x y_x - P y_{xx} - \frac{3}{2} E A y_x^2 y_{xx} = 0, \quad 0 < x < l(t). \quad (16)$$

The first four terms in Eq. (16) correspond to the local, Coriolis, tangential, and centripetal acceleration, respectively. Equation (16) is a partial differential equation that describes the dynamics of the flexible hoisting string. The equation is defined over time-dependent spatial domain rendering the problem non-stationary. Hence, the exact solution to this problem is not available, and recourse must be made to an approximate analysis. In what follows, numerical techniques are employed to obtain an approximate solution for the governing equation.

3. DISCRETIZATION OF THE GOVERNING EQUATIONS

Equation (16) is a partial differential equation with infinite dimensions and many parameters are time-variant. It is impossible to obtain an exact analytical solution from Eq. (16). In this section, Galerkin's method was applied to truncate the infinite-dimensional partial differential equation into a linear finite-dimensional ordinary differential equation with time-variant coefficients. Then, they were solved with numerical methods. In order to map Eq. (16) onto the fixed domain, a new independent variable $\zeta = x/[l(t)]$ was introduced and the time-variant domain $[0, l(t)]$ for x was converted to a fixed domain $[0, 1]$ for ζ. According to the characteristic of a taut translating string, the solution of $y(x,t)$ was assumed in the forms[15,23]

$$y(x,t) = \sum_{i=1}^{n} \varphi_i(\zeta) q_i(t) = \sum_{i=1}^{n} \varphi_i\left(\frac{x}{l}\right) q_i(t); \quad (17)$$

where $q_i(t)$ $(i = 1, 2, 3, \ldots, n)$ is the generalized coordinate respect to $y(x,t)$, n is the number of included mode, and $\varphi_i(\zeta)$ is trial function,[15,23]

$$\varphi_i(\zeta) = \sqrt{2} \sin i\pi\zeta. \quad (18)$$

Consequently, expanding Eq. (17) results in the expressions for partial derivatives of transverse displacement functions:

$$y_x(x,t) = \frac{1}{l} \sum_{i=1}^{n} \varphi_i'(\zeta) q_i(t),$$

$$y_{xx}(x,t) = \frac{1}{l^2} \sum_{i=1}^{n} \varphi_i''(\zeta) q_i(t),$$

$$y_{xt}(x,t) = \sum_{i=1}^{n} \frac{1}{l} \varphi_i'(\zeta) \dot{q}_i(t) - \sum_{i=1}^{n} \left(\frac{\zeta v}{l^2} \varphi_i''(\zeta) + \frac{v}{l^2} \varphi_i'(\zeta)\right) q_i(t),$$

$$y_{tt}(x,t) = \sum_{i=1}^{n} \varphi_i(\zeta) \ddot{q}_i(t) - \frac{2\zeta v}{l} \sum_{i=1}^{n} \varphi_i'(\zeta) \dot{q}_i(t) + \sum_{i=1}^{n} \left(\frac{2\zeta v^2}{l^2} \varphi_i'(\zeta) - \frac{\zeta a}{l} \varphi_i'(\zeta) + \frac{\zeta^2 v^2}{l^2} \varphi_i''(\zeta)\right) q_i(t). \quad (19)$$

Substituting Eqs. (17)–(19) into Eq. (16), multiplying the governing equation by $\varphi_j(\zeta)$ $(j = 1, 2, 3, \ldots, n)$, integrating it from $\zeta = 0$ to 1, and using the boundary conditions and the orthonormality relation for $\varphi_i(\zeta)$, yield the discretized equation of transverse vibration for the flexible hoisting string with time-variant coefficients

$$\mathbf{M}\ddot{\mathbf{Q}} + \mathbf{C}\dot{\mathbf{Q}} + \mathbf{K}\mathbf{Q} + \mathbf{S}(\mathbf{Q}) = \mathbf{0}; \quad (20)$$

where $\mathbf{Q} = [q_1(t), q_2(t), \ldots, q_n(t)]^T$ is a vector of the generalized coordinate, $\mathbf{M}$, $\mathbf{C}$ and $\mathbf{K}$ are matrices of mass, dampness and stiffness with respect to $\mathbf{Q}$, respectively. $\mathbf{S}(\mathbf{Q})$ is a higher-order item of the generalized coordinate. The matrices are expressed as follows:

$$M_{ij} = \rho \delta_{ij}, \qquad C_{ij}(t) = \frac{2\rho v}{l} \int_0^1 (1-\zeta)\, \varphi_i'(\zeta) \varphi_j(\zeta) \, d\zeta,$$

$$K_{ij}(t) = \frac{\rho a}{l} \int_0^1 (1-\zeta)\, \varphi_i'(\zeta) \varphi_j(\zeta) \, d\zeta - \frac{\rho v^2}{l^2} \int_0^1 (1-\zeta)^2\, \varphi_i'(\zeta) \varphi_j'(\zeta) \, d\zeta + \frac{\rho g}{l} \int_0^1 (1-\zeta)\, \varphi_i'(\zeta) \varphi_j'(\zeta) \, d\zeta - \frac{mg}{l^2} \int_0^1 \varphi_i''(\zeta) \varphi_j(\zeta) \, d\zeta,$$

$$S_j(\mathbf{Q}) = -\frac{3EA}{2l^4} \int_0^1 \Big(\sum_{i=1}^{n} \varphi_i'(\zeta) q_i(t)\Big)^2 \sum_{i=1}^{n} \varphi_i''(\zeta) q_i(t) \varphi_j(\zeta) \, d\zeta; \quad (21)$$

where the superscript " $'$ " denotes partial differentiation for the normalized variable ζ, and δ_{ij} is the Kronecker delta defined

by $\delta_{ij} = 1$ if $i = j$ and $\delta_{ij} = 0$ if $i \neq j$ ($i = 1, 2, 3, \ldots, n$, $j = 1, 2, 3, \ldots, n$). If the initial displacement and velocity of the string are given by $y(x, 0)$ and $y_t(x, 0)$, respectively, where $0 < x < l(0)$, the initial conditions for the generalized coordinate can be obtained from Eqs. (17) and (19);

$$q_i(0) = \int_0^1 y\left(\zeta l(0), 0\right) \varphi_i(\zeta)\, d\zeta; \tag{22}$$

$$\dot{q}_i(0) = \int_0^1 y_t\left(\zeta l(0), 0\right) \varphi_i(\zeta)\, d\zeta + \frac{v(0)}{l(t)} \sum_{i=1}^{n} q_i(0) \int_0^1 \zeta \varphi_i'(\zeta) \varphi_j(\zeta)\, d\zeta. \tag{23}$$

Solving the ordinary differential Eq. (20) with numerical methods may yield the instantaneous values of $\mathbf{Q}$. Substituting these values into Eq. (17) may yield the instantaneous values of transverse vibration of the string $y(x, t)$. The mathematical model defined by Eq. (20) illustrates the true dynamic nature of the flexible hoisting string, and can be used to predict and analyze the dynamic stability and vibration characteristics of a flexible hoisting string with time-varying length and axial velocity.

4. ANALYSIS OF DYNAMIC STABILITY

In order to gain a deeper insight into the mechanics of the flexible hoisting string with time-varying length and axial velocity, it is beneficial to investigate the stability characteristics of the problem. In what follows, we performed a stability analysis of the flexible hoisting string with time-varying dynamic parameters. According Lyapunov's first method, the stability of the system could be determined by analyzing the eigenvalues of the natural vibration. To obtain the eigenvalues of the flexible hoisting string, the methods suggested by Stylianou were used to reduce the system of governing Eq. (20) to a set of first order differential equations.[29] The set of reduced equations takes the form

$$\mathbf{A}\dot{\mathbf{U}} + \mathbf{B}\mathbf{U} = \mathbf{0}; \tag{24}$$

where $\mathbf{A}$ and $\mathbf{B}$ are matrix differential operators, and

$$\mathbf{A} = \begin{Bmatrix} \mathbf{M} & \mathbf{0} \\ \mathbf{0} & \mathbf{K} \end{Bmatrix}, \qquad \mathbf{B} = \begin{Bmatrix} \mathbf{C} & \mathbf{K} \\ -\mathbf{K} & \mathbf{0} \end{Bmatrix}; \tag{25}$$

$\mathbf{U}$ is the state vector, and

$$\mathbf{U} = \begin{Bmatrix} \dot{\mathbf{Q}} \\ \mathbf{Q} \end{Bmatrix}. \tag{26}$$

Equation (24) is the canonical form of the equation of motion and its solution satisfies the appropriate boundary conditions and initial conditions. Rearranging Eq. (24), we write

$$\dot{\mathbf{U}} + \mathbf{D}\mathbf{U} = \mathbf{0}; \tag{27}$$

where

$$\mathbf{D} = \mathbf{A}^{-1}\mathbf{B} = \begin{Bmatrix} \mathbf{M}^{-1}\mathbf{C} & \mathbf{M}^{-1}\mathbf{K} \\ -\mathbf{I} & \mathbf{0} \end{Bmatrix}. \tag{28}$$

Here, $\mathbf{I}$ is an $n \times n$ identity matrix. To obtain the natural frequencies and mode shapes for the flexible hoisting string with time-varying length, consider the eigenvalue problem of Eq. (27). We now assume that $\mathbf{U}$ is periodic,

$$\mathbf{U} = \mathbf{\Lambda} e^{\boldsymbol{\lambda} t}; \tag{29}$$

where

$$\boldsymbol{\lambda} = \boldsymbol{\xi} + i\boldsymbol{\omega} \tag{30}$$

is the eigenvalue which is a complex number, $\boldsymbol{\xi} = [\xi_1(t), \xi_2(t), \ldots, \xi_k(t)]^T$, $\boldsymbol{\omega} = [\omega_1(t), \omega_2(t), \ldots, \omega_k(t)]^T$ are the real and imaginary parts of $\boldsymbol{\lambda} = [\lambda_1(t), \lambda_2(t), \ldots, \lambda_k(t)]^T$, and $\boldsymbol{\omega}$ is also the natural frequency of the flexible hoisting string. It should be noted that the real and imaginary parts of the eigenvalue are related to the modal damping coefficients and the natrual frequencies of the flexible hoisting string. Substituting Eq. (29) into Eq. (27) leads to an eigenvalue equation

$$\left(\boldsymbol{\lambda}\mathbf{I} + \mathbf{D}\right) \mathbf{\Lambda} = \mathbf{0}; \tag{31}$$

where $\mathbf{\Lambda}$ is the corresponding eigenvector. The eigenvalues can be obtained from

$$\det\left(\boldsymbol{\lambda}\mathbf{I} + \mathbf{D}\right) = 0. \tag{32}$$

When $\boldsymbol{\xi} \leq \mathbf{0}$, the flexible hoisting string is stable, and when $\boldsymbol{\xi} > \mathbf{0}$, the flexible hoisting string is unstable, a positive $\boldsymbol{\xi}$ indicates the instability of the system. The system may lose stability by either divergence (a static form of instability) or flutter (a dynamic form of instability).

The same conclusions can be reached from Lyapunov's second method, which is a mathematical interpretation of the physical property that if a system's total energy is dissipating, then the states of the system will ultimately travel to an equilibrium point. This property can be explored by constructing a scalar, energy-related time-dependent function $T(t)$ for the system, where usually this function $T(t)$ is always positive. If its time derivative $dT(t)/dt < 0$, then the total energy of the system reduces, therefore leading to a stabilized dynamic response. By contrast, if its time derivative $dT(t)/dt > 0$, the total energy of the system increases, thus resulting in an unstabilized dynamic response. So the choice of the appropriate Lyapunov candidate function $T(t)$ is very important. From Eqs. (5) and (6), we observed that the total energy associated with the transverse vibration of the flexible hoisting system is always positive. Hence, the Lyapunov candidate function is given as

$$T(t) = \frac{1}{2} m y_t^2(l(t), t) + \frac{1}{2}\rho \int_0^{l(t)} \left(y_t + v y_x\right)^2 dx + \frac{1}{2} \int_0^{l(t)} \left(P y_x^2 + \frac{1}{4} E A y_x^4\right)^2 dx; \tag{33}$$

where $P(x, t)$ and $y(x, t)$ have been previously defined in Eqs. (7) and (17), respectively. Obviously, $T(t)$ is always positive. Differentiating $T(t)$ in Eq. (34) using Leibnitz's rule

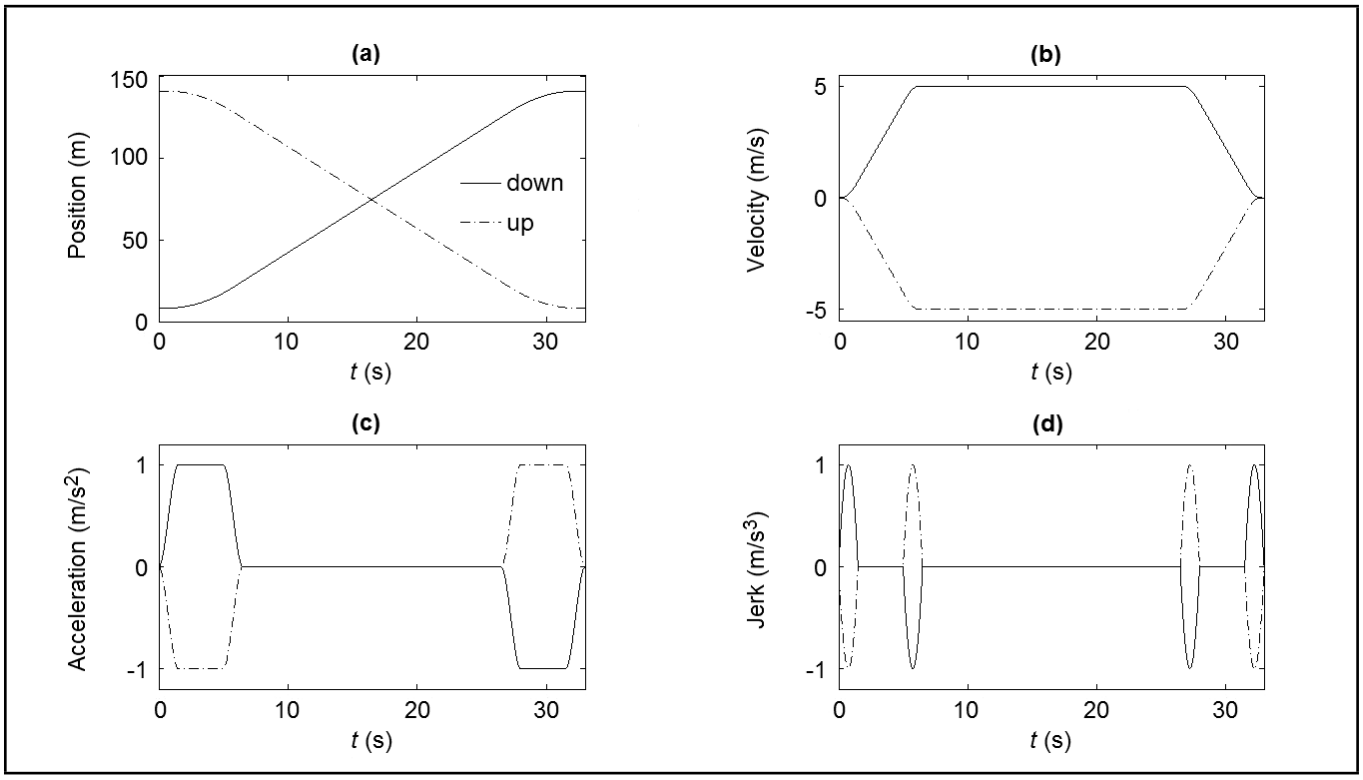

Figure 3. Movement profile of the elevator: (a) $l(t)$; (b) $v(t)$; (c) $\dot{v}(t)$; and (d) $\ddot{v}(t)$.

yields

$$\frac{dT(t)}{dt} = m y_t(l(t),t) y_{tt}(l(t),t) + \frac{1}{2} v \left[\rho (y_t + v y_x)^2 + \left(P y_x^2 + \frac{1}{4} E A y_x^4 \right) \right]_{l(t)} + \int_0^{l(t)} \left[\rho (y_t + v y_x)(y_{tt} + \dot{v} y_x + v y_{xt}) + \frac{1}{2} P_t y_x^2 + P y_x y_{xt} + E A y_x^3 y_{xt} \right] dx. \quad (34)$$

Substituting Eq. (16) into Eq. (34), followed by integration by parts, yields

$$\frac{dT(t)}{dt} = -\frac{\rho v^3}{2} \left(y_x^2 \right)_0^{l(t)} - \frac{v}{2} \left(P y_x^2 \right)_0 + \frac{1}{2} \int_0^{l(t)} \left(P_t + v P_x \right) y_x^2 \, dx + \frac{vEA}{2} \left(w_x^4 \right)_{l(t)} - \frac{3vEA}{8} \left(w_x^4 \right)_0 . \quad (35)$$

5. NUMERICAL SIMULATION AND DISCUSSIONS

A typical application of a flexible hoisting string with time-varying length is a traction elevator. The site observation revealed that traction ropes will fiercely vibrate during movement of the elevator. In what follows, the motions of elevator hoisting system were illustrated to evaluate the proposed mathematical models. An elevator hoisting system is modeled as an axially translating string with a rigid body attached at its lower end. In this paper, the flexible hoisting system of a typical high-speed elevator is considered as an example and analyzed.

Table 1. Simulation parameters.

Items	Data values
Density per unit length ρ (kg/m)	0.707
Young's modulus E (Pa)	2.01×10^{11}
String diameter d (m)	14×10^{-3}
Hoisting mass m (kg)	300
Minimum length of the string $l_{\min}$ (m)	5
Maximum length of the string $l_{\max}$ (m)	140
Maximum velocity $v_{\max}$ (m/s)	5
Maximum acceleration $a_{\max}$ (m/s^2)	1
Maximum jerk $j_{\max}$ (m/s^3)	1
Total travel time t (s)	33
Number of transverse modes n	4

The simulation parameters for the elevator are given in Table 1. The flight time for a travel distance of 135 m (45 stories) is 33 seconds. Figure 3 gives the prescribed displacement, velocity, acceleration and jerk curves of an elevator hoisting system. Utilizing the curves as the input of Eqs. (20), (32), and (35) with the aid of MATLAB® may obtain dynamic responses of an elevator hoisting system. In this work, all numerical analyses were implemented with the aid of MATLAB®.

Consider the free vibration caused by a distributed initial displacement and released from rest. The initial displacement and velocity are respectively

$$y(x,0) = y_0 \sin \frac{x\pi}{l_0}, \qquad y_t(x,0) = 0; \quad (36)$$

where $y_0 = 0.005$ m is the initial amplitude. Transverse vibration responses of the flexible hoisting string at 3 m above the car during movement of the elevator are illustrated in Fig. 4.

Figures 4(a) and 4(b) display reducing vibration amplitudes with an increasing length of the string during downward movement. This is due to the energy of the flexible hoisting sys-

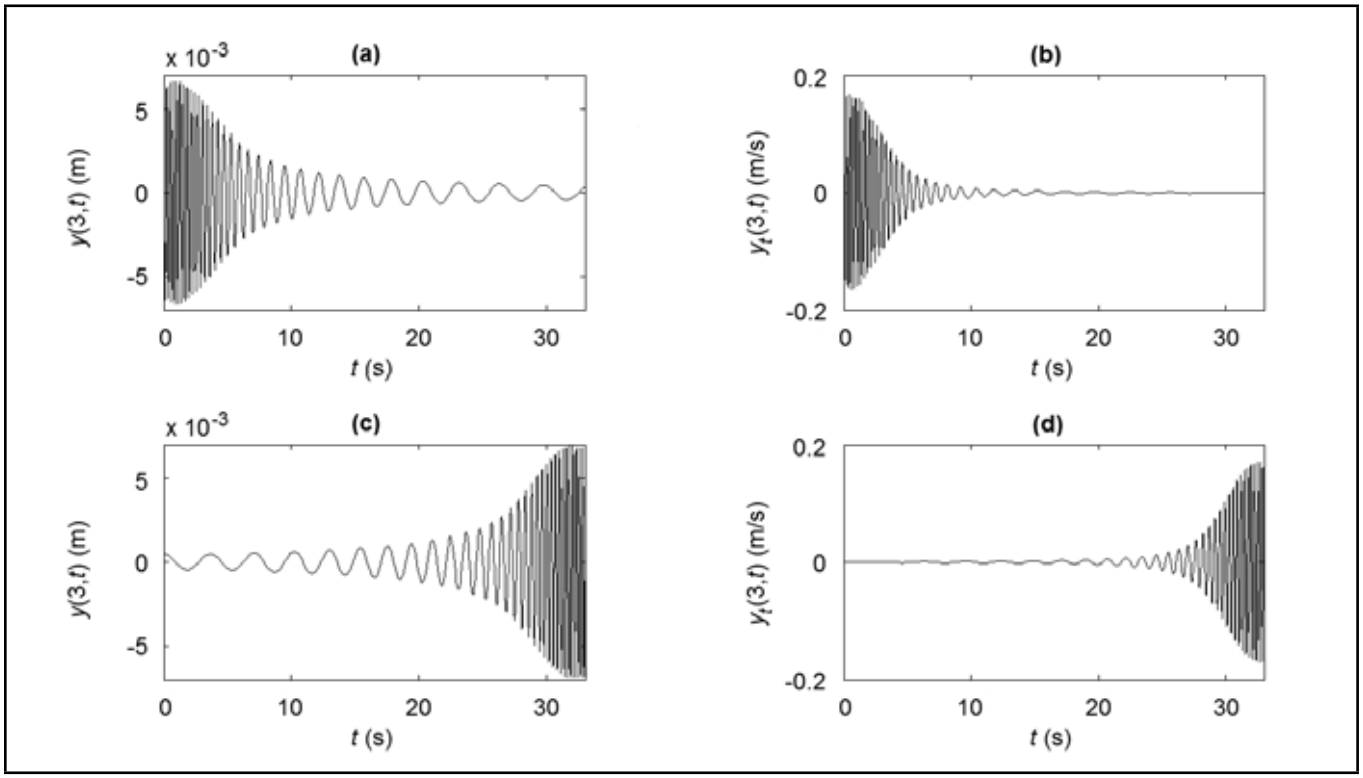

Figure 4. Transverse vibration responses of the flexible hoisting string at 3 m above the car: (a) Transverse vibration displacement during downward movement of the elevator; (b) Transverse vibration velocity during downward movement of the elevator; (c) Transverse vibration displacement during upward movement of the elevator; and (d) Transverse vibration velocity during upward movement of the elevator.

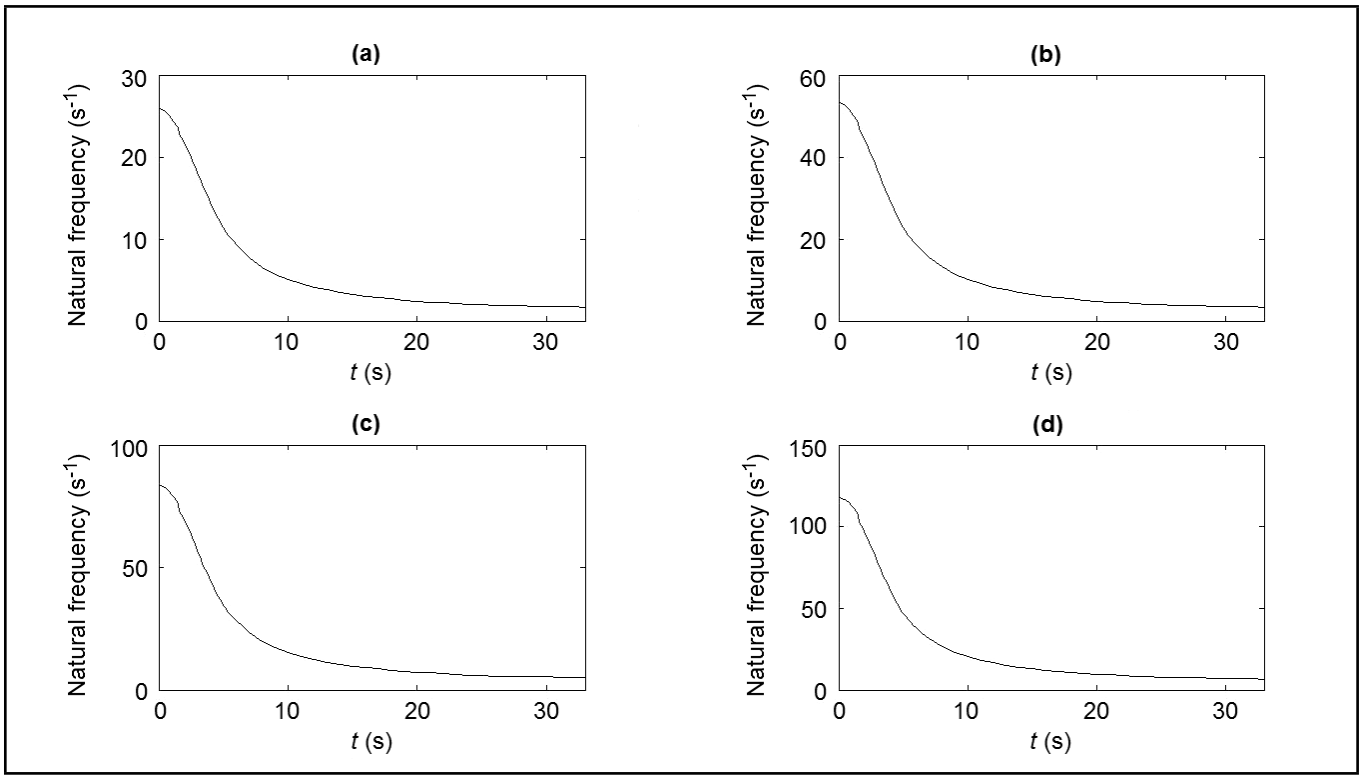

Figure 5. The lowest four order natural frequencies of the flexible hoisting string during downward movement of the elevator: (a) First order natural frequency; (b) Second order natural frequency; (c) Third order natural frequency; and (d) Fourth order natural frequency.

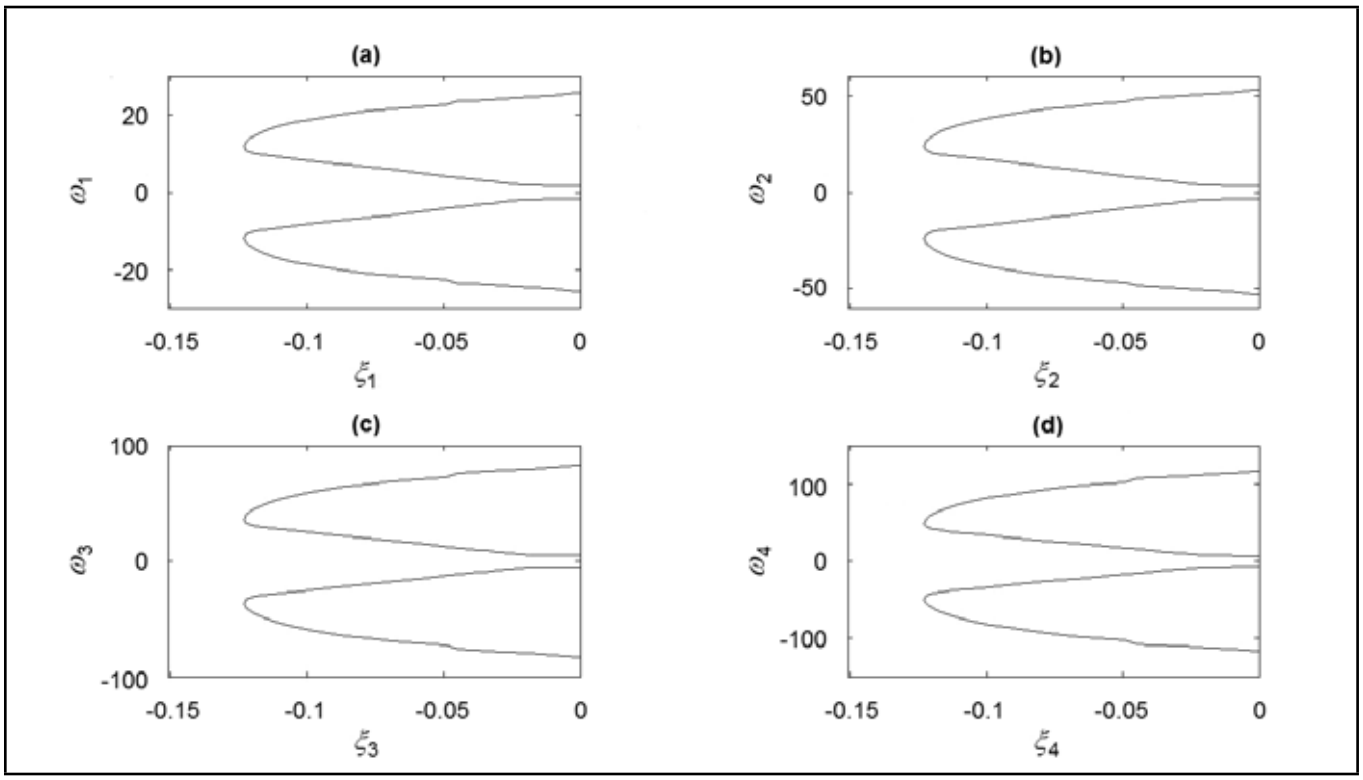

Figure 6. Eigenvalues of the flexible hoisting string during downward movement of the elevator: (a) λ_1; (b) λ_2; (c) λ_3; and (d) λ_4.

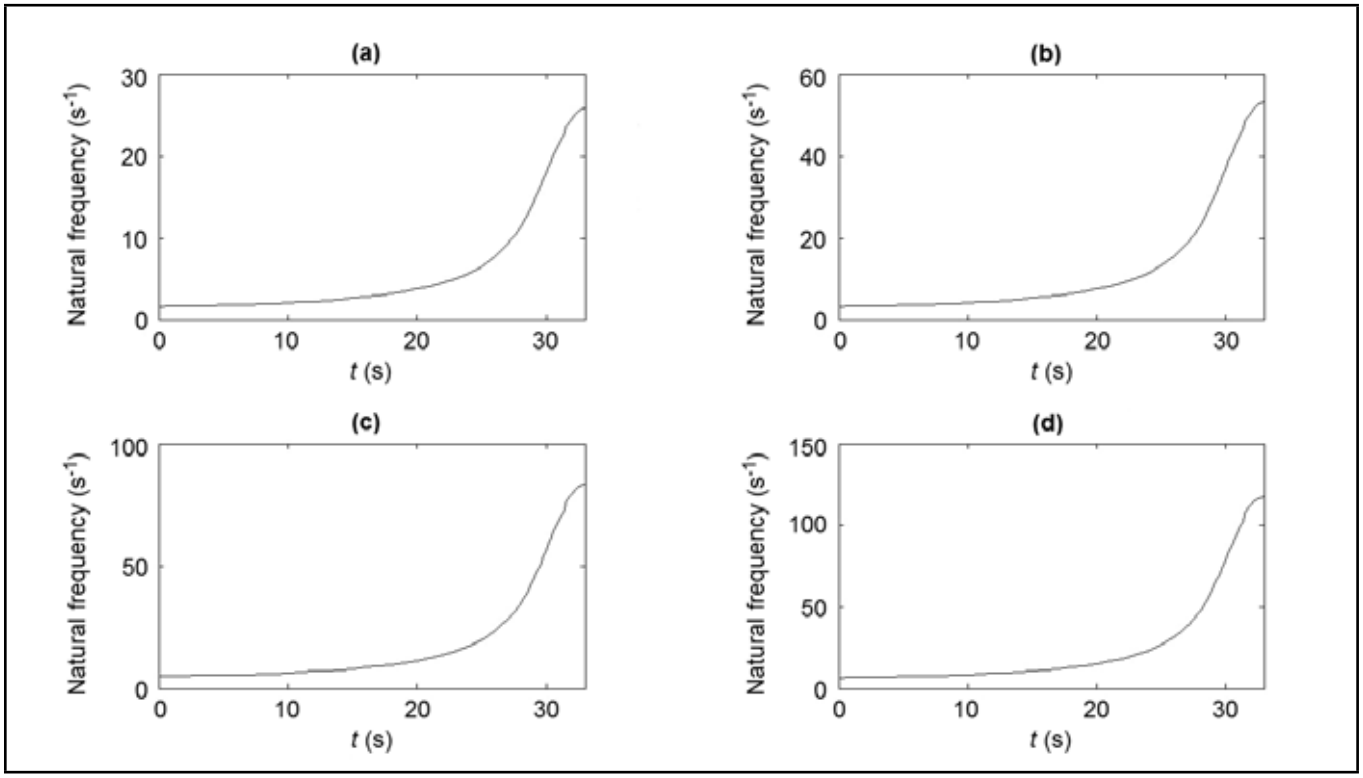

Figure 7. The lowest four order natural frequencies of the flexible hoisting string during upward movement of the elevator: (a) First order natural frequency; (b) Second order natural frequency; (c) Third order natural frequency; and (d) Fourth order natural frequency.

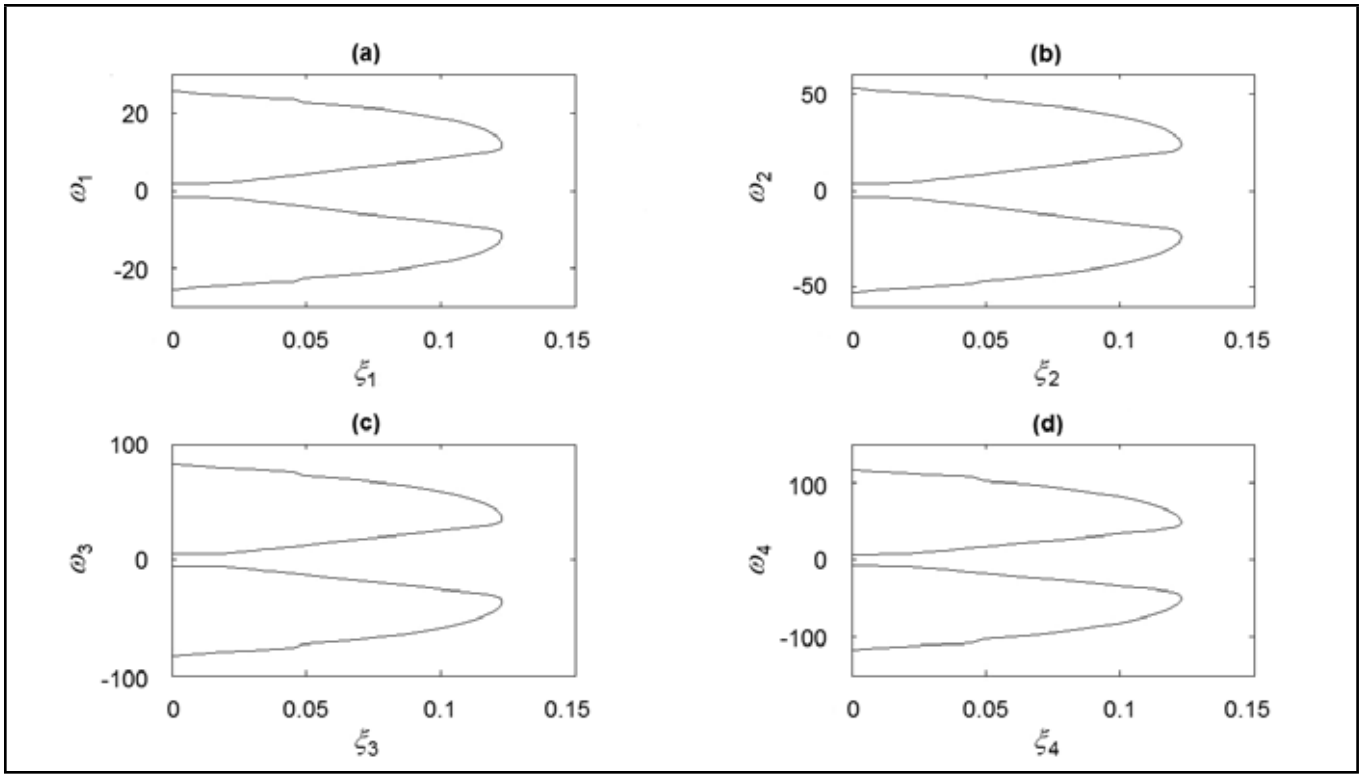

Figure 8. Eigenvalues of the flexible hoisting string during upward movement of the elevator: (a) λ_1; (b) λ_2; (c) λ_3; and (d) λ_4.

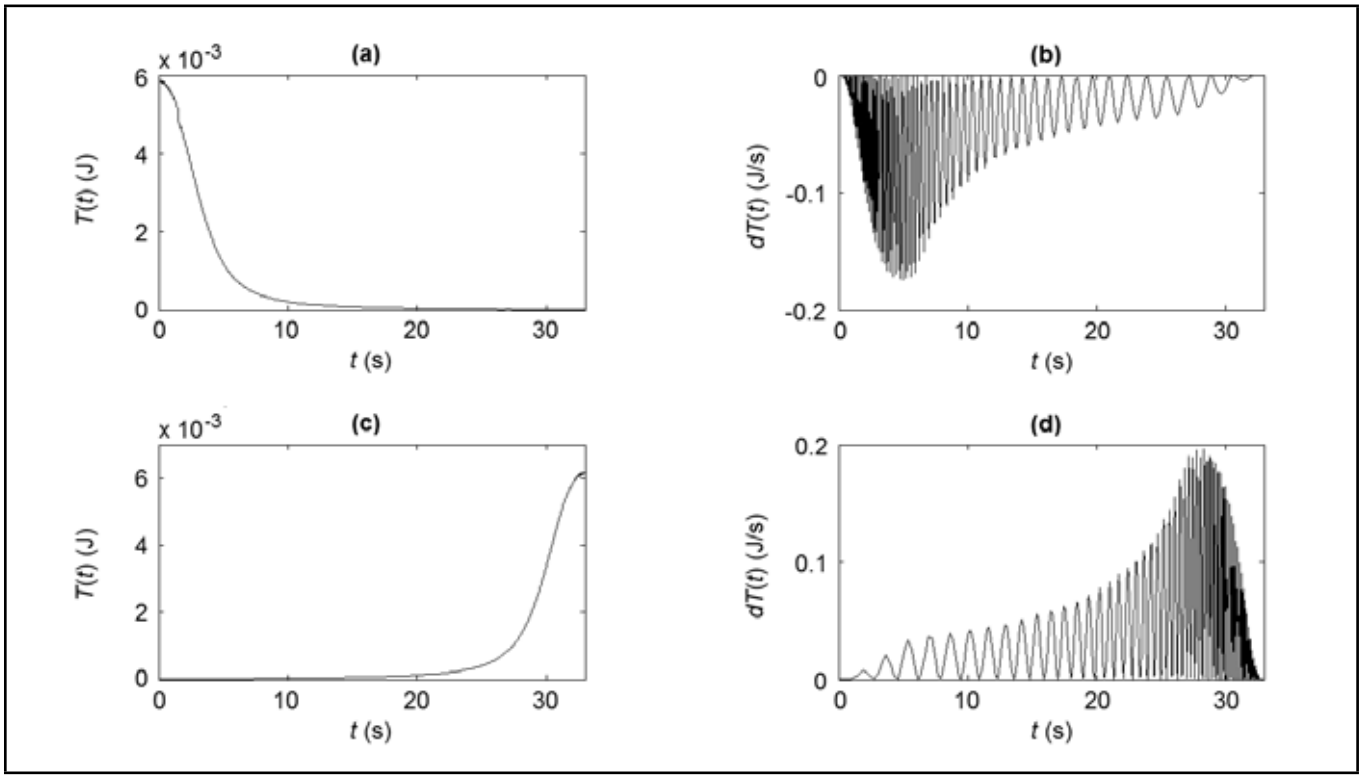

Figure 9. The transverse vibration energy and the rate of change of the energy: (a) The transverse vibration energy during downward movement; (b) The rate of change of the energy during downward movement; (c) The transverse vibration energy during upward movement; and (d) The rate of change of the energy during upward movement.

tem transfers from the transverse vibration to the axial motion by bringing some mass into the domain of effective length, which means that the axially moving string is dissipative during downward movement. A possible physical interpretation of the results is as follows: during downward movement negative external work is required to maintain the prescribed axial motion which, in turn, brings about a convection of mass in the domain of effective length. By contrast, in Fig. 4(c) and Fig. 4(d), we observe that vibration amplitudes of the string increase with the decreasing length of the string during upward movement. This is due to the energy of flexible hoisting system transfers from the axial motion to the transverse vibration by leaving some mass out of the domain of effective length, which means that the axially moving string gains energy during upward movement. A possible physical interpretation of the results is as follows: during upward movement positive external work is required to maintain the prescribed axial motion which, in turn, brings about a convection of mass out of the domain of effective length.

For the stabilization analysis of the flexible hoisting string, the eigenvalues of the system obtained from Eq. (32) should be studied for further consideration. During downward movement of the flexible hoisting system, the mass of the string is increasing and the stiffness of the string is reducing, or the string becomes somewhat stiffer, and the natural frequencies will decrease over time, which has been displayed in Fig. 5. In the mean time, the dynamic motion of the string is stable as the eigenvalues of this system have negative real parts ξ; (see Fig. 6). On the other hand, during upward movement of the flexible hoisting system, the mass of the string is decreasing and the stiffness of the string is increasing, or the string becomes somewhat stiffer, and the natural frequencies will increase with time, (see Fig. 7). At the same time, the dynamic motion of the string is unstable since the real parts ξ of eigenvalues of this system are all positive, which has been shown in Fig. 8. That is, the coupling effect of the translation and transverse motions generates a stabilizing response during downward movement of the flexible hoisting system and a destabilization response during upward movement of the flexible hoisting string. The same conclusions can be reached from the investigation based on an energy standpoint.

The resulting total transverse vibration energy and the rate of change of the energy of the flexible hoisting system are displayed in Fig. 9. During downward movement of the flexible hoisting system, the energy associated with the transverse vibration of the flexible hoisting system decreases, which has been displayed in Fig. 9(a). The reduction of transverse vibration energy translates into the increase in kinetic energy of the flexible hoisting system. In the mean time, the rate of change of the energy $dT(t)/dt$ is negative (see Fig. 9(b)), thus leading to a stabilized transverse dynamic response. By contrast, during upward movement of the flexible hoisting system, the transverse vibration energy of the flexible hoisting system increases, which has been shown in Fig. 9(c). The increase of transverse vibration energy comes from the reduction in kinetic energy of the flexible hoisting system. At the same time, the rate of change of the energy $dT(t)/dt$ is positive (see Fig. 9(d)), therefore resulting in an unstabilized transverse dynamic response. The results explain an inherent unstable shortening cable behavior encountered in the elevator industry.

6. CONCLUSIONS

The linear vibration characteristics and stability for a flexible hoisting string with time-varying length and axial velocity considering coupling of axial movement and flexural deformation were analyzed in this paper. The flexible hoisting system was modeled as an axially moving string with time-varying length and a rigid body at its lower end. The governing equations were derived by using Leibnitz's rule and the extended Hamilton's principle. The Galerkin's method was used to truncate the infinite-dimensional partial differential equations into a set of nonlinear finite-dimensional ordinary differential equations with time-variant coefficients. Based on the numerical simulations, the following conclusions can be obtained:

1. Two different methods, Lyapunov's first method and Lyapunov's second method were used to analyze the stability of the flexible hoisting string with time-varying length and axial velocity. The same results were obtained by the two mehtods.

2. The flexible hoisting string with time-varying length and axial velocity experiences instability during upward movement; the natural frequencies increase because of the reducing mass and the increasing stiffness of the string; and the energy transforms from the axial movement into the flexible deformation. By contrast, it is stable during downward movement; the natural frequencies decrease because of the increasing mass and the reducing stiffness of the string; and the energy coverts from the flexible deformation into the axial movement.

3. The proposed theoretical model and analyses about the stability of the flexible hoisting system in this paper will be helpful for the researchers to comprehend its dynamic behavior and develop the proper method to suppress the vibration in practice.

ACKNOWLEDGEMENTS

This work was supported by the National Natural Science Foundation of China (Grant No: 51205249). The authors are also most grateful to the anonymous reviewers and the Editor for their constructive comments.

REFERENCES

[1] Kaczmarczyk, S. and Ostachowicz, W. Non-stationary responses of cables with slowly varying length, *International Journal of Acoustics and Vibration*, **5** (3), 1–10, (2000).

[2] Chen, Y. F. and Huang, A. C. Oscillation reduction for overhead cranes with time-varying payload and rope length, *Journal of the Chinese Institute of Engineers*, **36** (2), 1–9, (2013).

[3] Kimura, H., Ito, H., and Nakagawa, T. Vibration analysis of elevator rope (2nd report, forced vibration of rope with damping), *Journal of System Design and Dynamics*, **2** (2), 540–549, (2008).

[4] Kimura, H., Iijima, T., Matsuo, S., and Yoshiaki, F. Vibration analysis of elevator rope (Comparison between experimental results and calculated results), *Journal of System Design and Dynamics*, **3** (3), 420–428, (2009).

[5] Zhang, P., Zhu, C. M., and Zhang, L. J. Analysis of forced coupled longitudinal-transverse vibration of flexible hoisting systems with varying length, *Engineering Mechanics*, **25** (12), 202–207, (2008).

[6] Wang, L. H., Hu, Z. H., Zhong, Z., and Ju, J. W. Dynamic analysis of an axially translating viscoelastic beam with an arbitrarily varying length, *Acta Mechanica*, **214** (3–4), 225–244, (2010).

[7] Wang, L. H., Hu, Z. H., and Zhong, Z. Dynamic analysis of an axially translating plate with time-variant length, *Acta Mechanica*, **215** (1–4), 9–23, (2010).

[8] Zhang, P., Zhu C. M., and Zhang, L. J. Analyses of longitudinal vibration and energetic on flexible hoisting systems with arbitrarily varying length, *Journal of Shanghai Jiaotong University*, **42** (3), 481–488, (2008).

[9] Zhang, P., Zhu, C. M., and Zhang, L. J. Coupled longitudinal-transverse vibration of flexible elevator rope, *Proc. the Symposium on the Mechanics of Slender Structures (MoSS2008)*, Baltimore, USA, (2008).

[10] Zhang, P., Zhu, C. M., Bao, J. H., and Zhang, L. J. Horizontal vibration of car in the flexible suspension system of elevator, *Proc. the Symposium on the Mechanics of Slender Structures (MoSS2010)*, San Sebastian, Spain, (2010).

[11] Zhang, P., Bao, J. H., and Zhu, C. M. Dynamic analysis of hoisting viscous damping string with time-varying length, *Journal of Physics: Conference Series*, **488** (1), 1–9, (2013).

[12] Bao, J. H., Zhang, P., and Zhu, C. M. Modeling and analysis of rope transverse vibration for flexible hoisting systems with time-varying length, *Journal of Shanghai Jiaotong University*, **46** (3), 341–345, (2012).

[13] Bao, J. H., Zhang, P., and Zhu, C. M. Computing simulation and dynamics modeling of flexible hoisting rope with time-varying length, *Journal of Computer Information Systems*, **8** (10), 4177–4184, (2012).

[14] Terumichi, Y., Ohtsuka, M., Yoshizawa, M., Fukawa, Y., and Tsujioka, Y. Nonstationary vibrations of a string with time-varying length and a mass-spring system attached at the lower end, *Nonlinear Dynamics*, **12**, 39–55, (1997).

[15] Zhu, W. D. and Chen, Y. Theoretical and experimental investigation of elevator cable dynamics and control, *Journal of Vibration and Acoustics*, **128**, 66–78, (2006).

[16] Chen Y. On the longitudinal vibration of a moving elevator cable-car system, Master Thesis, Faculty of Mechanical Engineering, University of Maryland Baltimore County, USA, (2008).

[17] Nguyen, Q. C. and Hong, K. S. Transverse vibration control of axially moving membranes by regulation of axial velocity, *IEEE Transactions on Control Systems Technology*, **20** (4), 1124–1131, (2012).

[18] Ngo, Q. H., Hong, K. S., and Jung, I. H. Adaptive control of an axially moving system, *Journal of Mechanical Science and Technology*, **23**, 3071–3078, (2009).

[19] Fung, R. F. and Lin, J. H. Vibration analysis and suppression control of an elevator string actuated by a PM synchronous servo motor, *Journal of Sound and Vibration*, **206** (3), 399–423, (1997).

[20] Chi, R. M. and Shu, H. T. Longitudinal vibration of a hoist rope coupled with the vertical of an elevator car, *Journal of Sound and Vibration*, **148** (1), 154–159, (1991).

[21] Zhang, Y. H. Longitudinal vibration modeling and control a flexible transporter system with arbitrarily varying cable lengths, *Journal of Vibration and Control*, **11**, 431–456, (2005).

[22] Kaczmarczyk, S. and Ostachowicz, W. Transient vibration phenomena in deep mine hoisting cables. Part 2: Numerical simulation of the dynamic response, *Journal of Sound and Vibration*, **262**, 245–289, (2003).

[23] Zhang, Y. H. and Agrawal, S. Coupled vibrations of a varying length flexible cable transporter system with arbitrary axial velocity, *Proc. the 2004 American Control Conference*, Boston, MA, USA, (2004).

[24] Lee, S. Y. and Lee, M. A new wave technique for free vibration of a string with time-varying length, *Journal of Applied Mechanics*, **69**, 83–87, (2002).

[25] Kumaniecka, A. and Niziol, J. Dynamic stability of a rope with slow variability of the parameters, *Journal of Sound and Vibration*, **178**, 211–226, (1994).

[26] Zhu, W. D. and Ni, J. Energetics and stability of translating media with an arbitrarily varying length, *Journal of Vibration and Acoustics*, **122** (7), 295–304, (2000).

[27] Lu, Y. F. *Flexible Multi-body Dynamics*, China Higher Education Press, (1996).

[28] Liu, H. W. *Mechanics of Materials*, China Higher Education Press, (1992), 3rd ed., Vol. 2.

[29] Stylianou, M. and Tabarrok, B. Finite element analysis of an axially moving beam, part II: stability analysis, *Journal of Sound and Vibration*, **178** (4), 455–481, (1994).

Active Sway Control of a Gantry Crane by an Electrical Ducted Fan

Mohammad Javad Maghsoudi and Z. Mohamed

Faculty of Electrical Engineering, Universiti Teknologi Malaysia, 81310 UTM Johor Bahru, Johor, Malaysia

(Received 4 June 2013; accepted 23 May 2014)

Sway reduction is very vital in a nonlinear oscillatory system such as a gantry crane. In this paper, a new design is proposed for active sway control of a gantry crane using an electrical ducted fan. The thrust force developed by the motor is used to cancel out payload oscillation. A dynamic model of the crane with a ducted fan is derived and simulated using Matlab. Performance of the proposed technique is investigated for a crane subjected to initial sway and an external force input. In addition, cases with different payloads and cable lengths are also studied. Simulation results show satisfactory performance of the fan-controlled system in eliminating the payload sway. The proposed design can also handle changes in payload and cable length. A main advantage of this approach is that it does not require modeling of the crane in real time experiments.

1. INTRODUCTION

Vibration control is crucial in flexible structures where their movement produces undesired vibration. Although flexible systems are lighter and faster than rigid ones, their motion-induced vibration is a drawback that limits their applications. In order to reduce the system vibration, several control approaches have been proposed by researchers. These include, active control of a grinding machine,[1] adaptive control of a drill string,[2] active vibration control of a ring-stiffened cylindrical shell[3] and active vibration control of smart plates.[4]

Gantry cranes are flexible structures that are commonly used in material handling systems in factories, warehouse, shipping yards, and nuclear facilities where heavy loads must be transferred from a specific place to a desired location. However, the crane movement induces undesirable payload sway.[5] This undesired load swing negatively influences the productivity and causes a drop in efficiency, load damages, and even accidents. Speed is a focal point in industries as it translates into the productivity and efficiency of the system. However, fast maneuvers tend to excite sway angles of the hoisting line, and this can result in a higher residual sway that degrades the overall performance. At very low speeds, the payload sway is not important and can be ignored. Nevertheless, at a higher speed, these sway angles become larger and significant and cause the payload difficulty in settling down when unloading. The overall system performance will be affected when significant sway angle of the payload occurs during and after the movement of a gantry crane. This is a very severe problem, especially for applications in the industries that require high positioning accuracy, small swing angle, short transportation time, and high safety.[6]

A number of techniques have been proposed for control of gantry cranes. The control objective is to move the trolley to a required position as fast as possible with low payload oscillation. The control algorithms can be categorized into feed-forward and feedback control strategies. The feed-forward control strategy mainly involves command shaping techniques and optimal control. An approach in command shaping techniques known as input shaping has been proposed and has received considerable attention in vibration control.[7] An input shaping technique for reduction of the residual vibration of a gantry crane has also been proposed.[8,9] The closed-loop control algorithms include linear quadratic regulator (LQR) technique, state feedback, and nonlinear control. The LQR technique is utilized to track the reference trajectories,[10] the state feedback control strategy is used to hoist, stabilize, and delivery the payload[11] and a nonlinear control scheme incorporating parameter adaptive mechanism is utilized to ensure the overall close-loop system stability[6] have been proposed by researchers. On the other hand, an acceptable system performance without payload sway that accounts for system changes by developing a hybrid controller consisting of both feed-forward and feedback control techniques has been successfully implemented on a gantry crane.[12]

Although many control strategies have been applied on different type of cranes to reduce the payload sway, no work has been conducted on the direct control of the payload sway. Several researchers have used ducted fans to control the swinging payloads, such as spy cameras[13] and indoor service robots.[14] In this paper, a new sway control strategy is proposed that utilizes an electrical ducted fan to directly control the payload sway of a gantry crane. The thrust force of an electrical ducted fan, installed on top of the hook, can be used to significantly reduce residual sway. The proposed technique can handle initial sway, external disturbances and changes in payloads and cable lengths.

2. DYNAMIC MODEL OF A GANTRY CRANE

The gantry crane can be considered as a simple cart and pendulum system.[12] Figure 1 shows a schematic diagram of a trolley and payload system considered in this study. M, m, l, b, d, F_e, x, and θ represent trolley mass, payload mass, cable length, coefficient of payload friction, coefficient of trolley friction, external force, trolley displacement, and angular displacement of payload, respectively. Table 1 shows the system parameters used in these investigations.

There are several methods to derive the mathematical equations that represent the trolley and payload system. In this work, Lagrange's equation is used to derive the mathematical expression for the model. The system has two numbers of independent generalized coordinate, namely trolley displacement x and angular displacement of payload oscillation. The

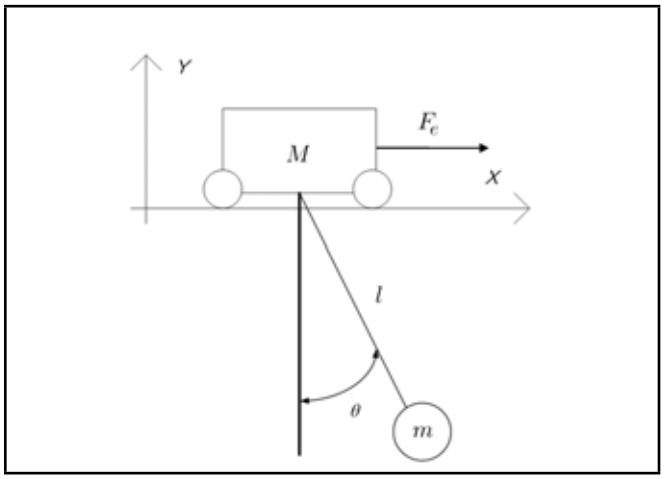

Figure 1. Schematic diagram of a gantry crane.

Table 1. System Parameters.

Variables	Values
mass of troley, M	1 kg
mass of payload, m	1.1 kg
gravitational constant, g (m)	9.8 m/s^2
trolley friction constant, d	20 Ns/m
constant of payload friction, b	0.001 Ns/m
length of cable, l	0.45 m

standard form for Lagrange's equation is given as

$$\frac{d}{dt}\left[\frac{\partial L}{\partial \dot{q}_i}\right] - \frac{\partial L}{\partial q_i} = Q_i; \tag{1}$$

where L, Q_i and q_i represent Lagrangian function, non-conservative generalized forces, and independent generalized coordinate. The Lagrangian function can be written as:

$$L = T - V; \tag{2}$$

where T and V are kinetic and potential energies, respectively. Therefore, the Lagrangian function can be obtained as:

$$L = \frac{1}{2}\left(m\dot{x}^2 + M\dot{x}^2 + ml^2\dot{\theta}^2\right) + m\dot{x}\dot{\theta}l\cos\theta + mgl\cos\theta. \tag{3}$$

Analyzing Eq. (3) yields:

$$\frac{\partial L}{\partial \dot{x}} = m\dot{x} + M\dot{x} + ml\dot{\theta}\cos\theta; \tag{4}$$

$$\frac{d}{dt}\left[\frac{\partial L}{\partial \dot{x}}\right] = m\ddot{x} + M\ddot{x} - ml\dot{\theta}^2\sin\theta + ml\ddot{\theta}\cos\theta; \tag{5}$$

$$\frac{\partial L}{\partial \dot{\theta}} = ml^2\dot{\theta} + m\dot{x}l\cos\theta; \tag{6}$$

$$\frac{d}{dt}\left[\frac{\partial L}{\partial \dot{\theta}}\right] = ml^2\ddot{\theta} + m\dot{x}l\dot{\theta}\sin\theta + m\ddot{x}l\cos\theta. \tag{7}$$

Utilizing Eqs. (4) to (7) and Eq. (1) yields nonlinear differential equations of the system as:

$$(m+M)\ddot{x} + ml\ddot{\theta}\cos\theta - ml\dot{\theta}^2\sin\theta - d\dot{x} = F_e; \tag{8}$$

$$ml^2\ddot{\theta} + ml\ddot{x}\cos\theta + mgl\sin\theta + b\dot{\theta} = 0. \tag{9}$$

In Matlab Simulink, the nonlinear equations are modeled as a single input multi output (SIMO) system and the model will be used for controller design and verification.

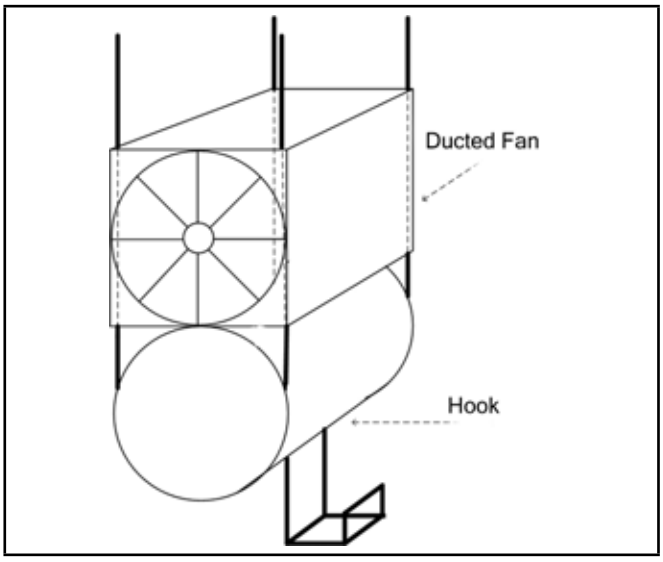

Figure 2. An electrical ducted fan installed on top of the hook.

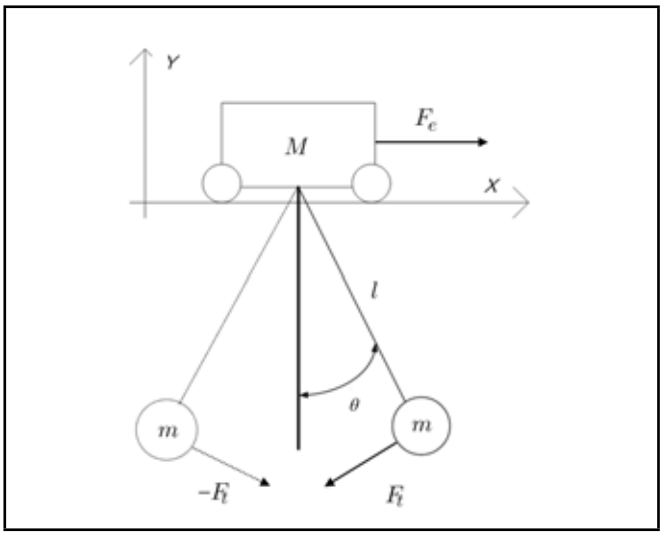

Figure 3. Schematic diagram of the gantry crane with fan.

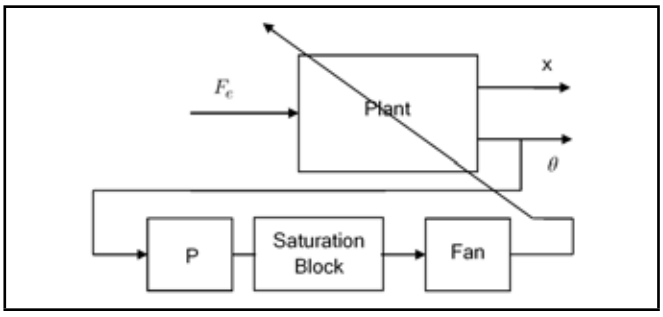

Figure 4. Fan control scheme.

3. FAN CONTROLLED SYSTEM

The gantry crane system is modeled using nonlinear equations as in Eqs. (8) and (9). Although this model is simply utilized for numerical simulation, finding an accurate model that gives similar behavior as the real system is usually very difficult. Model uncertainty can cause serious problems in terms of system performance and stability in real systems. Moreover, applying an external force to a nonlinear gantry crane system produces a considerable amount of sway in the transient and

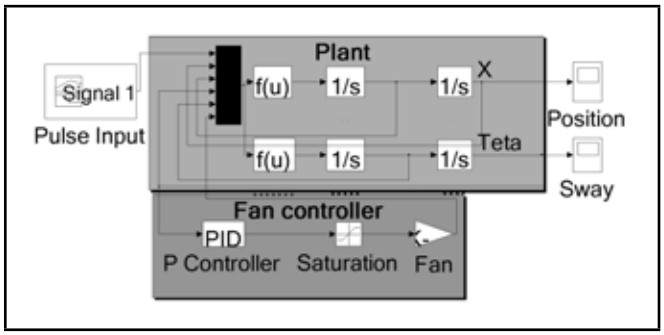

Figure 5. Simulation of the fan control scheme.

steady states of the system. As this payload sway is the most important specification in control objective, having an intelligent payload that can eliminate the sway actively is beneficial.

In this work, a payload equipped with an electrical ducted fan as an active controller is proposed. As shown in Fig. 2, the fan is installed on top of the hook. Most of the industrial gantry cranes are equipped with four strong cables to hoist the load. The fan can be installed in such a way that these cables support the fan and keep the fan parallel to the hook in order to prevent it from undesirable rotation. Moreover, hoisting is considered where the cable length can be reduced or increased to move in vertical directions. For this reason, these cables are designed to pass through four holes in the frame of the fan. The schematic diagram of the system including the fan is shown in Fig. 3. The thrust force (F_t) of the fan is able to move the payload to the left and right intelligently. The payload oscillation can be cancelled by applying the thrust force as in Eq. (10).

$$ml\ddot{\theta} + m\ddot{x}\cos\theta + mg\sin\theta + (b/l)th\dot{e}ta = -F_t. \quad (10)$$

It is assumed that F_t acts similar to the air friction force of the payload. The hook and fan are considered as a lumped mass. As shown in Fig. 3, when the payload moves to right side, F_t will react in the opposite direction to cancel the sway. Similarly, when the payload moves to left side, F_t will also react in the opposite direction. This can be done by changing the rotation direction of the fan using its motor driver.

Figure 4 shows the control system of a fan that consists of an encoder to measure the sway angle θ, a proportional controller to command the driver of the fan, a saturator to limit the input of the driver, and a driver to change the direction and voltage level of fan. An AC or DC fan motor compatible with the specific design can be used. The closed-loop controller of the fan tries to keep θ near zero continuously. In other words, any oscillation regardless of its source, whether it is caused by the crane's movement or by the wind—can be cancelled in the right or left direction. The proposed approach may be feasible using a new carbon made electrical turbo fan weighing 0.12 kg with a diameter of only 0.12 m that can produce thrust of 40 N.[15] It should be mentioned that as the fan controller is independent of the crane controller, other methods, such as input shaping or closed loop controllers, can be used in parallel for the cases where the load is too heavy compared to the fan thrust.

4. SIMULATION RESULTS AND DISCUSSION

In this section, the control scheme is implemented and tested within the simulation environments, and the corresponding results are presented. A personal computer with Intel Core2 Duo CPU, 2.1 GHz clock frequency and Simulink was utilized for simulation of the controller. Based on the system illustrated in Fig. 5), two functions correspond to position and sway of the model:

$$\ddot{x} = \frac{ml\dot{\theta}^2\sin\theta + mg\sin\theta\cos\theta - d\dot{x}}{M + m\sin^2\theta} + \frac{b/l\ \dot{\theta}\cos\theta + F_t\cos\theta - F_e}{M + m\sin^2\theta} \quad (11)$$

$$\ddot{\theta} = \frac{-ml\dot{\theta}^2\sin\theta\cos\theta - (m+M)g\sin\theta + d\dot{x}\cos\theta}{l(M + m\sin^2\theta)} + \frac{-(1+M/m)(b/l\ \dot{\theta} + F_t) + F_e\cos\theta}{l(M + m\sin^2\theta)} \quad (12)$$

In this experiment, the proportional controller with a gain of 20 is used. The fan is considered as a linear voltage to force convertor with a coefficient of 4. Moreover, maximum and minimum saturation limits are set to +10 volt and -10 volts, respectively.

In the first experiment, the performance of the active sway controller to an initial existing sway was investigated. Thus, a condition with no external input ($F_e = 0$) and initial existing sway ($\theta = 0.3$ rad) was considered. Figures 6 and 7 show simulation results of the payload sway and trolley position response respectively, both without and with a fan-controlled

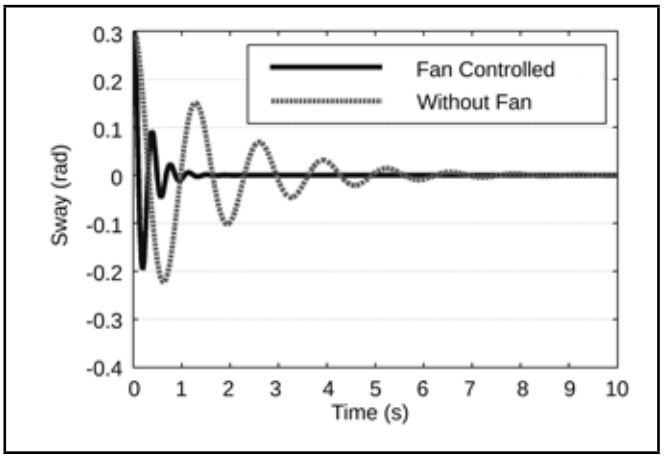

Figure 6. Sway of payload (initial $\theta = 0.3$ rad).

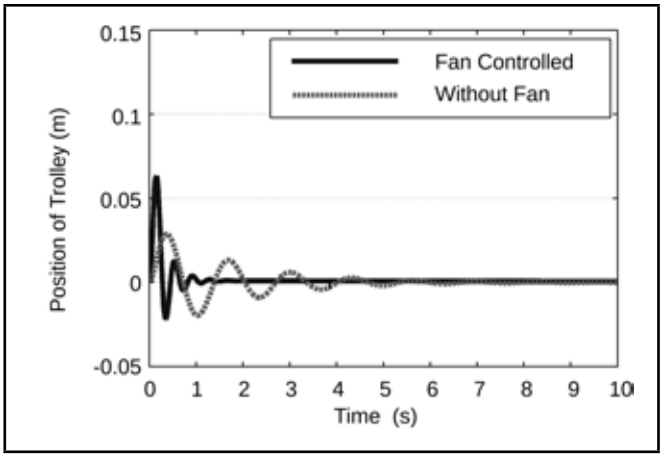

Figure 7. Position response of the trolley (initial $\theta = 0.3$ rad).

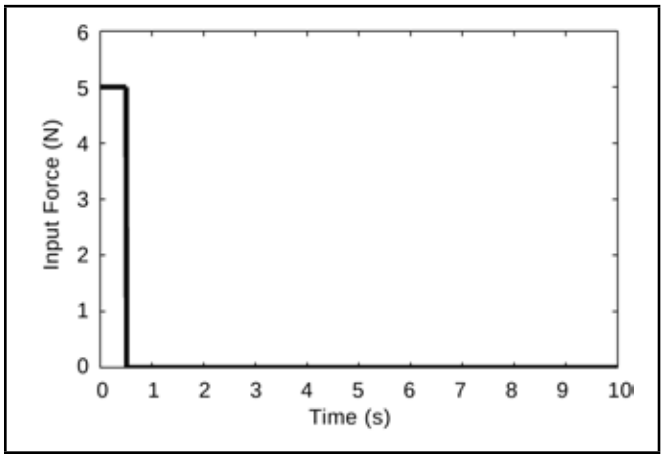

Figure 8. Force Input to the system.

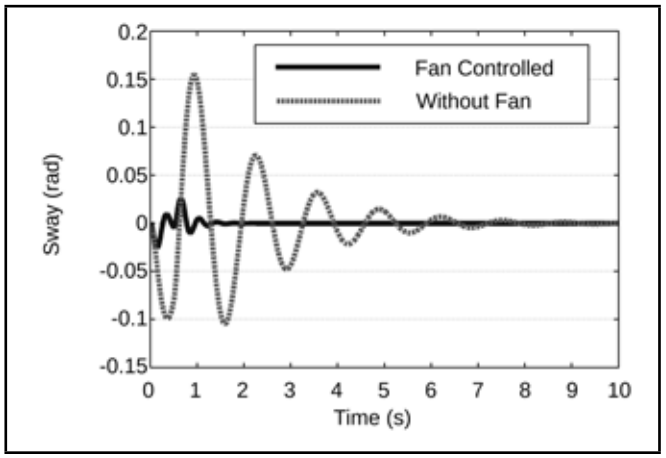

Figure 10. Sway of payload (pulse input).

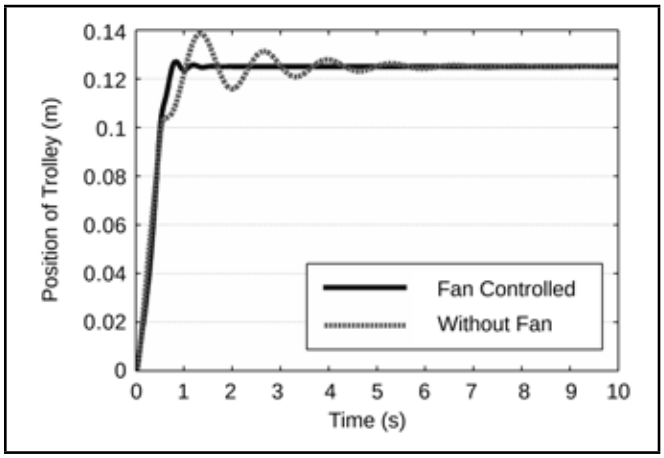

Figure 9. Position response of the trolley (pulse input).

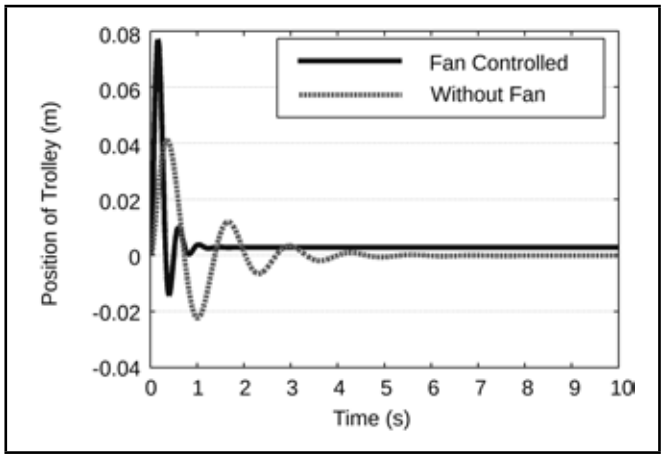

Figure 11. Position response of the trolley (initial $\theta = 0.3$ rad, $m = 1.7$ kg).

system. It was noted that, for payload sway, the thrust force of a fan can eliminate the residual oscillation in a much shorter time (less than two seconds), while without the ducted fan, the system needs more time to eliminate the payload oscillation (about eight seconds). Considering zero sway as the desired response, Integrated Absolute Error (IAE) for a fan-controlled system and a system without a fan were obtained as 6.5463 and 34.3925, respectively. Moreover, because the sway of the payload and the position of the trolley have a direct relationship, the initial payload sway caused the trolley to oscillate. Thus, a reduction of the payload sway is important as it leads to a fast and accurate positioning. It was observed that although a fan-controlled system has a higher initial oscillation compared to the system without a fan, it reaches a steady state faster. In this case, settling times of 0.245 seconds and 0.535 seconds were achieved for the fan-controlled system and the system without a fan, respectively. Moreover, it should be noted that a fan-controlled system needed less than two seconds to reach the steady state, whereas eight seconds is needed for the system without fan.

In the second experiment, the system with an external force and without initial sway was considered. In this case, a pulse input with 5 N force for a duration of 0.5 seconds was used, as shown in Fig. 8. As a result, the crane moves to 0.125 m. As depicted in Fig. 9, the position response of the trolley in fan-controlled system was faster (shorter settling time) with less overshoot. The settling times were obtained as 0.73 seconds and 4.08 seconds with and without a fan, respectively. Figure 10 shows that the proposed control scheme was able to reduce the payload sway significantly. The IAE values were obtained as 1.1088 and 23.7320 for the system with and without a fan, respectively. Moreover, the proposed control system was able to eliminate the sway within two seconds, whereas the system without a fan needed more than eight seconds to eliminate the sway.

Based on the previous case with $m = 1.1$ kg and $l = 0.45$ m, two cases were studied with $m = 1.7$ kg and $l = 0.45$ m (increased payload) and $m = 1.1$ kg and $l = 0.7$ m (increased cable length). Similarly, a condition with an initial sway of 0.3 rad without external input was considered first. Figures 11 and 12 show the trolley position responses with $m = 1.7$ kg and $l = 0.7$ m, respectively, with and without a fan control. In both cases, faster settling times were achieved with the fan-controlled system. However, a slight steady state error was noted with the system. Table 2 summarizes settling times obtained in all cases. It is noted, that an improvement of almost two-folds was achieved using the fan-controlled system as compared to the system without a fan control.

Figures 13 and 14 show payload sway with $m = 1.7$ kg and $l = 0.7$ m, respectively, for both systems. In both cases, the fan-controlled system was able to reduce the payload sway significantly, within less than two seconds. IAE values for all the cases are summarized in Table 2. It was noted that the sway was reduced almost five times with the fan-controlled system. Similar results obtained with different lengths and payloads demonstrate that the proposed fan-controlled system is able to

Table 2. Settling times and IAE values of system responses (initial $\theta = 0.3$ rad).

System		Settling time (s)		IAE	
m (kg)	l (m)	Normal	Fan-Controlled	Normal	Fan-Controlled
1.1	0.45	0.535	0.245	34.3925	6.5463
1.7	0.45	0.59	0.285	22.4666	5.6147
1.1	0.70	0.725	0.305	51.2193	8.4006

Table 3. Settling times and IAE values of system responses (pulse input).

System		Settling time (s)		IAE	
m (kg)	l (m)	Normal	Fan-Controlled	Normal	Fan-Controlled
1.1	0.45	4.08	0.73	23.7320	1.1088
1.7	0.45	2.845	0.775	15.2906	1.1664
1.1	0.70	5.84	0.915	25.1863	1.1071

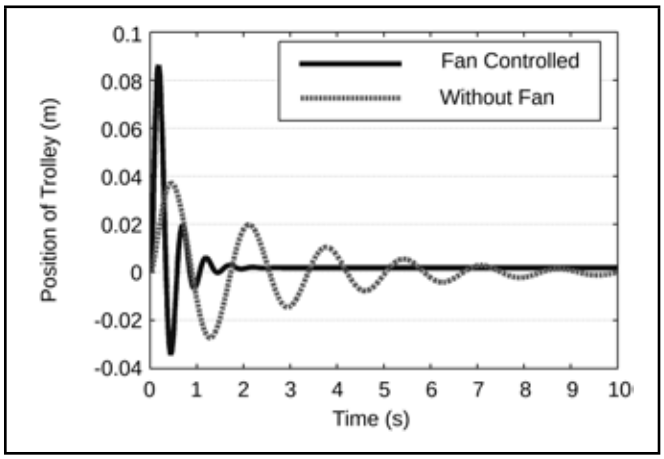

Figure 12. Position response of the trolley (initial $\theta = 0.3$ rad, $l = 0.7$ m).

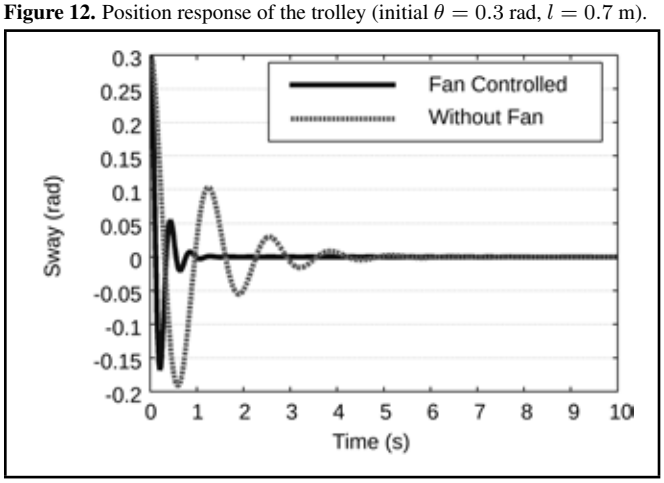

Figure 13. Sway of payload (initial $\theta = 0.3$ rad, $m = 1.7$ kg).

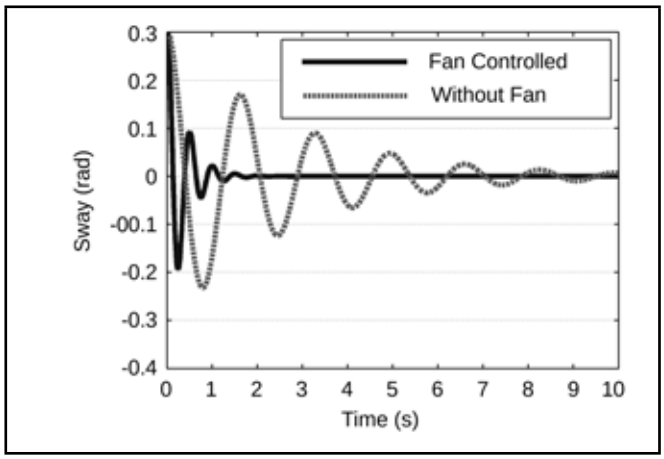

Figure 14. Sway of payload (initial $\theta = 0.3$ rad, $l = 0.7$ m).

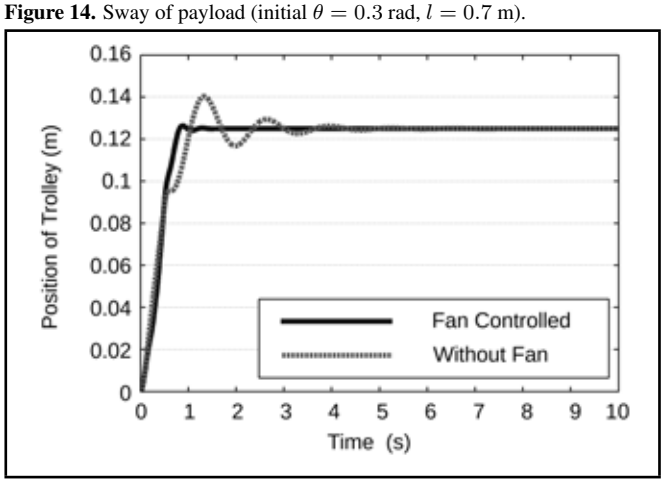

Figure 15. Position response of the trolley (pulse input, $m = 1.7$ kg).

handle changes in the system parameters.

Experiments with a pulse force input, as shown in Fig. 8, were then considered. Figures 15 and 16 show trolley position responses with $m = 1.7$ kg and $l = 0.7$ m, respectively, for both systems. In addition, Figs. 17 and 18 show payload sway for both cases. In both cases, the fan-controlled system showed a similar performance to the first case ($m = 1.1$ kg and $l = 0.45$ m) with faster settling time, lass overshoot and less payload sway. Table 3 summarizes settling times and IAE values for the three cases with and without fans. Again, these results demonstrate that the proposed fan-controlled system is able to handle different cable lengths and payloads where similar system performance is achieved.

The results demonstrate that installing an electrical ducted fan on the crane can improve the performance of the system significantly. One of the most useful advantages of the proposed approach is that it does not need to be modelled after the crane. Therefore, difficulties of modeling for industrial cranes, effects of uncertainties (including changes of load and length during hoisting), and effects of disturbances, such as wind, can be reduced.

5. CONCLUSION

A unique design has been proposed to enable active sway control of a gantry crane by using an electrical ducted fan. The fan is installed in such a way that the thrust force cancels out the oscillation. The proposed design does not need modeling and can overcome parameter uncertainties, such as changes in payload and cable length during hoisting. In addition, the controller is completely independent of the existing gantry crane

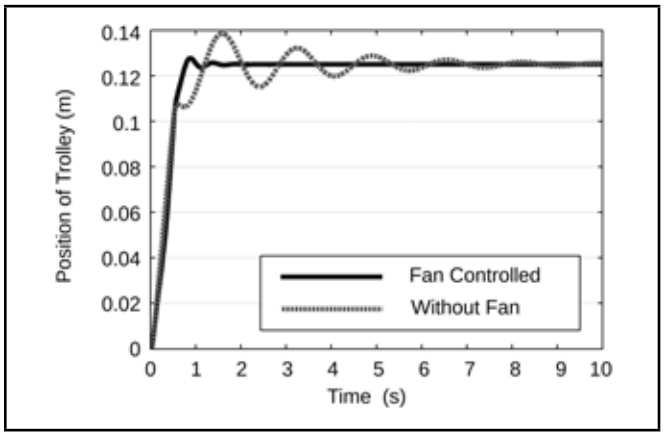

Figure 16. Position response of the trolley (pulse input, $l = 0.7$ m).

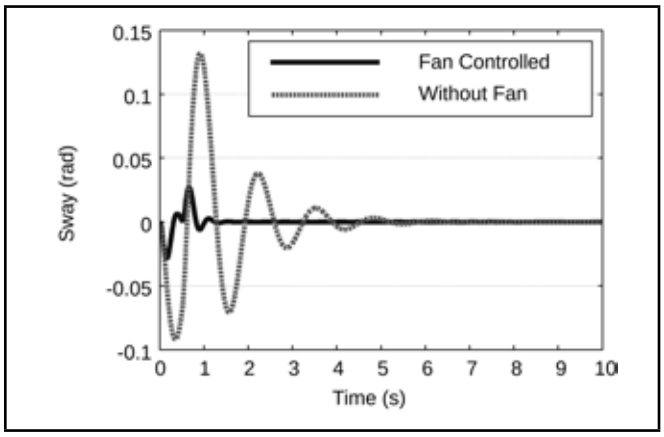

Figure 17. Sway of payload (pulse input, $m = 1.7$ kg).

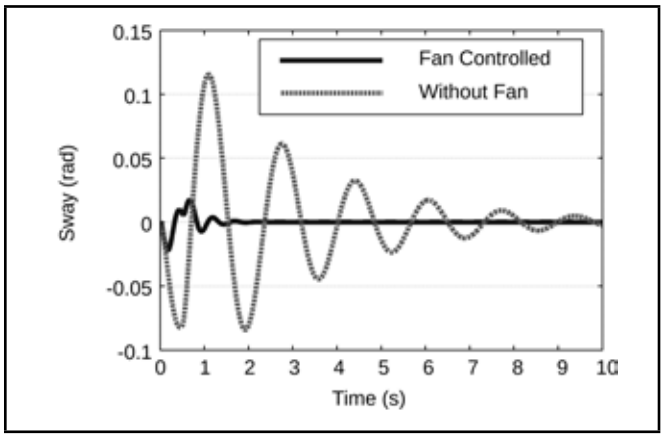

Figure 18. Sway of payload (pulse input, $l = 0.7$ m).

controller. The controller uses a simple proportional controller in a closed loop system. Experiments with several conditions have been simulated in Simulink that have verified acceptable performance of the proposed design in eliminating the existing sway of the gantry crane. The controller has also shown to be able to handle uncertainties in payload and cable length.

REFERENCES

[1] Garitaonandia, I., Albizuri, J., Hernandez-Vazquez, J. M., Fernandes, M. H., Olabarrieta, I. and Barrenetxea, D. Redesign of an active system of vibration control in a centerless grinding machine: Numerical simulation and practical implementation, *Precis. Eng.*, **37**(3), 562–71, (2013).

[2] Majeed, F. A., Karki, H., Karkoub, M. and Magid, Y. L. A. Experimental Verification of Drill String Vibration Suppression Using an Adaptive Self-Tuning Controller, *Int. J. Acoust. Vib.*, **18**(1), 20–6, (2013).

[3] Kwak, M.K. and Yang, D. H. Active vibration control of a ring-stiffened cylindrical shell in contact with unbounded external fluid and subjected to harmonic disturbance by piezoelectric sensor and actuator, *J. Sound. Vib.*, **332**(20), 4775–4797, (2013).

[4] Kapuria, S. and Yasin, M. Y. Active vibration control of smart plates using directional actuation and sensing capability of piezoelectric composites, *Acta Mech.*, **224**(6), 1185–1199, (2013).

[5] Butler, H., Honderd, G. and Van Amerongen, J. Model reference adaptive control of a gantry crane scale model, *IEEE Control Syst. Mag.*, **11**(1), 57–62, (1991).

[6] Yang, J. H. and Yang, K. S. Adaptive coupling control for overhead crane systems, *Mechatronics*, **17**(23), 143–52, (2007).

[7] Mohamed, Z., Martins, J. M., Tokhi, M. O., Sa da Costa, J. and Botto, M. A. Vibration control of a very flexible manipulator system, *Control Eng. Pract.*, **13**(3), 267–277, (2005).

[8] Maghsoudi, M., Mohammed, Z., Pratiwi, A., Ahmad, N. and Husain, A. An experiment for position and sway control of a 3D gantry crane. *4th International Conference on Intelligent and Advanced Systems (ICIAS)*. Kuala Lumpur, Malaysia, 497–502, (2012).

[9] Saeidi, H., Naraghi, M. and Raie, A. A. A neural network self tuner based on input shapers behavior for anti sway system of gantry cranes, *J. Vib. Control*, **19**(13), 1936–1949, (2013).

[10] Grassin, N., Retz, T., Caron, B., Bourles, H., and Irving, E. Robust control of a travelling crane. *Proceedings of the European Control Conference Grenoble*, France, 2196-2201, (1991).

[11] Kim, Y-S., Hong, K-S. and Sul, S-K. Anti-sway control of container cranes: inclinometer, observer, and state feedback, *Int. J. Control Autom.*, **2**(4), 435–449, (2004).

[12] Sorensen, K. L, Singhose, W. and Dickerson, S. A controller enabling precise positioning and sway reduction in bridge and gantry cranes, *Control Eng. Pract.*, **15**(7), 825–837, (2007).

[13] McKerrow, P. J. and Ratner, D. The design of a tethered aerial robot. *International Conference on Robotics and Automation*, IEEE, 355–360, (2007).

[14] Zelei, A, Kovács, L. L. and Stépán, G. Computed torque control of an under-actuated service robot platform modeled by natural coordinates, *Commun Nonlinear Sci.*, **16**(5), 2205-2217, (2011).

[15] Bulk, R. Turbo Fan 4000, Retrived from http://www.rbc-kits.com/shop/index.php?_a=viewProd&productId=260, (Accessed June 1, 2013).

Determination of Modal Constant for Fundamental Frequency of Perforated Plate by Rayleigh's Method using Experimental Values of Natural Frequency

Kiran D. Mali and Pravin M. Singru

Department of Mechanical Engineering, Birla Institute of Technology and Science, Pilani, K.K. Birla Goa Campus, NH-17B, Zuarinagar, Goa, India- 403726

(Received 4 June 2013; accepted 4 March 2014)

In the present work, an expression for the modal constant of the fundamental frequency of the perforated plate was determined experimentally. Rayleigh's formulation was used to calculate the modal constant. The displacement solution was considered to be a linear combination of cosines. In Rayleigh's formulation, fundamental frequency values were taken from experimental analysis. This problem was solved in reverse order by considering known experimental values of the fundamental frequency. Thus, the modal constant expression for fundamental frequency was discovered.

NOMENCLATURE

A	Correction factor
AR	Aspect ratio = $L_y/Lx, = b/a$
L_h	Centre to centre distance between holes along width in mm
L_v	Centre to centre distance between holes along length in mm
$(d + h_r)$	Center to center distance in mm
	Density of material in kg/m^3
D	Diameter of perforation hole in mm
a	Dimension of plate along X axis
b	Dimension of plate along Y axis
L_x	Effective plate width in mm
E	Young's modulus in N/m^2,
L_Y	Effective plate length in mm
h	Effective plate thickness in mm
T, u	Kinetic and strain energy of the plate respectively
h_r	Ligament width in mm
η_l	Ligament efficiency
MRR	Mass remnant ratio
ω_1	Fundamental frequency of perforated plate in Hz
υ	Poisson's ratio
r	Radius of perforation hole in mm
λ	Modal constant
D	Flexural rigidity of the plate = $Eh^3/12(1-\upsilon^2)$

1. INTRODUCTION

Cutouts are found in mechanical, civil, marine and aerospace structures, commonly as access ports for mechanical and electrical systems or simply to reduce weight. Cutouts are also made to provide ventilation and to modify the resonant frequency of the structures. Perforated plates are often utilized as head plates, end covers, or supports for tube bundles, typically including tube sheets and support plates. Perforated plates are widely used in nuclear power equipment, heat exchangers, and pressure vessels. The holes in the plate are arranged in various regular penetration patterns. Industrial applications include both square and triangular array perforation patterns.

Many researchers have carried out studies of perforated plate structures. Monahan et al. studied the finite element analysis of a clamped plate with different cutout sizes along with experiments using holographic interferometry.[1] Paramsivam used a finite difference approach in analyzing the effects of openings on the fundamental frequencies of plates with simply supported and clamped boundary conditions.[2] O'Donnell determined the effective elastic constants for thin perforated plates by equating the strains in an equivalent solid material to the average strains in the perforated material.[3] Hegarty and Ariman investigated free vibrations of rectangular elastic plate either clamped or simply supported with a central circular hole using the least-squares point-matching method.[4] Aksu and Ali obtained dynamic characteristics of rectangular plates with one or two cutouts using a finite difference formulation along with experimental verifications.[5] Ali and Atwal studied the natural frequencies of simply supported rectangular plates and rectangular cutouts using the Raleigh Ritz method.[6] Reddy studied linear and large amplitude flexural vibration of isotropic and composite plates with cutout by using the finite element method.[7] Chang and Chiang studied the vibration of a rectangular plate with an interior cutout by using the finite element method.[8] Lam et al. presented an efficient and accurate numerical method in the study of the vibration of rectangular plates with cutouts and non- homogeneity.[9] They found the deflection function for the originally complex domain by dividing the problem domain into appropriate rectangular segments. Lam and Hung investigatedflexural vibrations of plates with discontinuities in the form of cracks and cutouts using a scheme that combines the flexibility of dividing the problem domain into appropriate segments and the high accuracy resulting from the use of orthogonal polynomial functions, generated using the Gram-Schmidt process.[10] Lee et al. predicted the natural frequencies of rectangular plates with an arbitrarily located rectangular cutout.[11] Mundkur et al. studied the vibration of square plates with square cutouts by using boundary characteristics orthogonal polynomials satisfying the bound-

ary conditions.[12] Burgemeister and Hansen showed that effective material constants could not be used in classical equations to accurately predict the resonance frequencies of simply supported perforated panels.[13] Instead, it is much more accurate to fit the results from ANSYS to a simple cubic function. This function can be used to determine the effective resonance frequency ratio for a large range of panel geometries with an error of less than 3%. Young et al. studied the free vibration of thick rectangular plates with depression, grooves, or cutouts using three-dimensional elasticity and Ritz method.[14] Sivasubramonian et al. investigated the free vibration characteristics of unstiffened and longitudinally stiffened square panels with symmetrical square cutouts by using the finite element method.[15, 16] The optimized Rayleigh-Ritz method was applied by Grossi et al. to generate values of the fundamental frequency coefficient and the one corresponding to the first fully antisymmetric mode for rectangular plates elastically restrained against rotation and with located circular holes.[17] Suhn et al. performed a finite element modal analysis of the perforated plates having square and triangular hole patterns.[18] They carried out a modal analysis of the plates by using existing equivalent elastic properties. They also verified feasibility of the finite element models by conducting a modal test on one typical perforated plate. Parameters, such as natural frequencies and mode shapes, were extracted and compared with the analysis results. Huang and Sakiyama analyzed the free vibration of rectangular plates with variously shaped holes.[19] Sahu and Datta studied the parametric instability behavior of curved panels with cutouts subjected to in-plane static and periodic compressive edge loadings using the finite element analysis.[20] The first order shear deformation theory was used to model the curved panels, considering the effects of transverse shear deformation and rotary inertia. Avalos and Laura performed a series of numerical experiments on vibrating simply supported rectangular plates with two rectangular holes with free edges.[21] Liew et al. presented an analysis of free vibration of plates with internal discontinuities due to central cut-outs.[22] A numerical formulation for the basic L-shaped element, which was divided in to appropriate subdomains that were dependent upon the location of the cut out was used as the basic building element. Wang and Lai adopted the hybrid method, which combined experimental and numerical methods, to investigate the dynamic behavior of perforated plates.[23] The equivalent material properties of the perforated plates were also obtained by the hybrid method. In addition, the curve-fitting technique was utilized to find the relationship of the mass remnant ratio with the parameter ratio. They obtained functions from the curve fitting and used them to accurately predict the equivalent material properties and resonant frequencies of perforated plates of the diagonal array. Sinha et al. suggested a formula for added mass of the vibrating perforated plate-type structures submerged in fluid based on experimental and analytical studies on a number of test specimens.[24] Wu et al. developed a mathematical model of axisymmetric elastic/plastic perforated circular plates for bending and stretching.[25] Bhattacharya and Raj analyzed a quarter symmetric part of a perforated plate containing a 3×3 square array of circular holes by the finite element method (FEM) to obtain the peak stress multipliers under membrane and bending loads for different biaxiality ratios.[26] Britan et al. experimentally and theoretically/numerically studied the flow and wave pattern that resulted from the interaction of an incident shock wave with a few different types of barriers, all having the same porosity but different geometries.[27] Bhattacharya, and Raj also developed second- and fourth- order polynomials describing the yield criterion for perforated plates with square penetration patterns.[28] They did not consider the effect of out-of-plane stresses in the investigation, as these are found to be negligible in the case of thin perforated plates, for which plane stress condition was assumed in the finite element. Pedersen studied the optimization of the hole of a given area, which is placed in the interior of a plate with an arbitrary external boundary.[29] The objectives of the optimization were the eigenfrequencies of the plate with the hole. The optimization was performed in relation to maximizing the first eigenfrequency or maximizing the gap between the first and second eigenfrequency. Lee and Kim studied the validity of the Eshelby-type model for predicting the effective Young's modulus and in-plane Poisson's ratio of two dimensional perforated plates in terms of porosity size and arrangement.[30] Azhari et al. established the nonlinear mathematical theory for initial- and post-local buckling analysis of plates of abruptly varying stiffness based on the principle of virtual work.[31] They programmed the method, and several numerical examples were presented to demonstrate the scope and efficacy of the procedure. Local buckling coefficients of perforated and stepped plates were obtained, and the results were compared with known solutions. They studied the post-buckling behaviour of perforated and stepped plates for different geometries. Rezaeepazhand and Jafari used analytical investigation to study the stress analysis of plates with different central cutouts.[32] Particular emphasis was placed on flat square plates subjected to a uni-axial tension load. They compared results based on analytical solution with the results obtained using finite element methods. Hung and Jo studied free vibration characteristics of a circular perforated plate submerged in fluid with rectangular and square penetration patterns.[33] The natural frequencies were obtained by theoretical calculations and three-dimensional finite element analyses. The effect of holes on the modal characteristics was investigated; they also proposed new equivalent elastic constants for the modal analysis of a perforated plate. Watanabe and Koike investigated fatigue strength and creep-fatigue strength of perforated plates having stress concentration.[34] The specimens were made of type 304 SUS stainless steel, and the temperature was kept to 550°C. The entirety of each cycle of the experiment record was analyzed, and the characteristics of the structures having stress concentration were discussed. They also studied the stress redistribution locus in evaluation plastic behavior in a cyclic fatigue process as well as a stress relaxation in creep process, and the feasibility was discussed in conjunction with the comparison to experimental results. Jeong and Amabili presented a theoretical study on the natural frequencies and the mode shapes of perforated beams in contact with an ideal liquid.[35] The work of Kathagea et al. deals with the design of perforated trapezoidal sheeting.[36] They calculated the effective stiffness values for perforated sheeting with different arrays of holes based on numerical analyses and graphs. Also given was the calculation of a buckling coefficient for a perforated plate under uniform in-plane compression loading and the calculation for an infinitely long perforated plate under shear loading. Paik studied the ultimate strength characteristics of perforated steel plates under edge shear loading[37] and under combined biaxial compression and edge shear loads.[38] Liu et al. studied the effect of the cracks on natural frequencies and the modal strain energy of a perforated plate with ligament fractured cracks by finite element analysis.[39] Cheng and Zhao studied buckling behaviors of uni-axially compressed perforated steel plates strengthened by four types of stiffeners: ringed stiffener, flat stiffener, longitudinal stiffener, and transverse stiffener.[40]

Romero et al. used digital speckle interferometry technique for tuning resonant frequencies of vibrating plates in order to investigate the dynamical behavior of perforated plates.[41] Experimental natural frequencies and modal shapes were compared to those obtained by an analytical approximate solution based on the Rayleigh–Ritz method with the use of orthogonal polynomials as coordinate functions. Mali and Singru introduced the concept of concentrated negative masses for perforation holes and determined the fundamental frequency of a rectangular plate carrying four circular perforations in a rectangular pattern.[42,43] Mali and Singru formulated analytical models by using the greatest integer functions and unit step functions to express non-homogeneity in Young's modulus and the density and determined fundamental frequency of free vibration of a perforated plate.[44–46]

Many studies have been done on perforated plates having rectangular/square and triangular arrays of holes, especially in regards static behavior and stress distribution in the plate. Present literature on the dynamic performance of perforated plates deals with equivalent properties of material. These equivalent material properties can be used to consider perforated plates as full solid plates in vibration analysis. The effect of the hole geometry, hole size, ligament efficiency, and plate support conditions on the dynamic behavior of rectangular plates has not been experimentally studied thus far in combination and or by using FEM. There is no evidence of the formulation of modal constants, functions from curve fitting, or empirical equations to accurately predict the effective resonance frequencies of a wide range of perforation geometries, for rectangular plates with rectangular penetration pattern, or for all edges with clamped support condition.

In the present study, Rayleigh's formulation for perforated plates is carried out by considering a perforated rectangular plate as a full solid plate. Rayleigh's formulation gives an expression for fundamental frequency in terms of equivalent outer dimensions of solid plates and material properties.

Further, Rayleigh's formulation for fundamental frequency is modified with the known value of a fundamental frequency obtained from experimental analysis and by considering actual geometrical parameters of the perforated plate. This modified expression is rearranged to produce an expression for a modal constant.

The proposed approach provides an alternative method to the existing equivalent material properties approach. This modal constant can be directly used to calculate fundamental frequency by using actual material properties instead of equivalent material properties.

In this work, the perforation pattern considered is rectangular with circular perforations. The boundary condition considered is clamped-clamped. Thus, the proposed approach permits the ready determination of reasonably accurate natural frequencies for a plate involving any combination of ligament efficiency and perforation diameter. Presented are the finite element method (FEM) analysis and experimental analysis results for two plates within a given test envelope and outside a test envelope in order to illustrate the applicability and accuracy of the approach.

2. ANALYTICAL FORMULATION

The fundamental frequency expression of a plate is formulated by Rayleigh's principle.[47] This formulation is carried out by considering the perforated plate as a solid plate with the same outer dimensions as that of a perforated plate. Rayleigh's principle is based on the statement, 'If the vibrating system is conservative (no energy is added or lost), then the maximum kinetic energy, T_{max}, must be equal to the maximum potential (strain) energy, u_{max}'. In order to apply this principle, the elastic plate undergoing free vibrations in fundamental mode is considered as a system with one degree of freedom. Kinetic Energy of plate T is given as,

$$T = \frac{1}{2}\iint_R h\rho\, \dot{w}^2(x,y,t)dxdy\,. \tag{1}$$

Assuming that the plate is undergoing harmonic vibrations, then the vibrating middle surface of the plate can be approximated by the equation

$$w\,(x,y,t) = W_1\,(x,y)\cos\omega_1 t; \tag{2}$$

where $W_1(x,y)$ is a continuous function that approximately represents the shape of the plate's deflected middle surface and satisfies at least the kinematic boundary conditions, and ω_1 represents the natural frequency of the plate pertinent to the assumed shape function. Assume $\omega = \omega_1$ would be its fundamental frequency.

The maximum value of Kinetic Energy is obtained at

$$\sin^2\omega_1 t = 1; \tag{3}$$

$$\begin{aligned} T_{\max} &= \frac{{\omega^2}_1}{2}\sin^2\omega_1 t \iint_R h\rho\, \dot{W}^2{}_1(x,\dot{y},)dxdy \\ &= \frac{1}{2}{\omega_1}^2 \iint_R h\rho\, \dot{W}^2{}_1(x,\dot{y},)dxdy\,. \end{aligned} \tag{4}$$

Maximum Strain Energy is given as,

$$\begin{aligned} u_{\max} = \frac{1}{2}\iint_R D[(\nabla^2 W_1)^2 + 2(1-\upsilon)\{(\frac{\partial^2 W_1}{\partial x \partial y})^2 \\ - \frac{\partial^2 W_1}{\partial x}\frac{\partial^2 W_1}{\partial y}\}]dxdy. \end{aligned} \tag{5}$$

For conservative system by Rayleigh's principal,

$$T_{\max} = u_{\max}. \tag{6}$$

From equation (4) and (5), we obtain (7)

$$W_{1,xy} = \frac{\partial^2 W_1}{\partial x \partial y} \quad W_{1,xx} = \frac{\partial^2 W_1}{\partial x^2} \quad W_{1,yy} = \frac{\partial^2 W_1}{\partial y^2}; \tag{8}$$

Equation (7) is called Rayleigh's Quotient and gives the fundamental natural frequency of the plate.

For constant thickness and homogeneous plates, D, ρ, and h are constant. Hence, Rayleigh's Quotient becomes, (9) From Eq. (2) and for the orientation of the plate shown in Fig. 1, assuming the solution of the form,

$$W_1(x,y) = \left[1+\cos\frac{\pi x}{a}\right]\left[1+\cos\frac{\pi y}{b}\right] \quad \text{where} \quad \begin{cases} 0 \leqslant x \leqslant a \\ 0 \leqslant y \leqslant b \end{cases}. \tag{10}$$

$$\omega^2{}_1 = \frac{\iint\limits_R D[(\nabla^2 W_1)^2 + 2(1-\upsilon)\{W^2{}_{1,xy} - W_{1,xx}W_{1,yy}\}]dxdy}{h\rho \iint\limits_R W_1{}^2 dxdy}; \tag{7}$$

$$\omega^2{}_1 = \frac{D\int\limits_0^a\int\limits_0^b [(\nabla^2 W_1)^2 + 2(1-\upsilon)\{W^2{}_{1,xy} - W_{1,xx}W_{1,yy}\}]dxdy}{h\rho \int\limits_0^a\int\limits_0^b W_1{}^2 dxdy}; \tag{9}$$

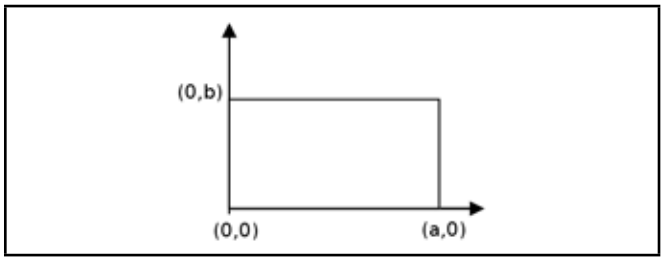

Figure 1. Co-ordinates of the plate.

3. ANALYTICAL SOLUTION

Fundamental frequency ω_1, is obtained by substituting Eq. (10) in Eq. (9) as follows:

$$\omega_1{}^2 = \frac{9D\pi^4}{h\rho a^4 b^4}\left[3\left(a^2b^2\right)b^2 + \left(a^2b^2\right)a^2 + 2a^2b^2 + 2a^2b^2(1-\upsilon^2)\right]. \tag{11}$$

This fundamental frequency equation is further modified by including perforation parameters given by Eq. (18) to get the fundamental frequency Eq. (21) for the perforated plate.

The expression given by Eq. (11) is used to calculate values of the correction factor (A), from known natural frequencies, obtained by experimental analysis.

4. GEOMETRY OF PERFORATED PLATE WITH RECTANGULAR PERFORATION PATTERN

From Fig. 2 consider the triangle ABC with area J as

$$J = \frac{L_h L_v}{2} - \left[\frac{\pi r^2}{4} + \frac{\pi r^2}{4}\right] = \frac{L_h L_v}{2} - \left[\frac{2\pi r^2}{4}\right]; \tag{12}$$

and the number of triangular elements N as

$$N = 2\left[\frac{L_x}{L_h}\ \frac{L_y}{L_v}\right]. \tag{13}$$

The total area of the perforated plate is $K = J \times N$, where

$$K = L_x L_y - \frac{L_x L_y \pi r^2}{L_h L_v}. \tag{14}$$

The mass remnant ratio (MRR) is defined as the ratio of the perforated plate area to the area of the full solid plate of the same outer dimensions. It can be expressed as

$$MRR = \frac{K}{L_x L_y}; \tag{15}$$

where $(L_x L_y)$ is the area of the full solid plate

$$MRR = 1 - \frac{\pi r^2}{L_h L_v}; \tag{16}$$

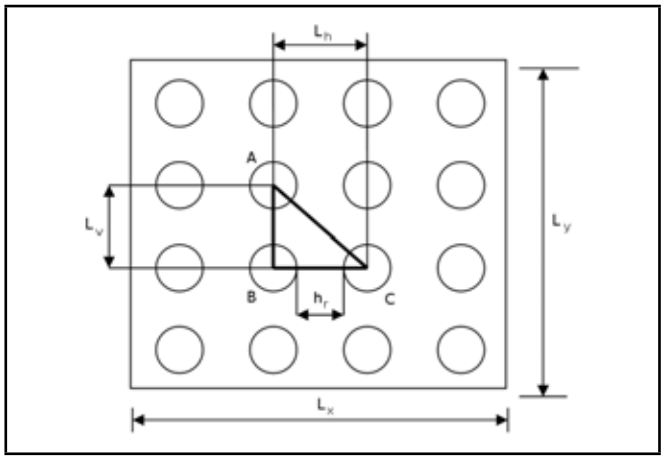

Figure 2. Geometry of the perforated plate.

Table 1. Details of the specimens analyzed experimentally.

η_l	Pitch $(\mathbf{d + h_r})$, (mm)	$\mathbf{h_r}$, (mm)	MRR
For $d = 6$ mm hole			
0.2	7.5	1.5	0.4973
0.6	15	9	0.874
For $d = 9$ mm hole			
0.4	15	6	0.7172
For $d = 12$ mm hole			
0.6	30	18	0.8743

$$MRR = \frac{ab}{ab} - \frac{ab\pi r^2}{abL_h L_v} = 1 - \frac{ab\pi r^2}{abL_h L_v}. \tag{17}$$

Thus, the relation between perforation parameters MRR, L_h, L_v, r and plate dimensions a, b is

$$ab = \frac{(1-MRR)\,L_h L_v ab}{\pi r^2}. \tag{18}$$

The relation between the ligament efficiency, pitch, and ligament width is

$$\eta_l = \frac{(h_r)}{(d+h_r)}; \tag{19}$$

for case the under study

$$L_h = L_v = (d + h_r). \tag{20}$$

5. MATERIALS AND METHOD

Fundamental frequency is obtained experimentally, for four specimens with configurations shown in Table 1. All the specimens are analyzed for the boundary condition clamped on all four edges. The correction factor is determined from Eq. (22) for each specimen from the average values of the fundamental frequencies obtained experimentally.[48]

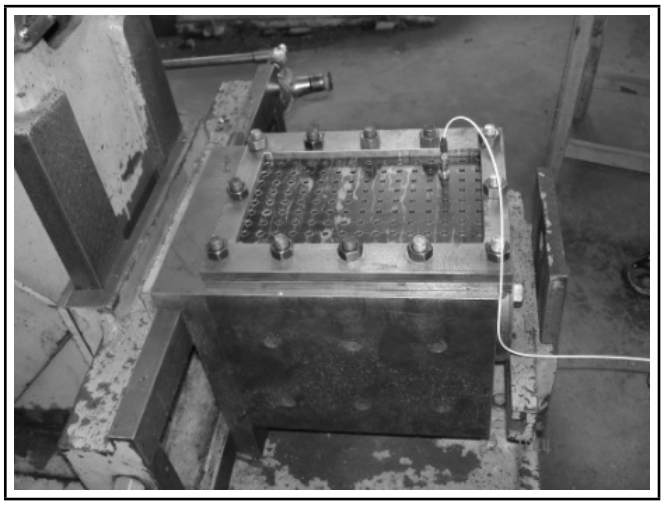

Figure 4. The fixture and specimen.

Figure 5. Experimental set up.

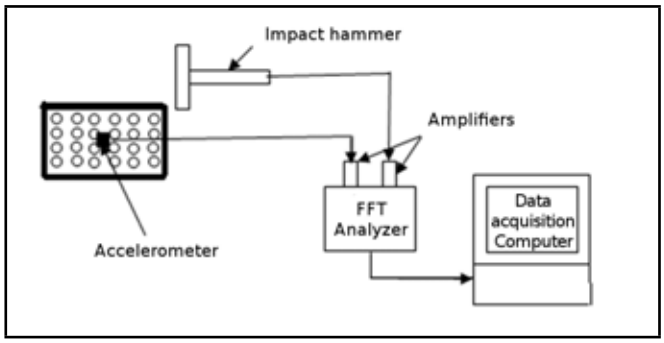

Figure 6. Schematic of experimental set-up.

5.1. Experimental Analysis

This section covers the information about the test specimen, clamping details, and experimental set-up used in the experimental vibration analysis.[48,49] Specimens were prepared for ligament efficiency 0.2, 0.4 and 0.6 and perforation diameters 6 mm, 9 mm, and 12 mm. Each specimen was tested ten times, and the average value of fundamental frequency was obtained. The outer dimensions of all the specimens were 259 mm by 207 mm by 2 mm, but effective dimensions of the perforated area were 216 mm by 138 mm. All specimens were made of mild steel material with an aspect ratio b/a = 1.565. The following is the material properties considered for all specimens: $E = 2.1 \times 10^{11}\mathrm{N/m^2}$, $\upsilon = 0.3$, $\rho = 7850$ kg/m^3

5.2. Test Specimen and Test Fixture

Figure 3 shows the schematic of the specimens used for testing and fixture plate. The margin with holes (outside the effective area) were kept to clamp the specimens between two fixture plates to get the clamed-clamped boundary condition on all four edges of the specimen. The test fixture mainly consisted of two rectangular plates of outer dimensions 259 mm by 207 mm by 9.2 mm. Both these fixture plates had central rectangular cut-outs with dimensions of 216 mm by 138 mm, which were aligned concentrically one over the other. The test specimen with all four outside edges fixed was held centrally between these fixture plates.

Figure 3 shows one of two similar fixture plates with central rectangular cut-outs and holes along the circumference for bolting the plates firmly. These fixture plates, with the test specimen sandwiched, were clamped together by using nut-bolt assembly in the holes provided along the circumference of fixture plates as shown in Figure 4. Thus, the required boundary condition of all four outside edges fixed was achieved.

5.3. Experimental Set up and Procedure

Experimentation was conduced by means of two channel FFT (Model: Virte 300+, Larson and Davis inc, U.S.A.) analyzers, an impact hammer (Model: 086C03, PCB Piezotronics Inc., U.S.A.), and an accelerometer (Model: 352C68, PCB Piezotronics Inc., U.S.A.).[47,48] Figure 5 shows the experimental set up used for testing, and Figure 6 shows schematic of the experimental set up. Care was taken in applying uniform pressure at all bolts with the help of a torque wrench. Four sampling points were chosen for mounting the accelerometer from the driving point survey such that the node would not occur at these points. A fixed response method was used for taking readings. The transfer function of each sampling point was calculated by the spectrum analyzer and was recorded at sixteen impacts to get the final spectrum for each specimen plate. Such experiments were repeated ten times. The final results of the natural frequencies for each specimen plate were mean values of the ten readings. The final values of natural frequency were tabulated in the last column of the Table 2. The dynamic mass of the accelerometer was much less than that of the plate, so the influence of the mass of the accelerometer on the dynamic behavior of the specimen could be neglected.

6. RESULTS AND DISCUSSION

The average value of the fundamental frequency of each specimen from Table 2 was used to calculate the value of the correction factor for respective specimens.

6.1. Determination of the Modal Constant

The expression for the natural frequency of the solid plate given by Eq. (11) could be modified by considering actual geometrical parameters of the perforated plate. Geometrical parameters of the perforated plate were related to the full solid plate dimensions by the relation given in Eq. (18). The expression in Eq. (21) can not be used directly to calculate the fundamental frequency of the perforated plate unless the correction factor is considered.

After simplification and after considering the correction fac-

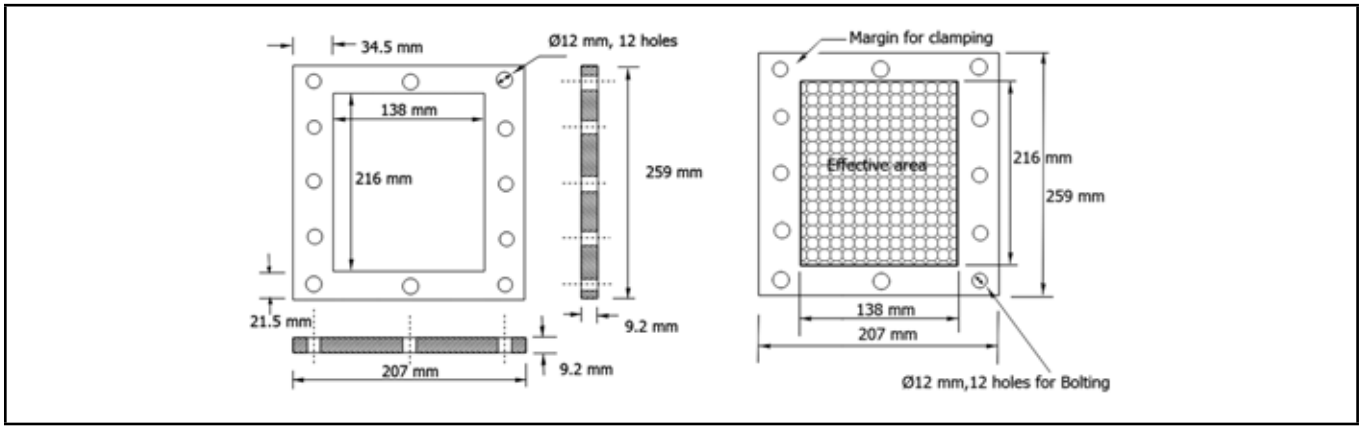

Figure 3. Schematic of the fixture plate and specimens used for experimentation.

Table 2. Experimentally obtained values of fundamental frequency.

η_1	Pitch d, (mm)	Fundamental frequency,(No. of Runs) Hz										
		1	2	3	4	5	6	7	8	9	10	Avg.
0.2	6	602	596	596	599	599	580	583	583	586	583	590.7
0.6	6	615	615	618	615	618	615	615	621	615	615	616.2
0.4	9	571	571	571	571	571	571	571	571	571	571	571
0.6	12	586	586	586	586	586	586	590	590	590	590	587.6

$$\omega_1{}^2 = \frac{9D\pi^4}{h\rho\left[\frac{(1-MRR)L_hL_vab}{\pi r^2}\right]^4}\left[\begin{array}{l} 3\left[\frac{(1-MRR)\,L_hL_vab}{\pi r^2}\right]^2 b^2 + \left[\frac{(1-MRR)\,L_hL_vab}{\pi r^2}\right]^2 a^2 + \\ 2\left[\frac{(1-MRR)\,L_hL_vab}{\pi r^2}\right]^2 + 2\left[\frac{(1-MRR)\,L_hL_vab}{\pi r^2}\right]^2 (1-\upsilon^2) \end{array}\right]; \tag{21}$$

tor, Eq. (21) becomes

$$\omega_1{}^2 = \frac{9D\pi^6 r^4}{h\rho[(1-MRR)\,L_hL_vab]^2}\cdot \cdot\left[3b^2+a^2+2+2(1-\upsilon^2)\right](A); \tag{22}$$

where A is introduced as the correction factor. Values of the correction factor are calculated from Eq. (22) by using fundamental frequencies determined experimentally, tabulated in the last column of Table 2. Correction factor values are tabulated in Table 3 for different specimens. Equation 22 can be used for calculating the fundamental frequency of the perforated plate by substituting the average value of correction factor 'A', from Table 3. A simple approximate formula for the fundamental natural frequency of the flexural vibration of the rectangular isotropic perforated plate is given as,[50]

$$\omega_1 \approx \sqrt{\frac{\lambda D}{h\rho}}; \tag{23}$$

where λ is the modal constant.

Thus, the modal constant λ for fundamental frequency is obtained from Eqs. (22) & (23).

$$\lambda = \left[\frac{9\pi^6 r^4}{[(1-MRR)\,L_hL_vab]^2}\cdot \cdot\left[3b^2+a^2+2+2(1-\upsilon^2)\right](A)\right]; \tag{24}$$

$$\lambda = \left[\frac{9\pi^6 r^4}{[(1-MRR)\,L_hL_vab]^2}\cdot \cdot\left[3b^2+a^2+2+2(1-\upsilon^2)\right](0.009129)\right]. \tag{25}$$

The expression given by Eq. (24) can be used to calculate the modal constant λ for the fundamental natural frequency of the perforated plates with rectangular perforation patterns of circular perforations having different configurations.

6.2. Application and Accuracy of the Approach

The proposed approach is validated by additional experimental analysis and by running FEM simulations with ANSYS. Configurations of the specimens are given in Tables 4 & Table 5. The criteria followed to select the plate dimensions in the analysis were

1. Validating the results of the proposed approach within the test envelope, or the effective outer dimensions (a, b) that were the same as the specimens given in Section 5.

2. Validating the results of the proposed approach outside the test envelope, or the effective outer dimensions (a, b) that were different from the specimens given in Section 5.

FEM analysis was carried out by using the shell63 element. It is assumed that the structure is formed from isotropic homogeneous elastic material, or mild steel. Effective outside dimensions, thickness, and material properties of the first specimen analyzed are the same as that used in the test envelope and within the fixture limit, but configuration is different from the test envelope. However, the second specimen thickness and material properties were the same as that used in the test envelope, but the effective outside dimensions (a, b) and configurations were different from the test envelope. Due to the size limitations of the test fixture experimental validation was not carried out for second case as given in Table 5. It was found that the results obtained from the proposed method are in close

Table 3. Values of the correction factor for different specimens

Sr. no.	η_l	d, mm	MRR	L_h, mm	L_v, mm	ω_{1avg}	Value of A
1	0.2	6	0.4973	7.5	7.5	590.7	0.009099
2	0.6	6	0.8743	15	15	616.2	0.009906
3	0.4	9	0.7172	15	15	571	0.008504
4	0.6	12	0.8743	30	30	587.6	0.009007
					Average Value of 'A' =		0.009129

Table 4. Validation of the modal constant within the test envelope.

a, mm	b, mm	d, mm	η_l	$L_h = L_v$, mm	MRR	ω_1 With modal Constant, Hz	ω_1, ANSYS, Hz	ω_1 With Experimental Analysis, Hz
138	216	9	0.4	15	0.7172	591.60	612.62	571

Table 5. Validation of the modal constant outside the test envelope.

a, mm	b, mm	d, mm	η_l	$L_h = L_v$, mm	MRR	ω_1 With modal Constant, Hz	ω_1, ANSYS, Hz
550	860	50	0.6	125	0.87433	47.07	42

agreement with the experimental and FEM results within test envelope and are in close agreement with the FEM results outside the test envelope.

7. CONCLUSION

In the present work, the expression for the modal constant for fundamental frequency of the perforated plate was determined. To establish this modal constant, experimental vibration data was used. A simple approximate formula for the fundamental natural frequency of flexural vibration of a rectangular isotropic perforated plate was developed. Rayleigh's method was used in combination with experimental values of the natural frequency to establish the expression for the modal constant. The fundamental frequency calculated by using this modal constant is in good agreement with ANSYS result. Thus, this approach provides an alternative method to the equivalent elastic properties method of the perforated plate for finding natural frequency.

REFERENCES

[1] Monahan, J., Nemergut, P. J., and Maddux, G. E. Natural frequencies and mode shapes of plates with interior cutouts, *The Shock and Vibration Bulletin*, **41**(7), 37–49, (1970).

[2] Paramsivam, P. Free vibration of square plates with square openings, *Journal of Sound and Vibration*, **30**(2), 173–178, (1973).

[3] O'Donnell, W. J. Effective elastic constants for the bending of thin perforated plates with triangular and square penetration patterns, *Journal of Engineering for Industry*, **95**(1), 121–128, (1973).

[4] Hegarty, R. F. and Ariman, T. Elasto-dynamic analysis of rectangular plates with circular holes, *International Journal of Solids Structures*, **11**(7–8), 895–906, (1975).

[5] Aksu, G. and Ali, R. Determination of dynamic characteristics of rectangular plates with cutouts using a finite difference formulation, *Journal of Sound and Vibration*, **44**(1), 147–158, (1976).

[6] Ali, R. and Atwal, S. J. Prediction of natural frequencies of vibration of rectangular plates with rectangular cutouts, *Computers and Structures*, **12**(6), 819–823, (1980).

[7] Reddy, J. N. Large amplitude flexural vibration of layered composite plates with cutout, *Journal of Sound and Vibration*, **83**(1), 1–10, (1982).

[8] Chang, C. N. and Chiang, F. K. Vibration analysis of a thick plate with an interior cutout by a finite element method, *Journal of Sound and Vibration*, **125**(3), 477–486, (1988).

[9] Lam, K. Y., Hung, K. C., and Chow, S. T. Vibration analysis of plates with cutouts by the modified Rayleigh-Ritz method, *Applied Acoustics*, **28**(1), 49–60, (1989).

[10] Lam, K. Y. and Hung, K. C. Orthogonal polynomials and subsectioning method for vibration of plates, *Computers and Structures*, **34**(6), 827–834, (1990).

[11] Lee, H. P., Lim, S. P., and Chow, S. T. Prediction of natural frequencies of rectangular plates with rectangular cutouts, *Computers and Structures*, **36**, 861–869, (1990).

[12] Mundkar, G., Bhat, R. B., and Neriya, S. Vibration of plates with cutouts using boundary characteristics orthogonal polynomial functions in the Raleigh-Ritz method, *Journal of Sound and Vibration*, **176**(1), 136–144, (1994).

[13] Burgemeister, K. A. and Hansen, C. H. Calculating resonance frequencies of perforated panels, *Journal of sound and vibration*, **196**(4), 387–399, (1994).

[14] Young, P. G., Yuan, J., and Dickinson, S. M. Three dimensional analysis of the free vibration of thick rectangular plates with depressions, grooves or cutouts, *American Society of Mechanical Engineers Journal of Vibration and Acoustics*, **118**(2), 184–189, (1996).

[15] Sivasubramonian, B., Kulkarni, A. M., and Rao, G. V. Free vibration of curved panels with cutouts, *Journal of Sound and Vibration*, **200**(2), 227–234, (1997).

[16] Sivasubramonian. B., Rao, G. V., and Krishnan, A. Free vibration of longitudinally stiffened curved panels with cutouts, *Journal of Sound and Vibration*, **226**(1), 41–55, (1999).

[17] Grossi, R. O., Del V. Arenas, B., and Laura, P. A. A. Free vibration of rectangular plates with circular openings, *Ocean Engineering*, **24**(1), 19–24, (1997).

[18] Suhn, C., Kyeonghoon, J., Taewan, K., Soo, K. K., Bae, P. K. Free vibration analysis of perforated plates using equivalent elastic properties, *Journal of the Korean Nuclear Society*, **30**(4), 416–423, (1998).

[19] Huang, M., and Sakiyama, T. Free vibration analysis of rectangular plates with variously shaped holes, *Journal of Sound and Vibration*, **226**(4), 769–786, (1999).

[20] Sahu, S. K. and Datta, P. K. Dynamic stability of curved panels with cutouts, *Journal of Sound and Vibration*, **251**(4), 683–696, (2003).

[21] Avalos, D. R. and Laura, P. A. A. Transverse vibrations of simply supported rectangular plates with two rectangular cut outs, *Journal of Sound and Vibration*, **267**(4), 967–977, (2003).

[22] Liew, K. M., Kitipornchai, S., Leung, A. Y. T., and Lim, C.W. Analysis of the free vibration of rectangular plates with central cut-outs using the discrete Ritz method, *International Journal of Mechanical Sciences*, **45**(5), 941–959, (2003).

[23] Wang, W. C., and Lai, K. H. Hybrid determination of equivalent characteristics of perforated plates, *Experimental Mechanics*, **43**(2), 163–172, (2003).

[24] Sinha, J. K., Singh, S., and Rao, A. R. Added mass and damping of submerged perforated plates, *Journal of Sound and Vibration*, **260**(3), 549–564, (2003).

[25] Wu, D., Peddieson, J., Buchanan, G. R., and Rochelle, S. G. Large axisymmetric deformations of elastic/plastic perforated circular plates, *Journal of Pressure Vessel Technology*, **125**(4), 357–364, (2003).

[26] Bhattacharya, A., and Raj, V. V. Peak stress multipliers for thin perforated plates with square arrays of circular holes, *International Journal of Pressure Vessels and Piping*, **80**(6), 379–388, (2003).

[27] Britan, A., Karpov, A. V., Vasilev, E. I., Igra, O., Ben-Dor, G., and Shapiro., E. experimental and numerical study of shock wave interaction with perforate plates, *Journal of Fluids Engineering*, **126**, 399–409, (2004).

[28] Bhattacharya, A., and Raj, V. V. yield criterion for thin perforated plates with square penetration pattern, *Journal of Pressure Vessel Technology*, **126**, 169–175, (2004).

[29] Pedersen, N. L. Optimization of holes in plates for control of eigenfrequencies, *Journal of Structural and Multidisciplinary Optimization*, **28**, 1–10, (2004).

[30] Lee, J.-K. and Kim, J.-G. An analytical study on prediction of effective elastic constants of perforated plate, *Journal of Mechanical Science and Technology*, **19**(12), 2224–2230, (2005).

[31] Azhari, M., Shahidi, A. R., and Saadatpour, M. M. Local and post local buckling of stepped and perforated thin plates, *Applied Mathematical Modelling*, **29**, 633–652, (2005).

[32] Rezaeepazhand, J. and Jafari, M. Stress analysis of perforated composite plates, *Composite Structures*, **71**, 463–468, (2005).

[33] Hung, M. J., and Jo, J. C. Equivalent material properties of perforated plate with triangular or square penetration pattern for dynamic analysis, *Nuclear Engineering and Technology*, **38**, 689–696, (2006).

[34] Watanabe, O., and Koike, T. Creep-fatigue life evaluation method for perforated plates at elevated temperature, *Journal of Pressure Vessel Technology*, **128**(1), 17–24, (2006).

[35] Jeong, K.-H., and Amabili, M. Bending vibration of perforated beams in contact with a liquid, *Journal of Sound and Vibration*, **298**(1–2), 404–419, (2006).

[36] Kathagea, K., Misiekb, T. H., and Saal, H. Stiffness and critical buckling load of perforated sheeting, *Thin-Walled Structures*, **44**(12), 1223–1230, (2006).

[37] Paik, J. K. Ultimate strength of perforated steel plates under edge shear loading, *Thin-Walled Structures*, **45**(3), 301–306, (2007).

[38] Paik, J. K. Ultimate strength of perforated steel plates under combined biaxial compression and edge shear loads, *Thin-Walled Structures*, **46**(2), 207–213, (2008).

[39] Liu, T., Wang, K., Dong, Q.-W., and Liu, M.-S. Hydro elastic natural vibrations of perforated plates with cracks, *Procedia Engineering*, **1**(1), 129–133, (2009).

[40] Cheng, B. and Zhao, J. Strengthening of perforated plates under uniaxial compression: Buckling analysis, *Thin-Walled Structures*, **48**(12), 905–914, (2010).

[41] Romero, G. G., Alans, E. E., Martnez, C. C., Nallim, L. G., Toledo, M. W., lvarez, L. Vibration analysis of perforated plates using time-average digital speckle pattern interferometry, *Experimental Mechanics*, **50**(7), 1013–1021, (2010).

[42] Mali, K. D. and Singru, P. M. Determination of the fundamental frequency of perforated plate with rectangular perforation pattern of circular holes by negative mass approach for the perforation, *International Journal of Advanced Materials Manufacturing and Characterization*, **1**(1), 105–109, (2012).

[43] Mali, K. D. and Singru, P. M. Determination of the fundamental frequency of perforated rectangular plates: Concentrated negative mass approach for the perforation, *Advances in Acoustics and Vibrations*, **2013**, 1–6, (2013).

[44] Mali, K. D. and Singru, P. M. An analytical model to determine fundamental frequency of free vibration of perforated plate by using greatest integer functions to express non homogeneity, *Advanced Materials Research*, **622**, 600–604, (2012).

[45] Mali, K. D. and Singru, P. M. An analytical model to determine fundamental frequency of free vibration of perforated plate by using unit step functions to express non homogeneity, *Journal of Vibroengineering*, **14**(3), 1292–1298, (2012).

[46] Mali, K. D. and Singru, P. M. An analytical model to determine fundamental frequency of rectangular plate having rectangular array of circular perforations, *Journal of Vibroengineering*, **15**(2), 588–596, (2013).

[47] Chakraverty, S. *Vibration of Plates*, Boca Raton, CRC Press Taylor & Francis Group, (2009), 83–135.

[48] Piersol, A. G., and Paez, T. L. *Harris' Shock and Vibration Handbook*, New York, McGraw-Hill (2002), 6th ed., 440–461.

[49] Larson and Davis, Inc., ViRTe3000+ Real Time Analyzer Reference Manual, New York, Larson and Davis Publication Division., (2008).

[50] Leissa, Arthur W., and Mohamad S. Qatu. *Vibration of Continuous Systems*. New York, McGraw Hill,(2011), 1st ed., 229-231.

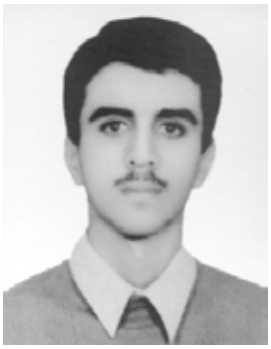

Reza Ramezanpour received his BS and MS in mechanical engineering from Guilan University and Isfahan University of Technology in 2006 and 2008, respectively. His research interests include nonlinear vibrations and experimental and analytical modal analysis.

Mostafa Ghayour received his MS in mechanical engineering from Tehran University in 1978. He received his PhD from Isfahan University of Technology in 1998. Currently, he is an associated professor in the Mechanical Engineering Deptartment, Isfahan University of Technology, Isfahan, Iran. His research interests include robotics, control systems, and mechanical vibrations.

Saeed Ziaei-Rad received both his BS and MS in mechanical engineering from Isfahan University of Technology, Isfahan, Iran, in 1988 and 1990, respectively. He also earned his PhD from the Department of Mechanical Engineering, Imperial College of Science and Technology in 1997. He is an academic member of the Mechanical Engineering Department of Isfahan University of Technology and has many publications in international journals and conferences.

Weipeng Li is currently an Associate Professor at Shanghai Jiaotong University and is actively engaged in the research areas of computational aeroacoustics, high-speed turbulent flows and active flow control techniques. In 2008, he graduated from Harbin Institute of Technology as an engineering masters student. In 2011, he completed his PhD degree from the Department of Aeronautics and Astronautics, University of Tokyo.

Taku Nonomura is an assistant professor at the Japan Aerospace Exploration Agency Institute of Space and Astronautical Science (JAXA/ISAS). He is currently involved in aerodynamics/aeroacoustics research and specifically focuses on researching the acoustic waves from rocket plumes.

About the Authors

Fujii Kozo is a professor at the Japan Aerospace Exploration Agency Institute of Space and Astronautical Science (JAXA/ISAS).

Umberto Iemma has been an associate professor of aeronautical structures and design at the Roma Tre University since 1996. His research interests are primarily related to the theoretical and numerical modeling in acoustics, aeroacoustics, aerodynamics, structural dynamics, and aeroelasticity, as well as the multidisciplinary design optimization of innovative, environment-friendly aircraft. He has also been involved in the development of innovative approaches for high performance computing in engineering applications, as well as higher-order boundary element and finite element formulations for aerodynamics, aeroacoustics, and structural dynamics. Since 2008, he has been a committer of the open-source project AcouSTO (Acoustic Simulation TOol, http://acousto.sourceforge.net). Since 2009, he has been deeply involved in the theoretical and numerical modeling of acoustic meta-materials using integral-equation-based methods. He is also the author of more than 100 scientific papers published in refereed international journals or presented at international conferences.

Vincenzo Marchese, PhD, is mainly an independent IT consultant and has been working since 1997 with the University of Rome III. His primary research fields are higher order boundary element methods, acoustics and aeroacoustics, the design of meta-materials for acoustic applications, compressible and incompressible aerodynamics for subcritical and supercritical flows, and high performance computing. Since 2008, he has been a committer of the open-source project AcouSTO (http://acousto.sourceforge.net).

Navin Kumar is an assistant professor in the School of Mechanical Materials and Energy Engineering at the Indian Institute of Technology (IIT), Ropar, India. Prior to joining IIT Ropar, he worked as a research scientist at Stevens Institute of Technology, New Jersey, USA. He completed his masters degree in mechanical engineering at the Indian Institute of Technology, Kharagpur, India and his PhD (mechanical engineering) from the Indian Institute of Technology, Delhi, India. His research interests are related to smart structures and materials, fault diagnosis, and condition monitoring.

Sukhjeet Singh is a research scholar in the School of Mechanical Materials and Energy Engineering at the Indian Institute of Technology, Ropar, India. He received his bachelor's (mechanical engineering) and masters degrees (mechanical engineering with specialization in machine design) from the Punjab Technical University, Jalandhar, Punjab, India. His research interests include mathematical as well as experimental aspects of vibration analysis, rotor dynamics, signal processing, and machine learning techniques.

Ji-Hu Bao received his MS degree from the Institute of Automotive Engineering at Shanghai Jiaotong University, China. He is currently a PhD candidate in the School of Mechanical Engineering at Shanghai Jiaotong University. His main research interests include dynamics modeling vibration analysis, control of elevator systems, and strength analysis of machinery.

Peng Zhang received his PhD degrees from the School of Mechanical Engineering, Shanghai Jiaotong University, China. He is currently an assistant professor in the School of Mechanical Engineering, Shanghai Jiaotong University, China. His main research interests include system dynamics analysis, the computer modeling and simulation of complex systems, and the energy saving technology of the elevator.

Chang-Ming Zhu is a professor in the School of Mechanical Engineering, Shanghai Jiaotong University, China. His main research interests include the logistics equipment system dynamics and measurement, control, and intelligence of electromechanical systems

Ming Zhu received his bachelors degree from the School of Mechanical Engineering at East China University of Science and Technology. He is currently a PhD candidate in the School of Mechanical Engineering at Shanghai Jiaotong University. His main research interests include dynamics modeling, control of vibration isolators, and the installation of offshore wind turbines.

About the Authors

Zaharuddin Mohamed is an associate professor in the Department of Control and Mechatronics Engineering at Universiti Teknologi Malaysia. He received BS in electrical and electronics engineering from the National University of Malaysia in 1993 and his MS and PhD in control systems engineering from the University of Sheffield, UK in 1995 and 2003, respectively. He was a recipient of the Islamic Development Bank Merit Scholarship for his PhD study. His research interests include command shaping control of dynamic systems, control of flexible structures, and mechatronic systems.

Mohammad Javad Maghsoudi received his BS in telecommunication engineering from the University of Tehran, Iran, in 1998 and his MS in mechatronic engineering from the Universiti Teknologi Malaysia (UTM) in 2010. He worked in industry before pursuing his graduate degree where he developed and installed control systems on industrial machines, such as hot rolling, scalping, and cut-to-length machines for the copper industry. He received an academic excellence award for his MS degree. Currently, he is pursuing a PhD at UTM, and he is a recipient of the Malaysian International Scholarship award. His research interests include control of flexible structures and utilizing meta-heuristic methods in multi-objective control systems.

Kiran D. Mali is currently working as lecturer in the Deptartment of Mechanical Engineering BITS-Pilani, K. K. Birla Goa Campus. He completed his BE in mechanical engineering in 2002 and his masters degree in design engineering, from Shivaji University, Kolhapur, in 2006. He joined BITS-Pilani in May of 2007. He has more than eight years teaching experience and teaches courses in mechanics of solids, kinematics and dynamics of machines, and vibrations. His research areas include vibration analysis of structural components, experimentation, and analysis. He has published seven research papers in international journals and eight papers in national & international conferences. Currently, he is also a reviewerof two international journals.

Pravin M. Singru is an associate professor of mechanical engineering at BITS Pilani, K. K. Birla Goa Campus. He obtained his masters degree in information technology from IIT, Kharagpur, and his PhD from Visvesvaraya National Institute of Technology, Nagpur. His doctoral thesis was on "Dynamic and Vibration Response of Pulleys of a Belt Drive." Prof. Singru has more than 22 years of teaching and research experience and teaches courses in mechanics of solids, kinematics and dynamics of machines, vibrations, and MEMS. Four research scholars have received the PhD under him, and two have submitted their thesis under his guidance. He has published 19 research papers in international journals and 36 papers in national & international conferences. He is reviewerof five international journals.